AN ABSTRACT OF THE DISSERTATION OF

Gregory J. Giesbers for the degree of Doctor of Philosophy in Physics presented on June 1, 2021.

Title: (Opto)electronic Properties of Xylindein and Organic (Opto)electronic Devices.

Abstract approved:

_____

Oksana Ostroverkhova

Organic semiconductors are of interest for (opto)electronic applications due to their low cost, solution processability, and tunable properties. Natural product-derived organic pigments have attracted attention due to their extraordinary environmental stability and unexpectedly good optoelectronic performance, in spite of only partially conjugated molecular structures. Fungi-derived pigments are a naturally sourced, sustainable class of materials that are largely unexplored as organic semiconductor materials. My research has focused largely on the optical and electronic properties of a fungi-derived pigment xylindein, which is secreted by the wood-staining fungi *Chlorociboria (C.) aeruginosa*. Device applications for xylindein have been explored to utilize its unique properties. A second project in my research focuses on polaritons in acenes and thiophenes, with a goal of harnessing polaritons to enhance physical and chemical properties relevant for electronic applications such as conductivity and stability. In particular, I have succeeded in incorporating an optical cavity into an anthradithiophene field effect transistor structure and explored the effects of the polaritons on device performance.

Optical and electronic properties of xylindein were explored initially, and a strategy to improve the innately poor processability was developed. Optical absorption spectra in solutions of various concentrations and in film were compared and are consistent

with aggregate formation in concentrated solutions and films. An amorphous polymer PMMA was introduced to xylindein to form xylindein:PMMA blends in order to improve film morphology. Current-voltage characteristics and hole mobilities extracted from space-charge limited currents were found to be comparable between pristine xylindein and xylindein:PMMA films. Side by side comparison of the photoresponse of pristine xylindein and xylindein:PMMA films at 633 nm revealed an increase in the photosensitivity in xylindein:PMMA films due to the improved morphology favoring enhanced charge generation.

After seeing large variations in data from different batches of xylindein, a simple purification step ("ethanol wash") was developed, and the impact of contaminants was investigated. The optical and electronic properties of solutions and films were studied with and without this processing procedure. The "post-wash" xylindein solutions exhibited considerably lower absorption in the ultraviolet spectral range and dramatically reduced photoluminescence below 600 nm, due to removal of contaminants most likely to be fungal secondary metabolites. The "post-wash" xylindein-based films were characterized by two orders of magnitude higher charge carrier mobilities as compared to "pre-wash" samples. This underlines the importance of minimizing contaminants that disrupt the conductive xylindein network in xylindein-based electronic devices.

With a simple and effective purification protocol in place, the optical and electronic properties of xylindein were studied in more depth, along with its blends with poly(methyl methacrylate) (PMMA) and crystalline nanocellulose (CNC). Optical absorption spectra of xylindein revealed the presence of two tautomers whose structures and properties were established using density functional theory. Pronounced pigment aggregation in polar solvents and in films, driven by intermolecular hydrogen bonding, was also observed. The pigment exhibited high photostability, electron mobility up to 0.4 $cm^2/(Vs)$ in amorphous films, and thermally activated charge transport and photoresponse with activation energies of ~0.3 eV and 0.2 eV, respectively. The dark and photocurrents in xylindein:PMMA

blends were comparable to those in pristine xylindein film, whereas blends with CNC exhibited lower currents due to inhomogeneous distribution of xylindein in the CNC.

One of reasons for studying xylindein is its remarkable stability, which is often an issue for organic semiconductors. Unlike most conventional organic semiconductors, xylindein has hydroxyl (OH) groups in its molecular structure. We sought to determine what role those OH groups and the hydrogen bonding they enable play in the stability and (opto)electronic properties of xylindein. We determined that the presence of the OH groups is critical for enabling its enhanced stability and relatively high electron mobility. In particular, we synthesized a methylated derivative of xylindein, dimethylxylindein, where the OH groups are replaced with OCH_3 groups, and compared photophysics and (opto)electronic properties of dimethylxylindein and xylindein. We revealed the presence of a long-lived excited state in dimethylxylindein, in contrast to xylindein, which has an efficient fast non-radiative pathway to the ground state. This results in significantly reduced photostability of dimethylxylindein as compared to xylindein. The effective electron mobility, obtained from space-charge-limited currents, in amorphous xylindein films was found to be four orders of magnitude higher than that in amorphous and crystalline dimethylxylindein films. In contrast, the photosensitivity of dimethylxylindein is about two orders of magnitude higher than that of xylindein. The mechanism of charge transport in all films was thermally-activated hopping, with the xylindein films characterized by considerably shallower charge traps than dimethylxylindein films, attributed to hydrogen bonding via hydroxyl groups promoting efficient conductive network in xylindein.

Potential (opto)electronic device applications were explored for xylindein with the hopes of using it as a stable, environmentally friendly alternative to current device materials. Thin films of various blends of xylindein with other organic semiconductor materials were studied for evidence of charge transfer for potential use in donor-acceptor (D-A) bulk heterojunction (BHJ) solar cells. Fullerenes are the most common high performance acceptor material in organic BHJ solar cells, though they

are costly and have degradation issues. Thus, there is much interest in finding stable non-fullerene acceptor materials. The high photostability and decent electron mobility of xylindein made it an attractive candidate in this application. Enhanced photostability was observed in thin films of PTB7-Th (a high-performance donor material) blended with xylindein on Au electrodes with 100V applied. BHJ solar cells were fabricated and cells with xylindein blends were observed to be non-functional. Ternary blend solar cells were fabricated with 0-5% xylindein, and xylindein was observed to have a detrimental effect on performance, even in small quantities. With these observations, we hypothesized that the inhibition of charge separation and extraction is likely caused by the short exciton lifetime of xylindein, which promotes exciton recombination.

Organic filed effect transistors (OFETs) were also explored as a potential application. Stable n-type organic semiconductors are rare, and their performance tends to lag behind their p-type counterparts. Complimentary circuits require both n- and p-type transistors to operate, so there is a need for stable, high-mobility, n-type organic semiconductors. The high stability and decent electron mobility make xylindein an attractive candidate for OFETs as well. OFETs were fabricated and tested in a variety of configurations with xylindein. Unfortunately, minimal switching behavior was observed, due to processing limitations. To bypass some of those limitations and take advantage of potential protonic conductivity in xylindein, organic electrochemical transistor (OECT) configurations were tested as well. Functioning transistors were fabricated using deionized water as a gating medium. Xylindein has the benefit not only of being environmentally friendly, but also non-toxic, which is important for biosensing applications, which OECTs and water gated transistors are commonly used for. Other electrolyte gates show redox activity that may point to potential use for xylindein in energy storage applications, which is currently under investigation.

A second research project discussed in this thesis focuses on hybrid light matter quasi-particles known as polaritons. Polaritons have been shown to exhibit interesting physical properties, which we hope to utilize in overcoming some of the bottlenecks

in organic (opto)electronics today, such as low stability and low charge carrier mobility. OFETs were further explored using 2,8-difluoro-5,11-bis(triethylsilylethynyl)anthradithiophene (diF-TES-ADT or ADT for short) as an active material. ADT has been shown recently to strongly couple to an optical cavity to form exciton polaritons, and is already well known as a p-type material for OFETs. Polariton states have been demonstrated theoretically to increase charge transfer and mobility in an organic semiconductor, thus have the potential to enhance (opto)electronic device performance. Interestingly, coupling can occur in an optical cavity in the absence of incident light, so it is theoretically possible to utilize polaritons in a conventional transistor in the dark, though there may be benefits to the operation of a phototransistor as well. Bottom gate top contact OFETs were fabricated with a fully reflective aluminum gate on the bottom, a top insulating layer on top of the active layer, and a thin aluminum layer on top as a partially reflective mirror to form an optical cavity. Some OFETs were left without the top aluminum layer as a control, and the bottom dielectric layer thickness was varied to give different cavity resonances. Transistor characteristics were measured along with phototransistor and photocurrent measurements to probe the effects of the optical cavity and polariton states induced in the devices.

(Opto)electronic Properties of Xylindein and Organic (Opto)electronic Devices

By

Gregory J. Giesbers

A DISSERTATION

submitted to

Oregon State University

in partial fulfillment of
the requirements for the
degree of

Doctor of Philosophy

Presented June 1, 2021
Commencement June 2021

Doctor of Philosophy dissertation of Gregory J. Giesbers presented on June 1, 2021.

APPROVED:

Major Professor, representing Physics

Head of the Department of Physics

Dean of the Graduate School

I understand that my dissertation will become part of the permanent collection of Oregon State University libraries. My signature below authorizes release of my dissertation to any reader upon request.

Gregory J. Giesbers, Author

ACKNOWLEDGEMENTS

The author would like to begin by thanking his many collaborators: T. Krueger, Dr. J. Van Schenck, R. Van Court, S. Vega Gutierrez, R. Kim, Dr. E. K. Tanyi, Dr. S. Robinson, Dr. C. Fang, Dr. L.-J. Cheng, Dr. C. Beaudry, Dr. K. Paudel, J. Morre, A. Kannegula, N. Hong, T. Sawyer, and Dr. J. Anthony for their assistance and support generating the research found in this work.

The author would also like to thank the following individuals for their direct assistance with device fabrication and data collection tools: R. Presley, Dr. B. Gibbons.

Next, the author would like to thank his coworkers: Dr. J. Van Schenck, N. Quist, W. Goldthwaite, C. Webber, N Auparay, R. Harrison, R. Grollman, and all of the undergraduate students in the lab for their assistance, support and stimulating discussion.

Additionally, the author would like to thank the National Science Foundation for their continuing financial support, without which this research could not have happened (NSF Grants: DMR-1808258, CBET-170509, CHE-1956431, and EECS-2025489). Finally, the author would like to thank Dr. O. Ostroverkhova for her instrumental support and mentorship; this work was only possible with her skillful guidance.

TABLE OF CONTENTS

TABLE OF CONTENTS (Continued)

Page

TABLE OF CONTENTS (Continued)

Page

TABLE OF CONTENTS (Continued)

Page

TABLE OF CONTENTS (Continued)

Page

LIST OF FIGURES

LIST OF FIGURES (Continued)

LIST OF FIGURES (Continued)

Figure Page

LIST OF FIGURES (Continued)

Figure Page

LIST OF FIGURES (Continued)

Figure Page

LIST OF TABLES

LIST OF APPENDIX FIGURES

DEDICATION

This work is dedicated to:
my parents, who raised me to be the person I am today;
my wonderful wife Lindsey, for all of your love, support, and patience;
and my dear children, who inspire me.

Preface

The broad scope of this work and the research of the author pertains to the physics of organic semiconductors. The low cost, solution processability, and tunability of organic semiconductors is desirable in a large number of (opto)electronic applications, and has sparked an increase in research and general interest over recent years. Dramatic progress has been made both in the performance of organic semiconductor devices, such as thin film transistors and solar cells, and the understanding of the underlying physical processes involved. The general goal of the research presented in this work is to further enrich that understanding to further the field of organic semiconductors and ultimately enable better organic (opto)electronic devices.

This work is divided into 8 chapters, most of which focusing on a fungi derived pigment called xylindein. Chapter 1 gives an introduction to the field of organic semiconductors, basic physical processes involved, current drawbacks and bottlenecks to applications, and proposed strategies to overcome those bottlenecks. Chapter 2 (adapted from Ref [A8]) gives an introduction to xylindein, initial findings on its optical and electronic properties, and a strategy for improving processability. After initial findings, variations were observed between different batches of xylindein Varying levels of contaminants, most likely secondary fungal metabolites, were found in the material. Chapter 3 (adapted from Ref [A6]) details efforts to minimize these impurities and quantify their effects. A simple purification method was developed to remove substantial amounts of these impurities. With better protocols for purity in place, a more in-depth study of the optical and electronic properties was conducted, as detailed in chapter 4 (adapted from Ref [A5]). The stability, charge transport mechanisms, photoconductivity and more were investigated to establish physical understanding of the material and guide device applications for xylindein and other materials. In order to gain insight into how the molecular structure of xylindein gives rise to its properties, a study was then conducted focusing on the hydroxyl groups present and the hydrogen bonding they enable. Chapter 5 (adapted from Ref [A1])

details a comparative study between xylindein and dimethylxylindein, which has the hydroxyl groups of xylindein replaced with methoxy groups. The hydroxyl groups are shown to be critical for stability and electrical conduction. (Opto)electronic device applications for xylindein are explored in chapter 6. In particular, organic solar cells, organic field effect transistors, and electrolytic gated transistors are fabricated and discussed, giving insight into which applications xylindein may be useful for, and giving more physical understanding that may point to more device applications. The chapter 7 is focused again on organic (opto)electronic devices, but as part of a second project unrelated to fungi-derived pigments. This project is focused on hybrid light-matter quasi particles called polaritons, and harnessing them to overcome some of the bottlenecks in organic (opto)electronic devices. This chapter describes organic field effect transistors fabricated with an optical cavity to induce polariton states. The effects of these polaritonic states on the characteristics and performance of the devices as transistors and phototransistors are studied. Finally, chapter 8 summarizes the work and provides an outlook.

Published Works Including the Author

[A1] **G. Giesbers**, T. Krueger, J. Van Schenck, R. Kim, R. Van Court, S. Robinson, C. Beaudry, C. Fang, O. Ostroverkhova,
"The role of hydroxyl groups in the photophysics, photostability, and (opto)electronic properties of the fungi-derived pigment xylindein"
The Journal of Physical Chemistry C 125 (12), 6534-6545 (2021)
DOI: 10.1021/acs.jpcc.0c09627

[A2] T. Krueger, **G. Giesbers**, R. Van Court, L. Zhu, R. Kim, C. Beaudry, S. Robinson, O. Ostroverkhova, C. Fang,
"Ultrafast Dynamics and Photoresponse of a Fungi-Derived Pigment Xylindein from Solution to Thin Films"
Chemistry – A European Journal 27 (18), 5627-5631 (2021) DOI: 10.1002/chem.202005155

[A3] E. Tanyi, N. Hong, T. Sawyer, J. Van Schenck, **G. Giesbers**, O. Ostroverkhova, and L. Cheng
"Strong Exciton-Plasmon Coupling in Dye-Doped Film on a Planar Hyperbolic Metamaterial"
Optics Letters (2020) DOI: 10.1364/OL.402210

[A4] R. C. V. Court, **G. Giesbers**, O. Ostroverkhova, and S. C. Robinson,
"Optimizing Xylindein from *Chlorociboria* spp. for (Opto)electronic Applications"
Processes 8 (11), 1477 (2020) https://doi.org/10.3390/pr8111477

[A5] **G. Giesbers**, J. Van Schenck, R. Van Court, S. Vega Gutierrez, S. Robinson, and O. Ostroverkhova,
"Xylindein: Naturally Produced Fungal Compound for Sustainable (Opto)electronics"
ACS Omega 4 (8), 13309-13318 (2019) DOI: 10.1021/acsomega.9b01490.

[A6] **G. Giesbers**, T. Krueger, J. Van Schenck, R. Van Court, J. Morre, C. Fang, S. Robinson, and O. Ostroverkhova,
"Fungi-derived xylindein: effect of purity on optical and electronic properties"
MRS Advances 4 (31-32), 1769-1777 (2019) https://doi.org/10.1557/adv.2019.269.

[A7] K. Paudel, **G. Giesbers**, J. Van Schenck, J. E. Anthony, and O. Ostroverkhova,
"Molecular packing-dependent photoconductivity in functionalized anthradithiophene crystals"
Organic Electronics 67, 311-319 (2019).

[A8] **G. Giesbers**, J. Van Schenck, S. Vega Gutierrez, S. Robinson, O. Ostroverkhova,
"Fungi-Derived Pigments for Sustainable Organic (Opto)Electronics"
MRS Advances 3, 3459-3464 (2018) DOI: 10.1557/adv.2018.446. Selected for press release in OSU Today.

[A9] J. Van Schenck, **G. Giesbers**, A. Kannegula, L. J. Cheng, J. Anthony, O. Ostroverkhova,
"Molecular Packing-Dependent Exciton and Polariton Dynamics in Anthradithiophene Organic Crystals"
MRS Advances 3, 3465-3470 (2018) DOI: 10.1557/adv.2018.471.

1: Introduction

1.1 A brief introduction to organic semiconductors

Historically, organic compounds were seen as insulators. In the 1950's, semiconductivity was discovered in a number of polycyclic aromatic compounds.[10,11] A breakthrough came in 1960 for the understanding of conductivity mechanisms in organic materials when it was discovered that charge carriers are produced at the electrodes and injected into the organic material.[12] Conductive polymers were first introduced in 1977 by Alan Heeger, Alan MacDiarmid, and Hideki Shirakawa,[13] a development that would later grant them the Nobel Prize in chemistry in 2000.[14] A number of organic electronic devices were developed in the 1980's, including organic field effect transistors (OFETs), organic light emitting diodes (OLEDs), and solar cells.[15–17] Since then, the performance of organic electronic devices and interest in organic semiconductors has increased dramatically. The current organic electronics market is valued at 46 billion as of 2019, forecast to more than triple by 2026.[18] The majority of this market is in display applications utilizing organic light emitting diodes, though other devices and applications are expected to grow as the technology becomes more commercially viable.

Organic semiconductors have a number of key advantages over their inorganic counterparts. They are typically low in cost, lightweight, readily deposited on flexible substrates, and solution processable. Solution processability is important as it allows for much cheaper manufacturing methods at lower temperatures. The lower processing temperatures allow a greater range of substrates, particularly flexible plastics that would melt at higher processing temperatures. Organic semiconductors can be printed onto flexible substrates for unique applications at a low cost. Organic semiconductors may have an environmental benefit as well. Many organic semiconductors are biodegradable, and they can be naturally and sustainably sourced. The ease of processing also means less energy usage. This is a relatively new field and the rich variety of organic chemistry means there are many possibilities to be

explored and potential for interesting physics and applications. There are certainly drawbacks to organics, and they are unlikely to completely replace inorganics for many applications, but there is a great deal of potential for them for applications that do not need the high performance of silicon.

1.2 Exciton and charge carrier dynamics

1.1.1 Structure

Organic semiconductor materials are hydrocarbons that may contain additional atoms such as nitrogen, sulfur, or oxygen in their structure. The core structure is a conjugated carbon backbone consisting of alternating single and double bonds binding the structure. These bonds arise from sp_2 hybridized atomic orbitals, which leave one free p orbital on each atom. These p orbitals are directed normal to the plane of the molecule, overlapping to form what is called a π-electron system, in which the electrons are delocalized. The size of the conjugated system dictates the energy at which the molecule absorbs light. The overlap between π-orbitals in adjacent molecules is critical in charge transport properties.

1.2.2 Optical properties

Upon absorption of light, an electron is raised from the highest occupied molecular orbital (HOMO) to the lowest unoccupied molecular orbital (LUMO). An exciton (electron hole pair) is formed. The electronic states in organic semiconductors can also couple to vibrational states from carbon-carbon stretching modes. Absorption from the ground state can occur into various vibrational modes of the excited state, resulting in a series of peaks in the spectrum referred to as a vibronic progression. Likewise, fluorescence transitions from the excited state can occur into multiple vibronic modes of the ground state. Transitions between states happen vertically (see Fig 1.1 (a)) since electronic transitions happen at a much faster time scale than shifts in nuclear positions. The probability of transition is proportional to the square of the

overlap in wave functions, a relation known as the Franck-Condon Principle. Transitions between adjacent vibrational states have a high degree of overlap and thus happen very quickly. A molecule in an excited state will quickly decay (on a picosecond time scale) to the lowest (vibrationless) excited state energy before fluorescence occurs (generally on a nanosecond time scale). Fluorescence thus occurs almost exclusively from the lowest excited state energy level, a principle known as Kasha's rule. This along with a roughly symmetric potential well results in mirror image absorption and fluorescence spectra (Fig. 1.1 (b)). The shift in nuclear positions of the molecule upon excitation (r_0-r_0' in Fig. 1.1 (a)) results in a difference in energy between the first (lowest-energy) absorption peak and the first (highest-energy) fluorescence peak called the Stokes shift. The Stokes shift often correlates to the rigidity of the molecule, and is directly related to the Huang-Rhys factor, a parameter that determines the relative height of each peak in a vibronic progression. These parameters are discussed in further detail in later chapters as they are used in the analysis of the optical properties of xylindein.

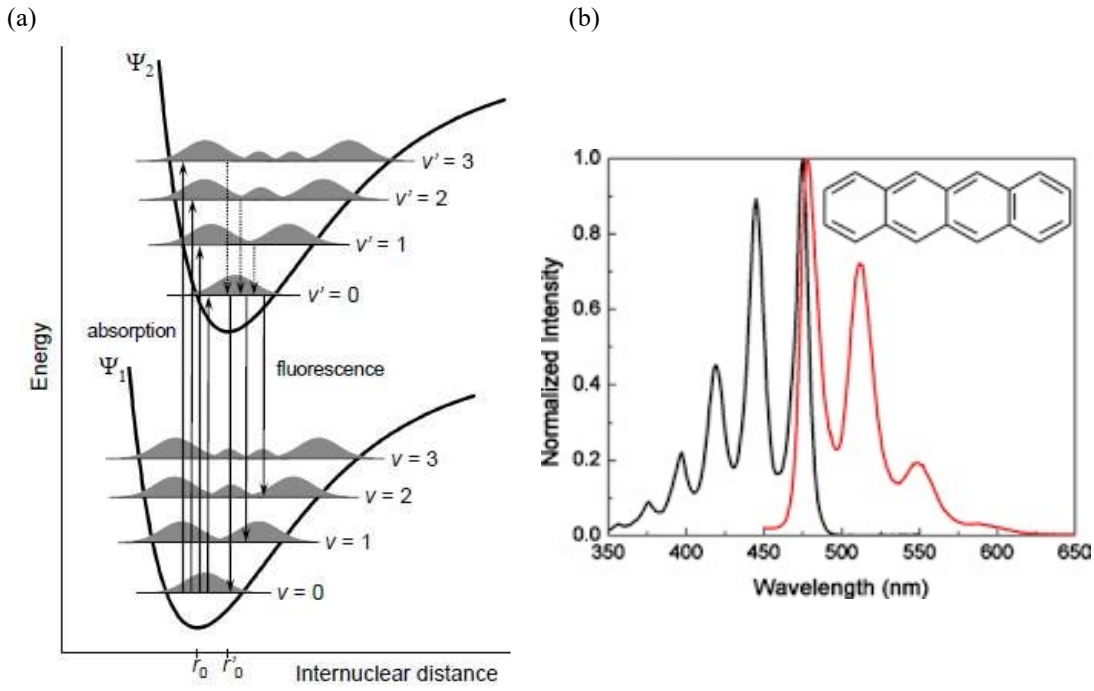

Fig. 1.1. (a) Energy diagram showing the potential energy wells for the ground (Ψ_1) and excited (Ψ_2) state and transitions. Vibrational levels are shown (ν and ν') and

wavefunctions are sketched. From Ref. [1] (b) Absorption and fluorescence spectra for tetracene in solution. From Ref. [2]

In a solid state, molecules are held together with weak van der Waals forces. Excitons are Coulombically bound with large binding energies of ~0.5-1.0 eV.[19] These Frenkel excitons as they are known are localized to the molecular backbone of the compound. Solid state spectra are often similar to that of an individual molecule aside from some broadening and (typically) a red shift resulting from intermolecular interactions.

1.2.3 Charge Transport

The weak intermolecular forces of organic semiconductors result in wavefunctions that are localized to a small group of molecules or a single molecule.[20] The degree of delocalization results in varying mechanisms of charge transport.[20] Disordered semiconductors such as polymers and amorphous small molecules have highly localized states; in these systems charge transport proceeds by hopping. In particular, charge carriers "hop" between a series of discrete states with varying energy levels due to the disorder in the material (see Fig. 1.2). Deep energetic states can act as charge "traps", preventing the charge carrier from participating in the transport. The conduction is thermally activated, meaning thermal energy assists in providing the extra energy to hop between sites. Conduction increases with increasing temperature in this matter, often modelled with an Arrhenius relation.[3] In highly ordered crystalline organic semiconductors, there is evidence of band-like transport,[21,22] similar to inorganic semiconductors, with an opposite trend in the temperature dependence.[22] Hopping transport is a good model for disordered and low mobility organic semiconductors, while band transport is better for highly ordered high mobility systems, but this is still an incomplete description and there are other models to appropriately describe the range of transport mechanisms in organic semiconductors.[19,20] The charge transport mechanisms of xylindein are studied and discussed in terms of hopping transport in Ch. 4-5.

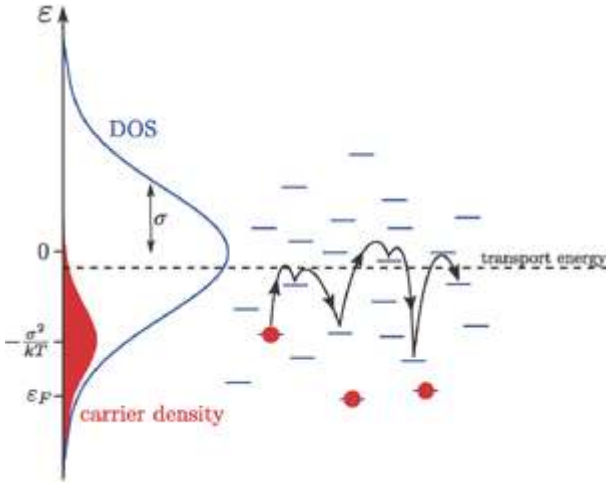

Figure 1.2. Thermally activated hopping transport mechanism. From Ref. [3]

Semiconductors in general can be n or p type, corresponding to the charge of the majority charge carrier: electrons for n-type and holes for p-type semiconductors. In organic semiconductor devices, these are sometimes combined, in which case they are referred to as "donors" and "acceptors". For example, in organic solar cells, an electron photoexcited in a donor molecule (p-type) donates an electron to an acceptor molecule (n-type). This will be discussed further in Ch. 7 for solar cells using xylindein as an acceptor.

Charge transport only occurs when the molecular unit is charged, which can occur in several ways: by injection at a metal interface, through electrochemical doping, or by dissociation of a neutral excited state.[19] Applications like OLEDs and OFETs generally rely on charge injection from the electrodes. It is important in these cases to match the work function of the electrodes to either the HOMO energy level (for a p-type material) or the LUMO energy level (for an n-type material) for proper charge injection. A mismatch can result in an energetic barrier that is detrimental to device performance. This work function matching is important for understanding and measuring charge transport properties, as applied to xylindein in Ch. 2-5, and in optimizing OFETs (discussed in Ch. 6-7).

1.3 Bottlenecks

Although organic semiconductors have several key advantages over inorganics, there are also limiting factors that need to be addressed for commercial viability of many device applications. The most important characteristics for creating commercially viable devices are performance (e.g. mobility in OFETs and power conversion efficiency in solar cells) and lifetime of the device, dependent on the stability of the materials.[23] Both of these factors can be problematic in organic semiconductors, and exploring novel organic electronic materials with enhanced stability is one of the major goals of the work described in this thesis.

1.3.1 Stability

Inorganic semiconductors are generally chemically stable and resistant to degradation from environmental factors such as light, heat, moisture, and oxidation. Unfortunately, this is not the case for organic semiconductors. For organic devices, degradation can occur as a deterioration of the active layer itself, degradation of the interface properties, or a mechanical breakdown of the device.[23] Many organic semiconductors that comprise the active layer of devices are susceptible to chemical reactions that will break the conjugated structure of the molecule, destroying the favorable (opto)electronic properties. Different device applications are exposed to different environmental stresses that make different forms of degradation more relevant, though most applications require at least some resiliency toward light and exposure to air. To quantify the issue, take Gevorgyan et al.'s metanalysis of organic photovoltaic stability, looking at device lifetimes reported from 2001-2015.[4] One can see that even in encapsulated devices stored in the dark, most devices are stable for no more than a matter of months (see Fig. 1.3 (a)). Devices tested under illumination (Fig. 1.3(b)) fare worse, and unencapsulated devices often last only for a matter of hours.

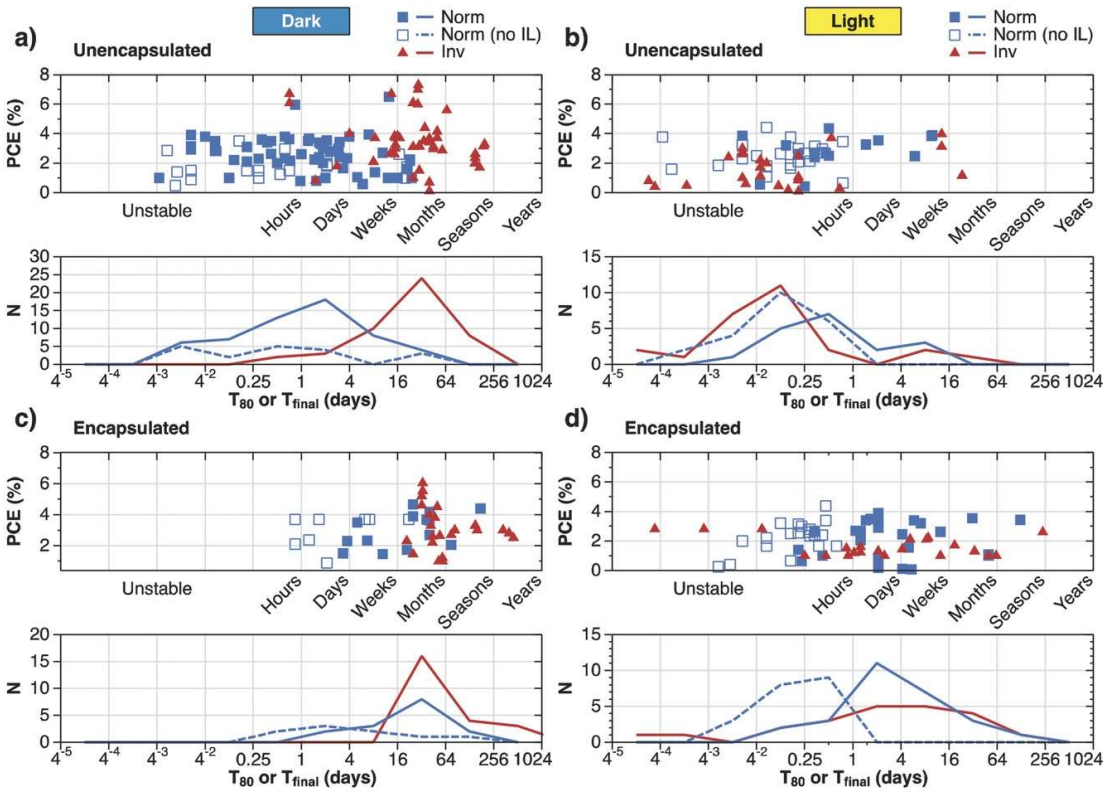

Figure 1.3. Distribution of the lifetime for unencapsulated (a,b) and encapsulated (c,d) samples with normal (blue squares) and inverted (red triangles) structures tested under illumination (b,d) and in the dark (a,c). Each data point corresponds to one aged sample reported in the literature. The open blue squares correspond to normal geometry devices where the top electrode is directly applied onto the PAL. The bottom plots show the distribution of the data in a histogram format, where the y-axis represents the number of the reported data points. From Ref. [4]

Degradation is a major problem in OFETs as well. For example, pentacene, a well-studied benchmark p-type organic semiconductor used in OFETs, is known to have low photo-oxidative stability.[24] There are examples of relatively stable p-type materials, though n-type materials lag behind in this respect.[25] N-type materials transport through the LUMO, and unless the material has a particularly low LUMO level, the electron in that state is at a high energy level that makes it susceptible to reactions with oxygen and H_2O.[25] This motivates work on xylindein, a n-type organic pigment with extraordinary stability with respect to environmental factors, described in Ch. 2-6.

1.3.2 Performance

Many organic electronic devices have performance issues as well. One of the key metrics in an organic semiconductor is the charge carrier mobility. Crystalline silicon, as a benchmark, has a mobility of around 1,000 $cm^2V^{-1}s^{-1}$.[19] Organic semiconductors are unlikely to ever replace silicon in applications where such high mobility is critical, though there are low-cost applications where organic semiconductors may be more advantageous. Amorphous silicon, which comes at a lower cost, is a common benchmark to compare to at 0.5-1 $cm^2V^{-1}s^{-1}$.[26] There are plenty of examples now of p-type organic semiconductors in excess of this benchmark, with reports up to 42.7 $cm^2V^{-1}s^{-1}$.[26] N-type organic semiconductors with high mobilities are much more uncommon, though progress is being made and there are reports of electron mobilities as high as 12.6 $cm^2V^{-1}s^{-1}$ for small molecules and 14.9 $cm^2V^{-1}s^{-1}$ for polymers.[25] However, there are also reports that some of the mobilities reported above 10 $cm^2V^{-1}s^{-1}$ are unreliable.[5] Since many applications rely on both p- and n-type semiconductors, it is important to have high performance in both. It is also important to note that high mobility cannot come at the expense of stability or cost for commercial viability. The work presented in Ch. 2-5 seeks to address the need for low cost, stable, high mobility materials through understanding and potentially utilizing the properties of xylindein.

1.4 Strategies

There is a massive amount of research effort devoted to increasing stability and performance metrics of organic semiconductors. Much of this work focuses on molecular design strategies. One strategy is to attach various side groups to a core structure in order to alter crystal packing, which can have dramatic effects on the optical and electronic properties.[27,28] Many such functionalization strategies have been employed to improve both stability and performance. For example, in benchmark acene derivatives, fluorine substitution on the acene molecular core is one common approach to improve both stability and performance.[24,29]

This thesis aims to explore a few innovative approaches to understanding and addressing the bottlenecks in organic semiconductors. One approach discussed is to employ hydrogen bonding (Ch.5), shown to greatly enhance photostability and be beneficial for charge transport.[30] Hydrogen bonding is one of the unique features of xylindein. Ch. 2-5 aim at understanding the mechanisms behind xylindein's stability and charge transport properties, including but not limited to hydrogen bonding. Another approach is to employ the unique properties of polaritons to potentially increase device performance (Ch. 7).[31,32]

Chapter 2: Fungi-Derived Pigments for Sustainable Organic (Opto)Electronics

Authors:

G. Giesbers, J. Van Schenck, S. Vega Gutierrez, S. Robinson, O. Ostroverkhova

MRS Advances (2018)

Journal Online Access

3, 3459-3464

2.1 Introduction

Organic semiconductor materials are of interest for use in optoelectronic applications due to their low cost, solution processability, and tunable properties. Among various classes of organic materials, over the past decade there has been a growing research effort focusing on green chemistry and on sustainable, natural product-derived materials for organic electronics.[33,34] Successful examples of the latter include indigo and Tyrian purple dyes, isoindigo, and diketopyrrolopyrrole derivatives which have been used in ambipolar organic field-effect transistors (OFETs) and donor-acceptor (D/A) solar cells.[35] Fungi-derived pigments are a naturally sourced, sustainable class of materials that are currently unexplored as organic semiconductor materials. We seek to explore this novel class of natural product-derived (opto)electronic materials, in this chapter focusing on a fungi-derived pigment xylindein, which is secreted from the fungi *Chlorociboria aeruginosa* and *Chlorociboria aeruginascens*. Wood stained with xylindein has been utilized by humans in decorative wood products since the 1400s; that the pigment remains blue-green in intarsia artwork aged 500+ years is a testament to its environmental durability.[36] However, optical and (opto)electronic properties of this pigment have not yet been characterized, and our initial efforts towards understanding these properties in xylindein and other fungi-derived pigments are presented here.

2.2 Experimental

2.2.1 Xylindein Culturing and Extraction

Xylindein is a spalting pigment produced by the wood-eating fungi, *Chlorociboria aeruginosa* and *Chlorociboria aeruginascens* (Fig 2.1(a)). We have developed a method for the reliable culturing, extraction, and purification of xylindein as described in our previous publications.[37–39] Briefly, *C. aeruginosa* is cultured on 10 cm plates in a 2% malt, 1.5% agar in water solution (Fig. 2.1(b)). Mature fungal materials are then transferred to bioreactors containing 2% malt in water. As the

fungal material secretes xylindein into the liquid media, some of the liquid is regularly collected and purified to yield the pigment (Fig. 2.1(c-e)).[39]

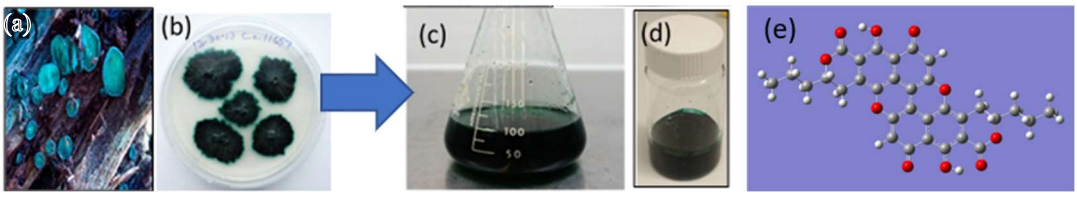

Figure 2.1. (a) Fruiting bodies of *C. aeruginosa*. (b) *C. aeruginosa* cultured on solid media. (c) *C. aeruginosa* secretes xylindein in liquid culture. (d) Xylindein purified from liquid cultures. (e) Molecular structure of xylindein.

2.2.2 Materials

The core structure of the xylindein molecule (Fig. 2.1(e)) is peri-xanthenoxanthene (PXX), derivatives of which were shown to exhibit hole mobilities of up to 0.9 $cm^2/(Vs)$[40,41] and explored by Sony for use in OFET-driven displays due to their unprecedented stability.[42] Promising electronic characteristics and stability, which has been previously demonstrated through prolonged exposure to UV light, electrical stress, and thermal stress,[43] motivates the choice of xylindein for this study. When deposited from solution, xylindein forms a highly disordered porous, amorphous solid which may be disadvantageous for electronic properties favorable for device applications, as well as their reproducibility. To gain improvement of morphology in the xylindein thin-film devices and enhance the quality of solution-deposited thin films, we introduced a transparent non-conductive polymer, poly(methyl methacrylate) (PMMA) as a host matrix and explored properties of xylindein:PMMA blends side-by-side with pristine xylindein films.[44]

2.2.3 Sample Preparation

Solid flakes of purified xylindein were mixed into chlorobenzene and tetrahydrofuran (THF) to form solutions of various concentrations. THF solutions in the 8-180 µM

range of concentrations were used for solution absorption measurements, and 10 mM and 25 mM chlorobenzene solutions were used for depositing films. For xylindein:PMMA samples, a 180 mM solution of PMMA in chlorobenzene was prepared and 10 µL of this solution was mixed with 180 µL of 10 mM xylindein solution to yield a composite solution containing xylindein and PMMA at a 1:1 molar ratio. All solutions were sonicated for at least 30 minutes. Pristine xylindein and xylindein:PMMA films were obtained by drop-casting corresponding solutions at room temperature onto interdigitated Au/Cr electrodes deposited on a glass substrate with a gap of 25µm.[45] Prior to film deposition, the substrates were sonicated in an acetone bath and rinsed with deionized water to eliminate foreign contaminants. Pristine xylindein films were studied using the x-ray diffraction (XRD) and scanning electron microscopy (SEM). The XRD confirmed an amorphous nature of films, and the SEM revealed porous structure with the pore sizes of up to ~1 µm.

2.2.4 Measurement Procedures

Optical absorption was taken at room temperature in air using an Ocean Optics USB-2000 spectrometer and an LS-1 tungsten halogen lamp. Electrical measurements were performed using a Keithley 237 source-measure unit. Current-voltage (I-V) characteristics were measured with a sweep in voltage increasing in 1 V increments from 1 V to 300 V and measuring the current output in a dark room at room temperature. Effective charge carrier (hole) mobilities were extracted from space-charge limited currents (SCLCs) using thin-film and half-space approximations as detailed in Ref. [45]. Current in the presence of a 633 nm 1.3 mW illumination from a HeNe laser was measured at a constant voltage (100 V) as follows. Voltage was applied, and dark current was recorded for 5 seconds. Then, the light was turned on with a shutter and the current under illumination was measured as a function of time. The photocurrent was calculated as the difference between the two, and the photosensitivity was obtained by dividing the photocurrent by the dark current. In order to make comparisons of the photosensitivity between the samples with different optical densities, photosensitivity per absorbed photon was calculated as the

photosensitivity divided by (1-10-OD), where OD is the optical density obtained from absorption spectra of films at 633 nm.

2.3 Results and Discussion

2.3.1 Optical Properties

Optical absorption spectra of xylindein in solutions of various concentrations, in pristine film, and in xylindein:PMMA film are shown in Figure 2.2. The absorption spectrum of xylindein in all solutions features a dominant peak at ~670 nm and a structure consistent with vibronic progression due to exciton coupling to C-C stretching modes similar to that observed in many organic semiconductor molecules such as acenes or acene-thiophenes.[46] The xylindein and xylindein:PMMA film absorption spectra (Fig. 2.2(b)) exhibit less pronounced vibronic progression features as compared to those in solution due to disorder-induced peak broadening. Additionally, they exhibit a new band at ~720 nm. The 720 nm band also occurs in solutions at higher concentrations (Fig. 2.2(a)), which suggests that it is due to aggregate formation.[44] The nature of these aggregates, which involve an interplay between intermolecular hydrogen bonding[47] and π-π stacking of xylindein molecules, is currently unknown and needs further investigation. The wide range of absorption in films extending to the near-infrared (IR) wavelength region obtained in films is beneficial for (opto)electronic devices such as D/A bulk heterojunction (BHJ) solar cells and applications specifically relying on the optical response in the near-IR.[48]

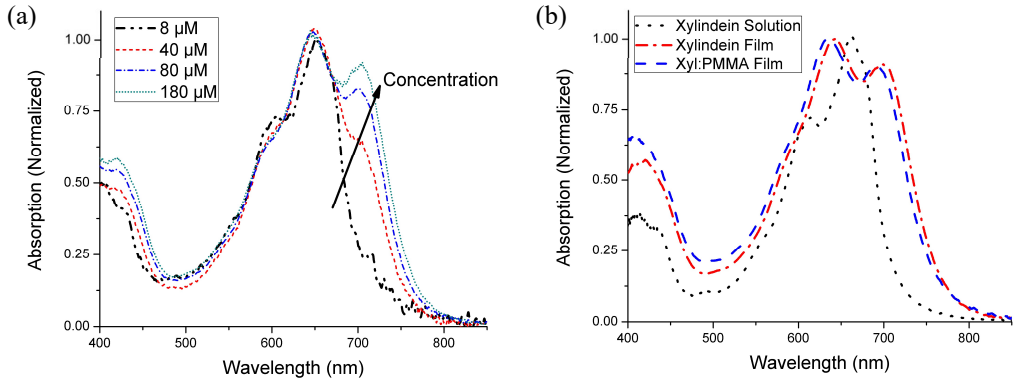

Figure 2.2 Normalized absorption spectra for (a) 8-180 μM xylindein in THF solutions and (b) drop-cast films of xylindein and xylindein:PMMA (1:1).

2.3.2 Electrical Properties

Xylindein films have been previously shown to exhibit an effective charge carrier (hole) mobility of up to 0.53 $cm^2/(Vs)$ despite un-optimized deposition conditions and poor morphology.[43] Given that pristine xylindein tends to form non-uniform films with an amorphous porous structure with current deposition techniques, an important step to the use of xylindein in (opto)electronic devices is to understand how film deposition method affects the performance and to improve film morphology.[49] We found that mobility obtained from drop-cast xylindein films varies by several orders of magnitude depending on the concentration of the solution used in film preparation, and solutions with higher xylindein concentrations produce thicker films characterized by higher values of mobilities. The solution concentrations and preparation method reported here yielded xylindein films with hole mobilities on the order of 10^{-3} $cm^2/(Vs)$. One strategy to improve film quality and enhance solution processability of small-molecule organic semiconductors has been to create blends of the organic semiconductor molecule with an amorphous polymer.[50] This strategy has proved successful for organic semiconductor molecules with a strong tendency to crystallize (such as anthradithiophene (ADT) derivatives), as enhanced mobility in ADT:polymer blends was obtained (as compared to that in pristine ADT films) due to reduced charge trap densities.[50] Aiming to achieve a similar goal, we introduced

PMMA as a polymer host matrix, to fill in the pores of the native xylindein and create more uniform films.[44] Given the non-conductive property of PMMA, it is then important to determine the possible trade-off between the film quality and its electrical characteristics which we discuss next.

Side by side comparison of I-V curves of xylindein and xylindein:PMMA films obtained using the same xylindein solutions for deposition show similar electrical characteristics (Fig. 2.3(a)). Both films experience a shift to the SCLC regime, where the I-V curve switches from linear to quadratic, at ~120 V. For the samples in Fig. 2.3(a), the effective charge carrier (hole) mobilities extracted from the slopes of a linear fit to a plot of current versus the square of voltage in the SCLC regime (inset of Fig. 2.3(a)) yielded 4.2 x 10^{-3} (9.5 x 10^{-3}) $cm^2/(Vs)$ and 4.6 x 10^{-3} (1.0 x 10^{-2}) $cm^2/(Vs)$ in pristine xylindein and xylindein:PMMA samples, respectively, in thin-film (half-space) approximations.[45] Similarity of the mobility values obtained in pristine xylindein and xylindein:PMMA films is promising for creating uniform thin-film devices with enhanced processability based on xylindein:polymer blends.

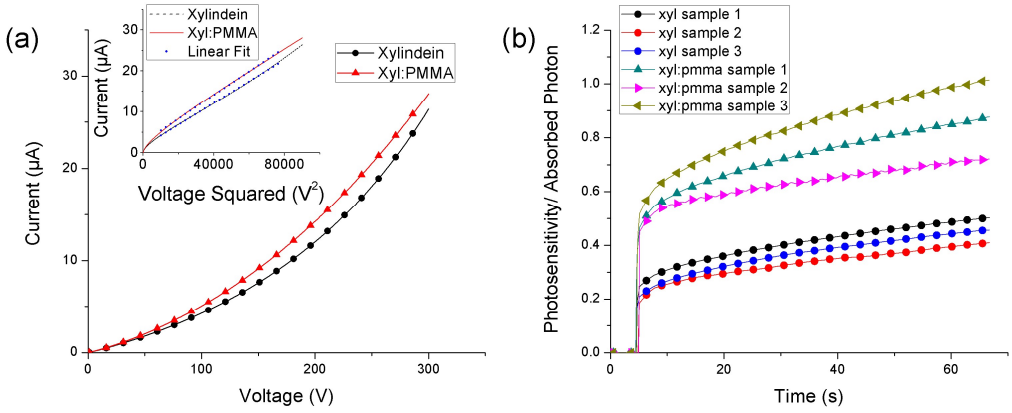

Figure 2.3. (a) Current-voltage characteristics from a 1-300V voltage sweep for a pristine xylindein film and a xylindein:PMMA (1:1) film. Inset shows the same curves plotted against the square in voltage with a linear fit in the SCLC regime from which effective hole mobilities are obtained. (b) Photosensitivity per absorbed photon for three pristine xylindein films and three xylindein:PMMA films on interdigitated Au/Cr electrodes obtained at an applied voltage of 100 V and 633 nm 1.3 mW laser illumination initiated at t=5 seconds.

Furthermore, the xylindein:PMMA films exhibited a stronger photoresponse in the visible spectral range as compared to pristine xylindein films (Fig. 2.3(b)). Comparing three xylindein films with three xylindein:PMMA films made from the same xylindein solution with identical processes, we observed a factor of ~2 increase in the photosensitivity per absorbed photon in the xylindein:PMMA films. Since PMMA is transparent in the visible wavelength range, it does not directly contribute to the enhanced photosensitivity at 633 nm observed here. Given that charge carrier mobilities in these xylindein and xylindein:PMMA samples are comparable, the observed increase in photosensitivity indicates an improved charge photogeneration efficiency. This suggests that the film morphology achieved in xylindein:PMMA blends favors a reduced efficiency of geminate recombination as compared to that in pristine xylindein films. Establishment of the exact mechanism behind this observation and its potential utility for polymer:xylindein D/A BHJ solar cells will be a subject of our future investigation.

2.4 Conclusion

Optical absorption measurements reveal aggregate formation, manifested via an appearance of a ~720 nm absorption band, red-shifted from the spectra of dilute solutions, in solutions with higher concentrations and in films as compared to dilute solutions. The nature of such aggregates that are created by an interplay of intermolecular hydrogen bonding and π-π stacking requires further investigation. Addition of PMMA to pristine xylindein is a promising route to improve the film morphology and solution processability without detriment to the electrical characteristics of the film. Charge carrier (hole) mobilities on the order of 10^{-3} $cm^2/(Vs)$ were obtained both from pristine xylindein and xylindein:PMMA films. A factor of ~2 improvement in photosensitivity was observed in xylindein:PMMA films as compared to pristine xylindein films, due to an enhanced charge generation efficiency caused by an improved film morphology. The mechanism of this enhancement and how it could be used in (opto)electronic thin-film devices incorporating xylindein will be explored in our future work.

Chapter 3: Fungi-derived xylindein: effect of purity on optical and electronic properties

Authors:

G. Giesbers, T. Krueger, J. Van Schenck, R. Van Court, J. Morre, C. Fang, S. Robinson, and O. Ostroverkhova

MRS Advances (2019)

Journal Online Access

4(31-32), 1769-1777

3.1 Introduction

Organic semiconductors are of considerable interest due to their low cost, tunability, and solution processability.[35] Over the past decade, there has been a growing interest in naturally sourced and sustainable organic materials for (opto)electronic applications.[51] Naturally derived pigments exhibit extraordinary stability with respect to a variety of environmental factors,[52–54] which is important since low stability is one of the bottlenecks preventing wide commercialization of organic semiconductor devices. Additionally, when implemented in electronic devices some of the pigments performed surprisingly well in spite of an only partially conjugated core structure.[52,55] One of the promising naturally sourced pigments for organic electronics is xylindein, secreted by the non-pathogenic wood-staining fungi *Chlorociboria (C.) aeruginosa* or *C. aeruginascens*. We recently reported the optical and electronic properties of xylindein,[56,57] amorphous films of which exhibited electron mobilities of up to 0.4 $cm^2/(Vs)$. Furthermore, xylindein considerably outperformed benchmark organic semiconductors in terms of the photostability in air.[57] Similar to many natural products, naturally sourced xylindein requires extraction from liquid cultures and subsequent purification. Purification procedures may lead to a low yield of the purified material, thus reducing its utility for device applications. Depending on the purification protocol, this may become a time-consuming and costly process. Therefore, it is important to understand how various degrees of purification affect electronic properties and to develop less time-consuming and wasteful purification methods. In this paper, we implement a simple purification method and compare optical and electronic properties of xylindein before and after purification.

3.2 Experimental

3.2.1 Xylindein Extraction

Xylindein was harvested from wood collected at Tidewater, Oregon, USA (Fig. 3.1(a)). Appropriate wood was identified by the signature blue-green color produced

by *Chlorociboria* species, which is unique across several kingdoms. The *Chlorociboria* species responsible for staining the wood was identified as *C. aeruginosa* through DNA extraction and Sanger sequencing of the ITS region, followed by GenBank Megablast comparison.[58] The collected wood was crushed into 2-3 mm fragments and the powder was placed in a 500 mL flask so that the bottom of the flask was evenly covered. 100 mL of dichloromethane (DCM) was poured into the flask and the contents were stirred on a magnetic plate for one hour before filtration as described in Ref. [59]. The solid crude xylindein was collected from evaporated DCM solution. When used without further processing, it will be referred to as "pre-wash" sample and its properties will be compared to a "post-wash" sample prepared as described below. The solid xylindein prepared as the "pre-wash" xylindein was sonicated in ethanol to form a suspension of xylindein aggregates. The ethanol solution was passed through a 0.45 μm PTFE filter, followed by multiple passes of clean ethanol through the filter to remove contaminants; the solution of contaminants in ethanol will be referred to as "ethanol wash" (Fig. 3.1(b)). The xylindein was removed from the filter with DCM, and solvents were evaporated to yield "post-wash" xylindein powder. The "post-wash" xylindein re-dissolved in DCM is shown in Fig. 3.1(c) and xylindein molecular structure in Fig. 3.1(d).

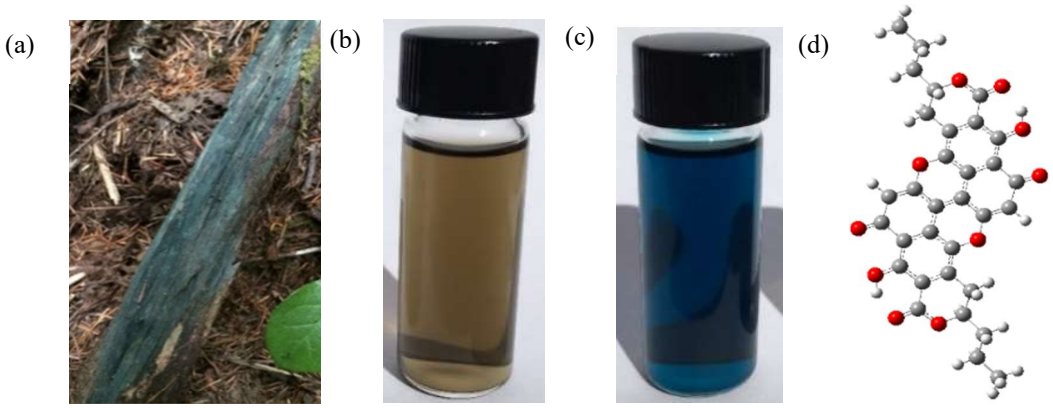

Figure 3.1: (a) *C. aeruginosa* producing blue-green pigment xylindein on the decaying wood. (b) "Ethanol wash" sample - contaminants in ethanol, washed away

from xylindein extracted from the wood. (c) “Post-wash” sample - purified xylindein solution in DCM, after ethanol wash. (d) Molecular structure of xylindein.

3.2.2 Mass Spectrometry

Analyses were performed on a Shimadzu HPLC (Columbia, MD) coupled to a Waters Synapt HDRMS time of flight mass spectrometer (Milford, MA). The MS was operated in negative ion mode, 80-1000 m/z scan range, 1 second scan time. A binary gradient and a 2.5 mm 2.1 x 50 mm c XTerra® MSC8 column (Waters, Milford, MA) were used for analytical separation. Solvent A consisted of MS grade water (Fisher Scientific, Fairlawn, NJ) and 0.1% formic acid (EMD Millipore Corporation, Billerica, MA) and solvent B consisted of MS grade acetonitrile (Fisher Scientific, Fairlawn, NJ) and 0.1% formic acid. “Pre-wash” and “post-wash” xylindein samples in DCM, along with the “ethanol wash” sample, were tested at 1:30 dilution.

3.2.3 Sample Preparation

Xylindein powder was dissolved into DCM to form solutions of concentration 10 mg/mL. For optical measurements, the solutions were further diluted with DCM to achieve appropriate optical density for the spectroscopic apparatus. Films were prepared by drop-casting the concentrated solution onto glass substrates with planar Al electrodes with a 50 μm gap. The substrates were patterned using conventional lift-off photolithography, and Al was deposited using a Veeco 7700 thermal evaporator. The drop-cast xylindein films were approximately 3-5 μm thick, as measured by an Alpha Step 500 profilometer.

3.2.4 Measurement Procedures

The steady-state absorption measurements were taken using a Thermo Scientific Evolution 201 UV/Visible (UV/Vis) spectrophotometer at room temperature. The path length of the quartz cuvette (1-Q-1, Starna Cells, Inc.) used for the absorption measurements was 1 mm, and the OD for both the “pre-wash” and “post-wash” xylindein solutions was 0.5 at 656 nm following a background/baseline measurement of pure DCM solvent.

The steady-state fluorescence measurements of the “pre-wash” and “post-wash” samples were performed using a Shimadzu RF-6000 Spectro Fluorophotometer at room temperature with 400 nm excitation. The path length of the 4-sided rectangular quartz cuvette used for the emission measurements was 5 mm. The excitation and emission slit- widths were both set to 5 nm. Additional fluorescence measurements were taken using an Ocean Optics USB2000-FLG spectrometer with 532 nm excitation from a frequency- doubled Nd:YVO_4 laser.

For measurements of current-voltage characteristics, voltage was applied to the samples using a Keithley 237 source-measure unit. Current was measured as a function of applied voltage in the 0-10 V range, under ambient conditions in the dark.

3.2.5 Density Functional Theory (DFT) Calculations

In order to calculate the vertical transition energies for the two molecular tautomers of xylindein (Fig. 3.2), both configurations were optimized in the electronic ground state using DFT methods in Gaussian 16.[60] The B3LYP functional with the basis set 6- 311++G(d,p) and a polarizable continuum model for DCM solvent were used. The energies of vertical transitions into each of the first 50 excited states were then calculated using time-dependent (TD)-DFT methods along with their associated oscillator strengths. Due to molecular symmetry, most of these vertical transitions are forbidden, leading to zero oscillator strength; all the allowed transitions are shown in Fig. 3.2.

3.3 Results and Discussion

3.3.1 Effect of Contaminants on Optical Properties

Figure 3.2 shows the optical absorption spectrum of a dilute solution of “post-wash” xylindein in DCM. The complicated structure of the S0-S1 part of the spectrum (600-750 nm) was analyzed in our previous publication[57] and attributed to a joint contribution of two vibronic progressions resulting from two xylindein tautomers (Fig. 3.2), wherein tautomer 1 has the hydroxyl groups pointed toward the conjugated core and tautomer 2 has the hydroxyl groups pointed away from the core. In order to

better understand the xylindein spectrum in the UV/Vis wavelength range, we calculated vertical energies and oscillator strengths of both tautomers for transitions from the ground state to several electronic excited states. Figure 3.2 shows the calculation result (which includes only the 0-0 lines and thus excludes the contribution of vibronic satellites to the spectra) superimposed with the experimental data. The calculated energies of the S_0-S_n transitions are slightly blue-shifted from the experimental values (e.g. by 10 and 18 nm, or 0.03 and 0.05 eV, for the S_0-S_1 transitions for the tautomers 1 and 2, respectively[57]). Nevertheless, the calculations help us understand what spectral features should be expected from xylindein molecules.

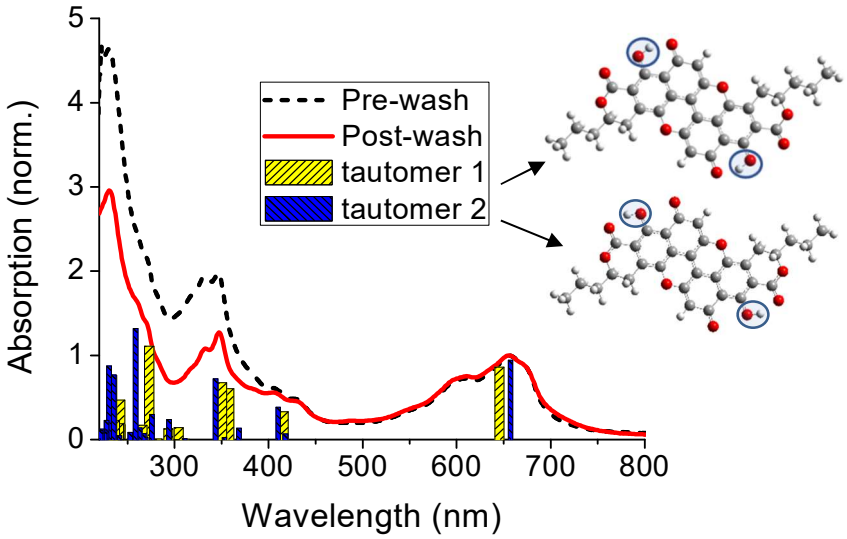

Figure 3.2: UV/Vis absorption spectra of xylindein before and after ethanol wash, overlaid with the 0-0 vertical transition energies determined from TD-DFT calculations for the two tautomers 1 (top) and 2 (bottom) of xylindein, shown on the right.

Figure 3.3 shows a comparison between the optical absorption spectra (a) and photoluminescence (PL) spectra (b) obtained from “pre-wash” and “post-wash”

xylindein solutions. While the absorption in the 500-700 nm region corresponding to that from the S_0-S_1 transition of xylindein remains unchanged, a dramatic reduction in the UV- absorbing species (which will be referred to as contaminants) was observed as a result of the ethanol wash (Figure 3.2). The PL of xylindein occurs in the ~680-800 nm wavelength region (Fig. 3.3(a)) and is very weak, with a quantum yield of <0.1%.[57] A considerably stronger PL was observed from contaminants in the "pre-wash" sample, occurring in the broad (400-600 nm) spectral region upon 400 nm excitation. The ethanol wash substantially reduced the PL from the contaminants by nearly 75% (relative to the "pre- wash" sample), although it did not eliminate it completely as seen from Fig. 3.3(b).

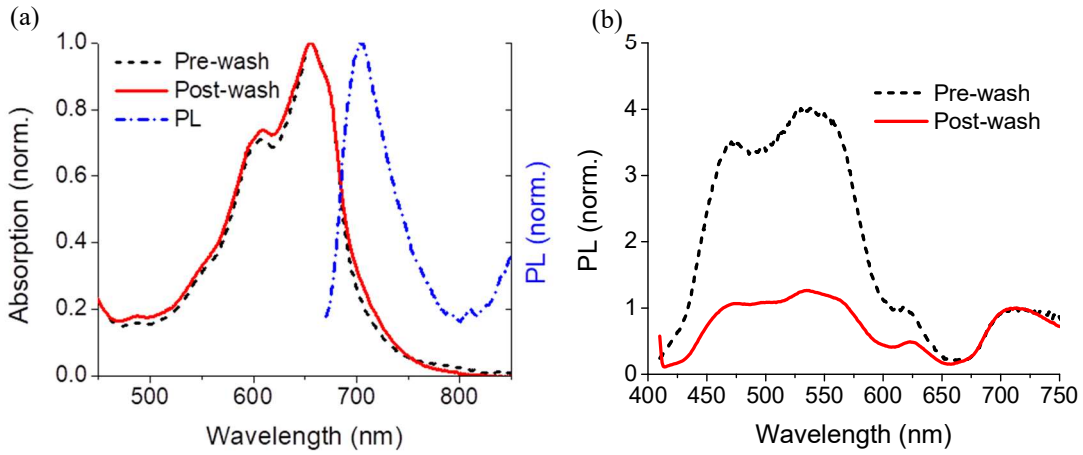

Figure 3.3: (a) Normalized absorption spectra before and after the ethanol wash, exhibiting negligible change in absorption in the spectral region corresponding to the S_0-S_1 excitation of xylindein. PL spectrum of xylindein obtained upon 532 nm excitation of the "post-wash" sample is also shown. (b) Emission spectra before and after ethanol wash upon 400 nm excitation, normalized at 712 nm, exhibiting a large discrepancy in PL from contaminants mainly responsible for emission below ~600 nm.

3.3.2 Effect of Contaminants on Electrical Properties

Figure 3.4 shows a comparison between electronic properties of films made from "pre-wash" and "post-wash" xylindein solutions as described in the Experimental. An increase in the current of more than 2 orders of magnitude was observed in samples made with a "post-wash" xylindein. The electron mobilities were calculated from the space-charge-limited current (SCLC) regime of the I-V characteristics (when $I \sim V^2$), in the thin-film approximation[45,57] (Eq. (3.1)).

$$j = \frac{2\mu_{eff}\epsilon\epsilon_0}{\pi}\frac{V^2}{L^2} \tag{3.1}$$

Here j is the linear current density, j = I/d, where I is the measured current and d is the length of the electrode. V is the applied voltage, L is the gap between the electrodes, ε_0 is the vacuum permittivity, ε is the dielectric constant (assumed to be equal to 3), and μ_{eff} is the effective electron mobility. The effective mobilities yielded 1.6 x 10^{-3} $cm^2/(Vs)$ and 0.19 $cm^2/(Vs)$ in the "pre-wash" and "post-wash" samples, respectively. The relatively high charge carrier mobility in the amorphous films of the "post-wash" samples could be indicative of a beneficial interplay between the π-π stacking and hydrogen bonding[55,61] which are both expected in a xylindein solid, for efficient charge transport. Films deposited from the "ethanol wash" solution of contaminants exhibited negligible conductivity.

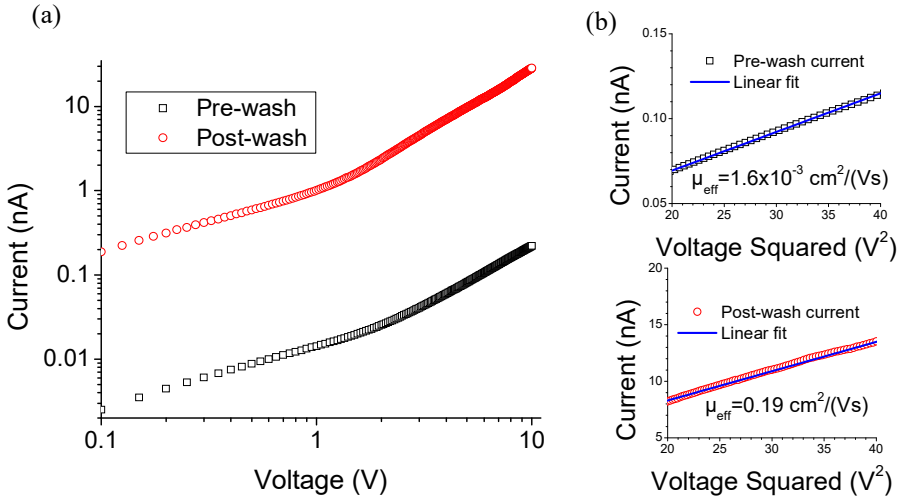

Figure 3.4: (a) Current-voltage (I-V) characteristics for the “pre-wash” and “post-wash” xylindein film on coplanar Al electrodes with a 50 μm gap, showing transition from the linear to the quadratic (SCLC) regime. (b) SCLC data from (a) replotted as I versus V^2 for the “pre-wash” (top) and “post-wash” (bottom) samples. Fits from which the effective mobilities were calculated are also included.

3.3.3 Nature and Properties of Contaminants

Next, we sought to understand the nature of contaminants that play such a dramatic role in conductive properties of xylindein-based films. Towards that goal, we analyzed mass spectra of “pre-wash” and “post-wash” xylindein samples, as well as of the “ethanol wash” containing contaminants. Negative ion analysis showed clear differences in peaks between the “pre-wash” and “ethanol wash” samples when compared to the “post-wash” samples. An initial peak which eluted at retention time of ~2.3 min was present in the “pre-wash” and “ethanol wash” samples, but not in the “post-wash” xylindein sample (Fig. 3.5(a)). The dominant mass peak at this elution time, not present in the “post-wash” sample, had a mass of 227.0926. Xylindein was observed at 11.1 minutes at a mass of 567.1268, with a -4.1 ppm mass accuracy corresponding to the (M - H)- ion, in accordance with the molecular formula of $C_{32}H_{23}O_{10}$.[62,63] A further peak present in the “pre-wash” and “ethanol wash” samples, but greatly reduced in the “post-wash” sample was at ~12.9 min, associated with a dominant mass of 573.1976. At 13.1 min, the dominant mass peak in the “pre-wash” and “ethanol wash” samples, but not the “post- wash” sample, had a mass of 573.1713 (Fig. 3.5(b)). At ~15.7 min, multiple peaks were present in the “pre-wash” and “ethanol wash” samples, but not in the “post-wash” sample. Most notable mass peaks that showed distinct differences between the “pre- wash” and “post-wash” samples were 349.2379, 368.3214, and 411.227. As there are several candidates for the responsible molecules, including various fungal secondary metabolites, information on the mass alone is not sufficient for reliable identification and the exact

assignment will be performed in future studies. However, based on the optical and PL properties of these contaminants and the procedure leading to their effective removal, we hypothesize that these are polar molecules with a considerably reduced conjugation length as compared to that of xylindein.

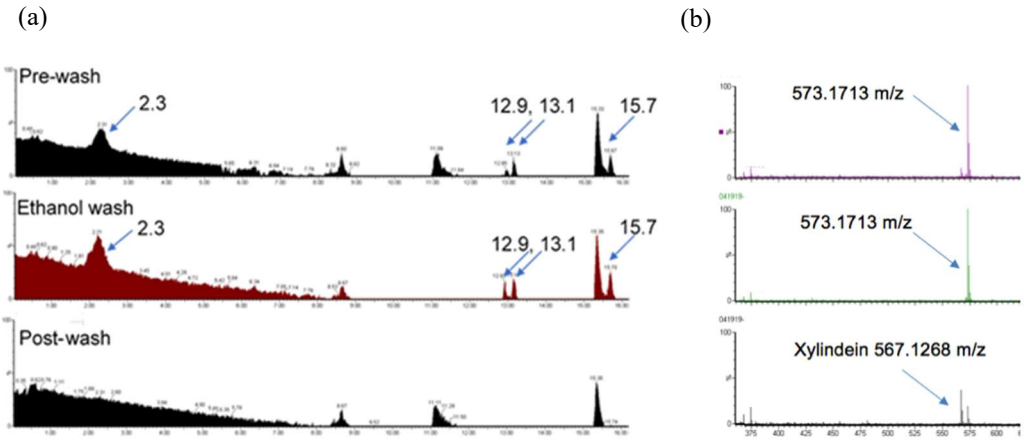

Figure 3.5: (a) Mass spectroscopy chromatogram of "pre-wash" and "post-wash" xylindein samples (top and bottom), as well as the "ethanol wash" (middle). Four peaks present in "pre-wash" and "ethanol wash" samples, with retention times (in minutes) denoted by arrows, were absent in the "post-wash" sample. (b) Masses at retention time of 13.1 min, including the peak corresponding to xylindein (highlighted in the "post-wash" sample, bottom). Also highlighted is the dominant contaminant peak with mass of 573.1713 m/z in the "pre-wash" (top) and "ethanol wash" (middle) samples.

Regardless of the exact molecular structures of the contaminants removed by the ethanol rinse, we surmise that they disrupt the conductive network of xylindein aggregates by introducing charge traps and non-conductive linkers. In particular, introduction of the fungi secondary metabolite molecules in the xylindein-based films would considerably disrupt both π-π stacking and hydrogen bonding between the xylindein molecules, which determine charge transport properties of xylindein films. To better understand the trade-off between a significantly improved electronic

performance and the production costs of purification, more studies correlating purification protocols with subsequent effects on optical and electronic properties are necessary to quantify the corresponding changes in the charge carrier mobilities and in mechanisms of conduction. These are currently underway and will be reported elsewhere.

3.4 Conclusions

Dramatic effects from an ethanol wash on the optical and electronic properties of the xylindein solution precursor and xylindein-based thin films, respectively, were observed. Considerably reduced UV absorption and PL at below 600 nm were obtained in “post-wash” solutions as compared to “pre-wash” solutions. These changes were correlated with a two orders of magnitude enhancement in charge carrier mobility in films drop-cast from “post-wash” solutions as compared to those from “pre-wash” solutions. Mass spectrometry revealed several contributors, hypothesized to be fungal secondary metabolites, responsible for these observations. Removal of these molecules, which serve as contaminants in “pre-wash” xylindein-based devices that disrupt the π-π stacking and hydrogen bonding between xylindein molecules, dramatically increases conductivity of xylindein-based films. Studies correlating further purification protocols and electronic properties of xylindein-based films are underway.

Chapter 4: Xylindein: naturally produced fungal compound for sustainable (opto)electronics

Authors:

G. Giesbers, J. Van Schenck, R. Van Court, S. Vega Gutierrez, S. Robinson, and O. Ostroverkhova

ACS Omega (2019)

Journal Online Access

4 (8), 13309-13318

4.1 Introduction

Organic (opto)electronic materials are of interest due to their low cost and tunable properties;[23] a broad range of their applications, from photovoltaics to three-dimensional (3D) displays, have been demonstrated.[35] Solution processable materials that can be cast into thin films using various solution deposition techniques are especially advantageous.[64] One of the bottlenecks that complicates organic materials processing and device fabrication, as well as hinders commercialization, is their relatively low stability with respect to photo- and/or thermal degradation. Therefore, organic (opto)electronic materials that exhibit enhanced stability are of considerable interest.

Over the past decade, there has been a considerable research effort focusing on sustainable, natural product-derived materials for organic electronics. These include biodegradable and biocompatible substrate materials (e.g. polyester elastomers), polymer dielectric and electrodes, and plant- or animal-derived active layers.[51,55,65] Examples of the latter include carotenoids, porphyrins, and anthraquinone derivatives, with the most successful examples being the indigo and Tyrian purple dyes,[51–53] which exhibited ambipolar charge transport with balanced organic field-effect transistor (OFET) carrier mobilities of 0.3-0.4 $cm^2/(Vs)$ in crystalline films. Additionally, indigo's structural isomer, isoindigo, has been used as a building block for D/A oligomers and co-polymers serving as donors in BHJ organic solar cells with PCEs of up to 8.2%.[66] Another successful example is animal-derived diketopyrrolopyrrole (DPP) derivative used as building block in D/A copolymers with OFET charge carrier mobilities of 10-12 $cm^2/(Vs)$.[67] Moreover, some derivatives such as quinacridone (derived from naturally occurring acridone) exhibited extraordinary photoconductive properties: an external quantum efficiency (EQE) of 10% in a single-layer Schottky diode, three orders of magnitude higher than that in benchmark pentacene films in a similar device geometry.[68] Success of the derivatives of natural origin, and with unconventional molecular structure, has been referred to as an exciting paradigm shift from the traditional requirements of an organic semiconductor molecule to necessarily possess a fully π-conjugated core, instead focusing on

importance of H-bonding for photophysics and molecular packing.[65] Additionally, many of such "unconventional" derivatives exhibited an enhanced stability with respect to environmental factors,[54,69] thus addressing a major issue of performance degradation in organic electronics. An example of "unconventional" and highly stable molecule of potential interest for organic electronics is xylindein, which is a blue-green pigment (Fig. 4.1) secreted by the non-pathogenic wood-staining fungi *Chlorociboria (C.) aeruginosa*.

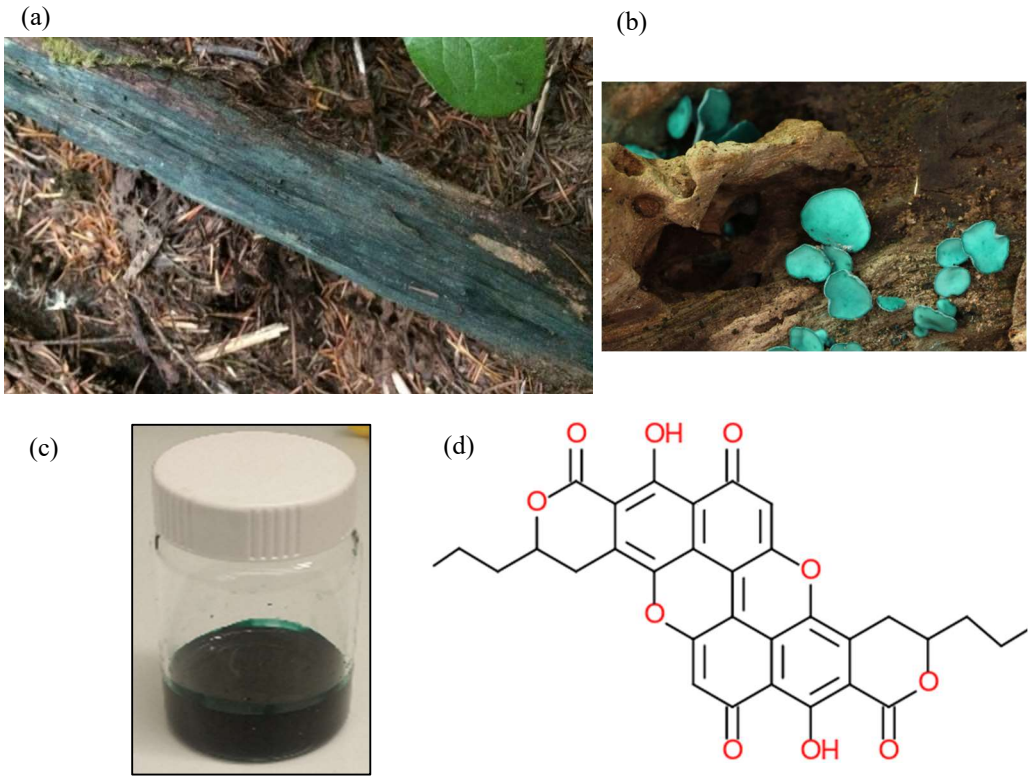

Figure 4.1. (a) and (b): *Chlorociboria aeruginosa* producing blue-green pigment xylindein on the decaying wood. (c) Extracted pigment in solution. (d) Molecular structure of xylindein.

Many fungi produce pigments for use in resource capture/territorial defense, ultraviolet (UV) resistance, and prevention of desiccation. Only a very select group of fungi, generally the wood soft-rotting fungi in the Ascomycetes, produce pigments that can penetrate deeply into wood.[70] These special pigments, referred to as 'spalting' pigments, have anti-fungal properties and are secreted by fungi to defend

territory (the wood matrix) while they grow into the substrate. Spalting fungi generally grow very slowly, and the distribution of the pigment into the wood allows them the time they need to colonize. Since it can take years for a given spalting fungus to colonize a log, the pigment it makes must be stable – under UV light, in water, heat, and other extreme environmental conditions. Their persistence is well documented - the blue-green pigment xylindein of Fig. 4.1 can be found in intarsia and marquetry woodworks as far back as the 1400s, still as vibrant as samples collected today.[71,72] The two *Chlorociboria* species *C. aeruginosa* and *C. aeruginascens*, both of which produce xylindein, have worldwide distribution and the wood stained by their colonization is readily available in the Pacific Northwest of the United States, among many other regions. Though pigment generation is slow in the wild, it can be significantly increased under laboratory conditions, and requires only standard 2% malt agar substrates (with some added sterilized, rotted wood) for growth.[37,39,73] No additional heat, nutrients, or movement is required.
Recently, we specifically demonstrated that xylindein shows extraordinary stability under UV excitation and self-healing capabilities.[74] Current interest in xylindein revolves primarily around the controlled introduction of the pigment into high-value wood products for aesthetic purposes.[39,75] Here, we seek to explore xylindein as an (opto)electronic material.

The core structure of the xylindein molecule is a peri-xanthenoxanthene (PXX),[41,76–79] derivatives of which (3,9-diphenyl-PXX and 3,9-bis(p-propylphenyl)-PXX) were shown to exhibit hole mobilities of up to ~0.8-0.9 $cm^2/(Vs)$[41,78] and unprecedented stability.[80] In particular, the reported OFETs remained considerably more stable over time with exposure to oxygen, moisture, light and heat as compared to similar pentacene-based devices.[41] PXX has also been used as a donor in charge transfer complexes for n-channel organic field effect transistors,[81] and its radical cation has been explored as a promising photo-oxidant.[82] Thus far, attempts at xylindein synthesis have proven incomplete.[83] The structure of xylindein was first reported in the 1960s[62,84] but its absolute configuration was unknown for many years, leading to a

systematic re-examination in 2000 to obtain the xylindein tautomeric structure.[63] The developments utilizing derivatives with the PXX core[41,78,80–82] and our promising preliminary results incorporating xylindein in electronic devices[43,56] motivated the present paper in which we investigate in detail optical and (opto)electronic properties of naturally-derived xylindein and xylindein-based films.

4.2 Materials and Methods

4.2.1 Extraction of Xylindein

Over the past 5 years, we have developed a variety of protocols for cultivating fungi and extracting fungi-produced pigments.[73,85,86] Here we focus on the wild type xylindein, sustainably obtained from the decaying wood (Figs. 4.1(a) and (b)), leaving a detailed comparison of characteristics of xylindein obtained via different preparation and purification protocols to a separate publication. Wild type xylindein was harvested from wood (Fig. 4.1(a)) collected at Tidewater, Oregon, USA. Appropriate wood was identified by the signature blue-green color produced by *Chlorociboria* species, which is unique across several kingdoms. The *Chlorociboria* species responsible for staining the wood was identified as *Chlorociboria aeruginosa* through DNA extraction and Sanger sequencing of the internal transcribed spacer region, followed by GenBank Megablast comparison (see Supporting information). The collected wood was crushed into approximately 2-3 mm fragments. The powder was placed in a 500 mL flask, with enough powder to cover the bottom of the flask in an even layer. 100 mL of dichloromethane (DCM) was poured into the flask. The contents were then stirred on a magnetic stir plate for one hour before being filtered as described in Ref. [59]. The solid crude xylindein was collected from evaporated DCM solution, then sonicated in ethanol to form a suspension of xylindein aggregates. The ethanol solution was passed through a 0.45 μm PTFE filter, followed by multiple passes of clean ethanol through the filter to remove contaminants. The xylindein was removed from the filter with DCM, and solvents evaporated to yield solid xylindein powder.

4.2.2 Mass Spectrometry

Analysis was performed on a Shimadzu HPLC (Columbia, MD) coupled to a Waters Synapt HDRMS time of flight mass spectrometer (Milford, MA). The MS was operated in positive ion mode, 80-1000 m/z scan range, 1 second scan time. A binary gradient and a 1.0 x 50 mm Waters XBridge C18 column (Milford, MA) were used, for analytical separation. Solvent A consisted of MS grade water (Fisher Scientific, Fairlawn, NJ) and 0.1% formic acid (EMD Millipore Corporation, Billerica, MA). Solvent B consisted of MS grade acetonitrile (Fisher Scientific, Fairlawn, NJ) and 0.1% formic acid. High-resolution mass spectrometry of xylindein resulted in measured mass of 569.1448 (M + H)+, corresponding to the (M + H)+ ion, C32H25O10 (calculated exact mass of 569.1448, mass accuracy of 0.00 ppm), which is in agreement with the literature.[62,63]

4.2.3 Sample Preparation

For measurements of optical properties, xylindein powder was dissolved in various solvents (Fig. 4.1(c)) including DCM, chloroform (CF), chlorobenzene (CB), tetrahydrofuran (THF), acetone (Ac), isopropyl alcohol (IPA), and water at various concentrations in the 10^{-6} M – 10^{-3} M range.

For preparation of films, three types of solutions were prepared: xylindein dissolved in DCM at 10 mg/mL concentration, a mixture of 4 mg xylindein with 1 mg poly(methyl methacrylate) (PMMA) (Aldrich, Mw=15000) dissolved in 500 μL DCM to form a 10 mg/mL solution, and a mixture of 4 mg xylindein with 1mg of crystalline nanocellulose (CNC) with 500 μL formic acid to form a 10 mg/mL solution. CNC powder with fiber dimensions 5-20 nm wide by 150-200 nm long was obtained from the Process Development Center at the University of Maine.

For film preparation, solutions of pristine xylindein or xylindein:PMMA or xylindein:CNC mixtures were drop cast onto glass substrates patterned with Al or Au/Cr coplanar or interdigitated electrodes spaced by 25-200 μm.[45] Structure and morphology of drop-cast films was assessed using SEM and XRD, revealing amorphous structure and morphology depending on the mixture, with blends yielding smoother films than pristine xylindein (Fig. 4.2). The film thickness measured using a surface profilometer ranged between 3 and 5 μm, depending on the device.

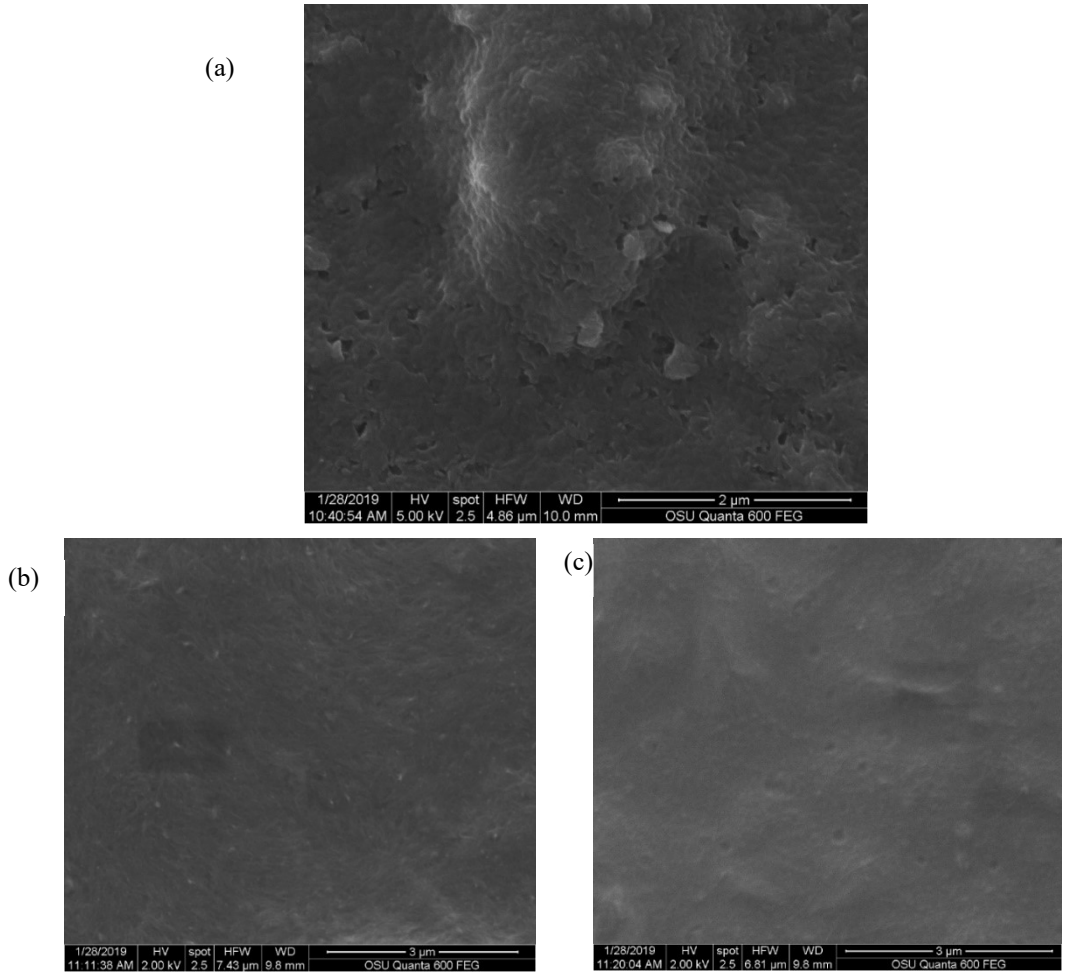

Figure 4.2. SEM images of a pristine xylindein film (a), xylindein:CNC (b), and xylindein:PMMA (c). Considerably smoother films are achieved in blends of xylindein with polymers as compared to pristine. Data taken by Ray Van Court (Robinson Lab, OSU Wood Science and Engineering).

4.2.4 Measurements

For optical absorption measurements in solution and film, light from a halogen (LS-1, Ocean Optics) or Xe lamp (Oriel 96000) transmitted through samples was measured using an Ocean Optics USB2000 spectrometer. For PL measurements, solutions samples were excited with 633 nm light (HeNe laser). As reference material for the PL quantum yield estimates, previously studied functionalized pentacene (Pn) derivative Pn-TIPS-F8 (also known as F8 TIPS-Pn) with QY = 0.6 in toluene was used.[87] PL emission was collected using an Ocean Optics USB2000-FLG spectrometer as described in our previous publications.[46,88] Measurements of optical absorption in films were conducted on an inverted microscope (Olympus IX-71) with a 10x objective.

For measurements of photostability, 10 μM solutions of xylindein in chlorobenzene and of benchmark organic semiconductors – functionalized fluorinated anthradithiophene (ADT) derivative diF TES-ADT and functionalized pentacene TIPS-Pn - in toluene were prepared,[46,87,89,90] and their optical absorption measured. The spectra were integrated in the S0-S1 absorption region (600-700 nm for xylindein, 450-550 nm for diF TES-ADT, and 560-660 nm for TIPS-Pn) yielding a data point at time t = 0. The solutions in vials sealed with a paraffin film to prevent solvent evaporation were then placed under the fume hood lights, in air, and the spectral measurement was repeated at various time intervals. The S_0-S_1 spectra were integrated and the result normalized by that at t = 0. The experiment was carried out up to 30 weeks.

For measurements of thermal stability, pristine xylindein films were placed on a hot plate held at a particular temperature in the 50 – 200 °C range for two hours, in air. The absorption spectrum of the film was measured every 5 minutes. The spectra were integrated in the S_0-S_1 absorption region (600-750 nm) and plotted as a function of time, normalized at the value at t = 0.

For measurements of current-voltage characteristics, voltage was applied to the samples using a Keithley 237 source-measure unit and current in the dark was measured as a function of applied voltage ranging from 0-300 V.

Continuous wave (cw) photocurrents in films were measured under 633 nm 2 mW/cm^2 photoexcitation chopped using an optical chopper at 100 Hz. Voltage was applied to the samples using a Keithley 237 source-measure unit, and the photocurrent was measured using a Stanford Research Systems (SRS830) lock-in amplifier.

For temperature-dependent measurements, samples were incorporated in an optical cryostat (Janis STC-500), and dark current and photocurrent measurements were carried out in vacuum in the temperature range of 300-350 K.

4.2.5 Density Functional Theory (DFT) Calculations

The structure of xylindein was optimized using DFT methods in Gaussian 16 to ascertain the location and orientation of xylindein's hydroxyl groups. Initial structures of the molecule were optimized with the B3LYP function and 6-31G(d,p) basis set. Only configurations with centralized hydroxyl groups (Fig. 4.1(d)) were found to be energetically stable, and of those only two were found to have negligible dipole moments (Fig. 4.3), in keeping with our observations of enhanced solubility of xylindein in nonpolar, as compared to polar, solvents (discussed below). These two tautomers A and B were then optimized with a larger basis set (6-311G++(d,p)) to find the energies of the Highest Occupied Molecular Orbital (HOMO) and Lowest Unoccupied Molecular Orbital (LUMO). Time-dependent DFT (TD-DFT) methods were applied to find the energies of the vertical first allowed singlet excited state for the xylindein embedded in the DCM solvent environment. A similar optimization process was conducted for dimethylxylindein derivative, yielding only a single configuration. Properties of dimethylxylindein, embedded in a DCM solvent environment, were also calculated in order to assess the contribution of the OH groups, not present in dimethylxylindein, to various characteristics of xylindein. Control calculations were also conducted on several derivatives of peri-xanthenoxanthene (PXX) for comparisons with the literature.

(a) (b)

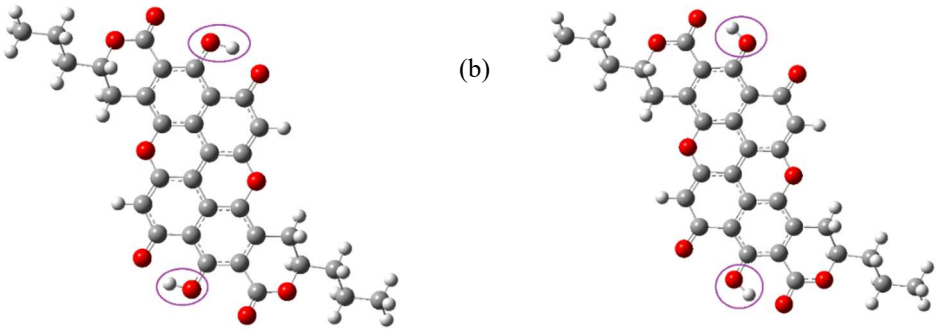

Figure 4.3. Molecular structures for xylindein tautomers A (a) and B (b) with optical properties described in Table 1. The difference in the orientations of the OH groups between the two tautomers is emphasized by encircling.

4.2.6 Fit Procedure

The dilute solution absorption spectra of xylindein were initially fit using a vibronic progression model of Eq. (4.1):[35,91–93]

$$\frac{A}{\hbar\omega} = A_0 \sum_{n=0}^{5} \frac{e^{-S} S^n}{n!} \Gamma_{\sigma_0(1+n\Delta\sigma)}(\hbar\omega - E_X - nE_V) \tag{4.1}$$

Here $A/\hbar\omega$ represents the reduced absorption as a function of photon energy and A_0 is a scale factor for the integrated absorption of the exciton manifold. E_X is the 0-0 energy, E_V is the vibrational energy, n is an index for the number of vibrational quanta hosted by the molecule, and S is the corresponding Huang-Rhys factor. Each optical transition is modelled with a Lorentzian lineshape Γ, with a FWHM of $\sigma_0(1+n\Delta\sigma)$. Here σ_0 is the 0-0 broadening, and $\Delta\sigma$ is the dimensionless progressive broadening factor which corrects for vibrational modes not explicitly treated in the model.[92]

It was found that a single vibronic progression of Eq.(4.1) was insufficient to model the fine details in the xylindein spectra, so the spectra were then fit assuming the convolution of two vibronic progressions: $A_1/\hbar\omega + A_2/\hbar\omega$ (Fig. 4.4(c)), each characterized by their own parameters E_X, E_V, S, σ_0, and $\Delta\sigma$ (Table 4.1).

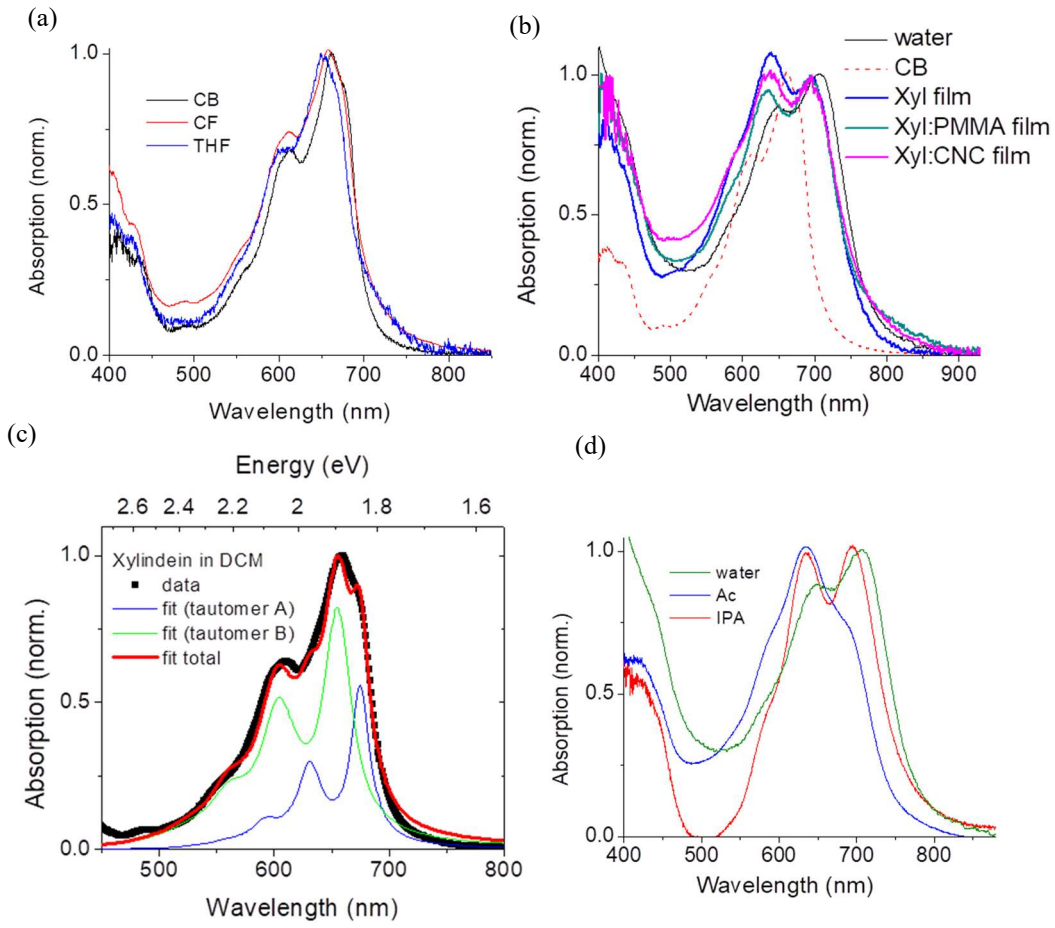

Figure 4.4. (a) Spectra of dilute solutions of xylindein in chlorobenzene (CB), chloroform (CF), and tetrahydrofuran (THF). (b) Spectra of xylindein in CB and water solutions, in pristine film, and in blends with PMMA and CNC. (c) Absorption spectrum in DCM divided by ħω and fit using two vibronic progressions, each described by Eq.(4.1). The fit parameters are listed in Table 4.1. The sum of the contributions of the two tautomers to the spectra is also included. (d) Absorption spectra of xylindein in water, acetone (Ac), and isopropyl alcohol (IPA) showing pronounced aggregation resulting in formation of the band peaked at 710-720 nm.

4.3 Results and Discussion

4.3.1 Optical Properties

Optical absorption spectra of xylindein solutions in solvents of various polarity are shown in Fig. 4.4. The most pronounced effect of solvent polarity on xylindein spectra was in the solvent polarity dependent propensity of xylindein for aggregation. At comparable concentrations, the contribution of xylindein aggregates to the spectra, which lead to the appearance of a new absorption band peaked at about ~710-720 nm, was considerably higher as the solvent polarity increased. For example, in THF (dielectric constant $\varepsilon = 7.9$), the aggregate peak was pronounced at already 40 μM, while it was not present at 60 μM in CB ($\varepsilon = 5.6$). For highly polar solvents such as isopropyl alcohol ($\varepsilon = 20$), acetone ($\varepsilon = 21$), and water ($\varepsilon = 80$), even at micromolar concentrations the aggregate peak was strongly pronounced (Figs. 4.4(b) and (d)). This is consistent with xylindein being a nonpolar molecule, and so its solubility in polar solvents is greatly reduced. The aggregates were also responsible for the near-infrared absorption spectra of xylindein-based films (Fig. 4.4(b)) showing absorption features similar to those for xylindein in water.

In order to better understand the absorption spectra of xylindein, we fit the spectra as described in Materials and Methods. The parameters obtained from fits to the spectra of dilute solutions in CB and DCM are summarized in Table 4.1. The spectra of dilute solutions in these solvents exhibit a similar structure that can be fit by a sum of two vibronic progressions, each described by Eq. (4.1) (Fig. 4.4(c)). In order to understand the origin of the complicated structure of the S_0-S_1 spectrum of xylindein, we also modelled the absorption spectrum of the dimethylxylindein, in which the OH groups are substituted by the OMe groups (Fig. 4.5(b)). The absorption spectrum of dimethylxylindein in DCM produced a good fit with one vibronic progression of Eq. (4.1) as shown in Fig. 4.5(a). Therefore, we attribute the need for two vibronic progressions to adequately describe the S0-S1 spectrum of xylindein to the presence of two tautomers which exhibit slightly different energies for the 0-0 transition (Ex) and parameters describing the line shape and vibronic coupling in Eq. (4.1). Molecular structures of such tautomers were identified using DFT calculations as described in Materials and Methods and are shown in Fig. 4.3 with the relative contributions of tautomers A and B to the absorption spectra of about 30:70 (A_0 in Table 4.1). Their calculated vertical energies, which are comparable to the 0-0

energies (E_X) extracted from fits to the experimental data, are also included in Table 4.1.

Table 4.1. Fit parameters obtained from fits of the absorption spectra to a vibronic progression of Eq. (4.1). In the case of xylindein, a sum of two vibronic progressions, with the corresponding parameters listed, were needed to obtain a good fit. Numbers in the brackets correspond to values of vertical energies for two xylindein tautomers calculated as described in Materials and Methods.

Fit parameters	Xylindein in CB ($\varepsilon = 5.6$)	Xylindein in DCM ($\varepsilon = 8.9$)	Dimethylxylindein in DCM
A_0 (norm.)	0.35; 0.65	0.3; 0.7	1
E_X (eV)	1.82; 1.88	1.84; 1.90 [1.89; 1.93]	2.17 [2.14]
E_V (eV)	0.13; 0.16	0.13; 0.16	0.18
S	0.87; 0.87	0.77; 0.92	0.99
σ (eV)	0.07; 0.09	0.06; 0.08	0.11
$\Delta\sigma$	0.51; 0.51	0.55; 0.59	0.53

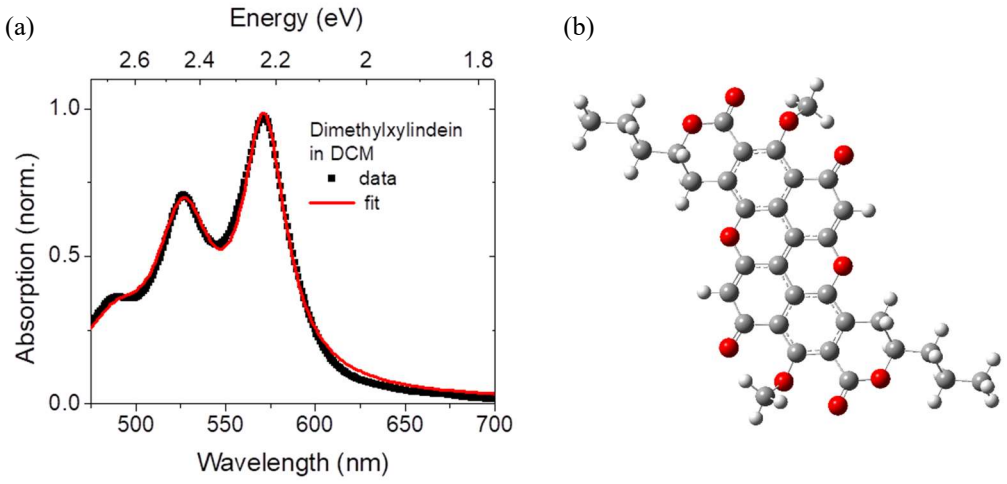

Figure 4.5. (a) Normalized absorbance divided by $\hbar\omega$ of dimethylxylindein in DCM fit with a vibronic progression of Eq. (4.1). Fit parameters are listed in Table 4.1. Molecular structure of dimethylxylindein is shown in (b).

In all xylindein solutions, the PL quantum yields measured at 633 nm excitation of the S_0-S_1 transition were below 0.1%. Such low quantum yields have been observed in other pigments such as indigo, for which it was attributed to the intramolecular

proton transfer.[54,94] The mechanism of nonradiative energy relaxation in xylindein is currently under investigation and will be reported in our subsequent publication.

4.3.2 Stability

Figure 4.6 illustrates considerably higher photostability of xylindein in solution as compared to solutions of benchmark organic semiconductors TIPS-Pn and diF TES-ADT.[46,88] In particular, under continuous illumination in air, the TIPS-Pn molecules in solution decomposed within 3 days. The fluorinated ADT derivative, diF TES-ADT, which has been photostable enough to enable its use as a fluorophore in single-molecule fluorescence spectroscopy,[87] showed a gradual degradation over the period of first several weeks followed by an accelerated degradation starting at about 5 weeks. Under the same conditions, no degradation in optical absorption of xylindein was observed over the period of about 25 weeks, after which some degradation occurred (Fig. 4.6).

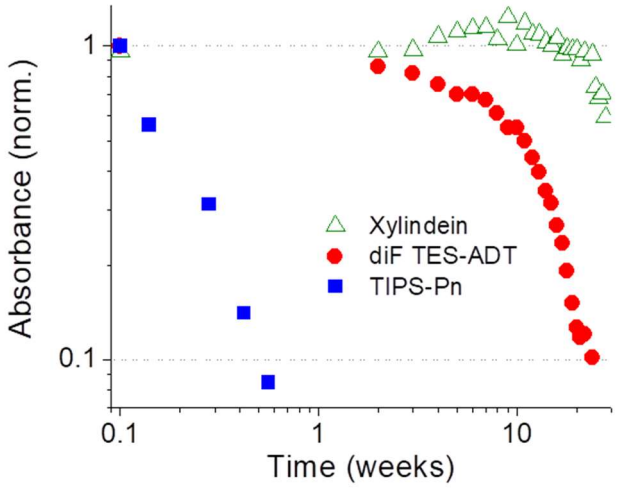

Figure 4.6. Integrated S_0-S_1 spectra, normalized at time t = 0, of dilute solutions of xylindein and of benchmark organic semiconductors TIPS-Pn and diF TES-ADT continuously exposed to light and air.

Enhanced photostability of pigments has been their known property for a long time, fostering their applications in art throughout the history[95,96] and more recently, as

food colorants, paints,[97] and, finally, organic electronic devices.[52,67,69,98] The origin of high photostability depends on the molecular structure. For example, photostability of indigo and its derivatives has been attributed to sub-picosecond excited intramolecular proton transfer leading to a rapid internal conversion.[54,94] This leads to short excited state lifetimes, low PL quantum yields, and high photostability. Similar considerations could be operational in xylindein; ultrafast spectroscopy necessary to quantify the picosecond time-scale excited state dynamics and reveal the contributing mechanisms is underway and results will be reported elsewhere.

Xylindein also exhibited a relatively good thermal stability in air. For example, no considerable degradation of optical properties of xylindein films was observed upon holding the xylindein film at temperatures up to 100 °C in air for at least two hours (Fig. 4.7). About 8% and 15% degradation occurred at 150 °C and 175 °C, respectively, after two hours. At 200 °C, pronounced degradation occurred within the first 20 minutes of the heat treatment.

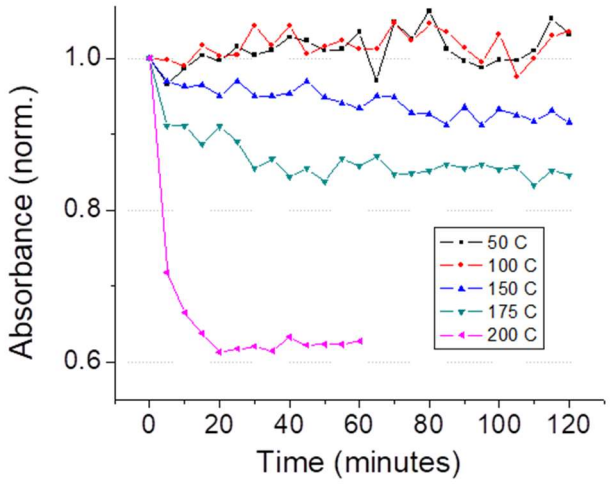

Figure 4.7. Integrated S_0-S_1 absorbance, normalized at its value at t = 0, for pristine xylindein films kept at the temperature indicated, in air and under illumination. No degradation was observed up to temperatures of 100 °C over continuous heat exposure for 2 hours in air. About 8% and 15% degradation occurred at 150 °C and 175 °C, respectively, after 2 hours. Considerably faster degradation occurred at 200 °C. Data taken by Alex Quinn.

4.3.3 (Opto)electronic Properties

In order to better understand electronic properties of xylindein, we performed DFT calculations of the HOMO and LUMO orbitals for the tautomers A and B (Figs. 4.3 (a) and (b), respectively) revealed by the combination of optical spectroscopy and DFT calculations. The HOMO and LUMO energies yielded -6.49 (-6.30) eV and -4.31 (-3.99 eV), respectively, for the tautomer A (B), resulting in the HOMO-LUMO gap of 2.19 (2.31) eV, as shown in Fig. 4.8. The low LUMO energies of xylindein suggest preferential electron or ambipolar transport, in contrast to the unsubstituted PXX which favors hole transport.[77] Results from the cyclic voltammetry are consistent with this prediction, and the reversible reduction in xylindein was confirmed experimentally.

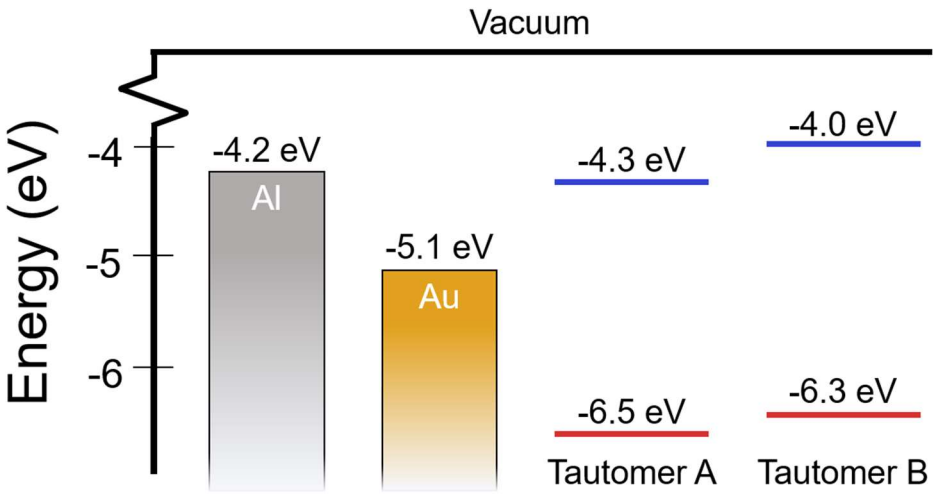

Figure 4.8. HOMO and LUMO energy levels for two xylindein tautomers. Work functions of Al and Au relative to the HOMO and LUMO energies are also shown.

In order to explore electron transport in xylindein films, we prepared films on aluminum (Al) electrodes in order to facilitate electron injection expected from a relatively good alignment of Al work function with LUMO energies of xylindein (Fig. 4.8). Figure 4.9 shows current-voltage (I-V) characteristics for two pristine xylindein films and for a xylindein:PMMA film, all on coplanar Al electrodes. Ohmic

response followed by a characteristic transition from the linear ($I \sim V$) to the space-charge-limited current (SCLC) ($I \sim V^2$) regime was observed in all samples. In the case of the planar electrode geometry used in our experiments, the current flows along a thin layer of unknown thickness, and the current density (j) is expressed in units of A/m (as opposed to A/m^2 for the "sandwich" electrode geometry). Although there is no analytical solution for the relationship between the SCLC linear current density (j) and the applied voltage (V) in a film of finite thickness on coplanar electrodes, there are solutions for the extreme cases of the infinitely thin film ("thin-film approximation") and the infinite half space.[45] In the thin-film approximation, the linear current density[45] $j = (2/\pi)\, \mu_{eff}\, \varepsilon\, \varepsilon_0\, V^2/L^2$. Here $j = I/d$, where I is the measured current and d is the length of the electrode, L is the gap between the electrodes, ε_0 is the vacuum permittivity, ε is the dielectric constant (assumed here to be equal to 3), and μ_{eff} is the effective mobility. The thin-film approximation for these devices is justified by the ≤ 5 μm film thicknesses as compared to the gap between the electrodes (L) of 50-200 μm chosen for these experiments. From SCLC currents (inset of Fig. 4.9), the values for the effective mobility in the 0.1-0.4 $cm^2/(Vs)$ range were obtained, depending on the device, in pristine xylindein films. We consider these values to be lower bound estimates to the electron mobility, as the trap-free SCLC regime was not reached in our measurements and thus, the intrinsic mobility is higher. We also note that the performance of xylindein-based devices depends on the fungi growth and purification protocols,[99] and higher mobilities could be possible with protocols other than the one used in the present study; this is currently under investigation. Achieving effective mobility values above 0.1 $cm^2/(Vs)$ is rather remarkable given that the films under study are amorphous, illustrating benefits of an interplay of intermolecular hydrogen bonding and π-π stacking, afforded by the molecular structure of xylindein, for charge transport.

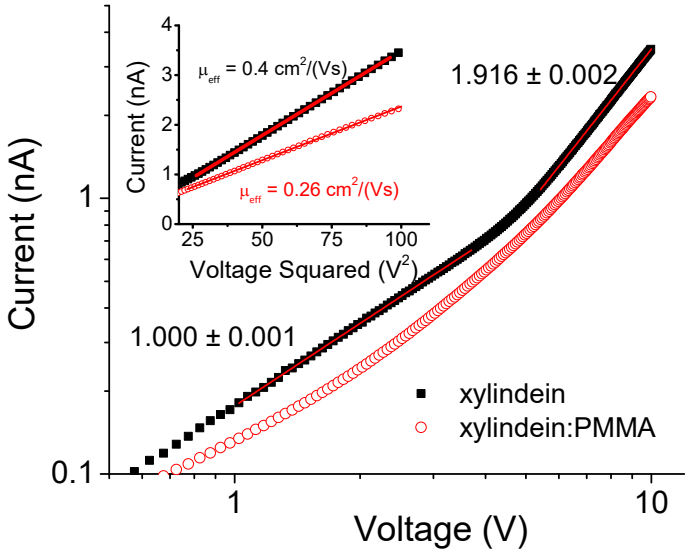

Figure 4.9. Current-voltage (I-V) characteristics for pristine xylindein and xylindein:PMMA films on coplanar Al electrodes with a 200 μm gap, showing transition from the linear to the quadratic (SCLC) regime. Inset shows I vs V^2 and linear fits slopes of which were used to calculate the effective mobilities assuming the thin-film approximation of the SCLCs in the planar electrode geometry as discussed in the text.

As xylindein tends to form porous and inhomogeneous films[56] (Fig. 4.2(a)), in order to improve film processability we also explored its blends with a polymer PMMA and a biopolymer CNC (both of which exhibited negligible electric currents in the absence of xylindein, thus providing a non-conductive scaffold for the xylindein molecules). The use of PMMA was inspired by our own[44] and other literature[100,101] studies of electronic properties of small-organic-semiconductor molecule:non-conductive polymer blends, which exhibited improved morphology and comparable or better electronic performance than that of pristine organic semiconductor films. The naturally sourced CNC was chosen in order to explore the possibility of creating the all-sustainable functional xylindein:polymer blend. Both blends yielded considerably smoother films (Fig. 4.2(b) and (c)) as compared to xylindein films, with optical properties similar to those of pristine xylindein film (Fig. 4.4(b)), which suggests that the nature of xylindein aggregates is similar in all films. The xylindein:PMMA films yielded electric characteristics similar to those of the pristine

xylindein films (Figs. 4.9 and 4.10), with the SCLC effective mobilities similar to those in pristine xylindein film (e.g. 0.26 cm2/(Vs) in the xylindein:PMMA film in Fig. 4.9). The xylindein:CNC films exhibited electric currents and corresponding SCLC effective mobilities that were more than an order of magnitude lower than those in pristine xylindein or xylindein:PMMA blends, most likely due to a non-uniform distribution of xylindein in the CNC at high concentrations, which prevents formation of efficient conductive network via xylindein molecules.

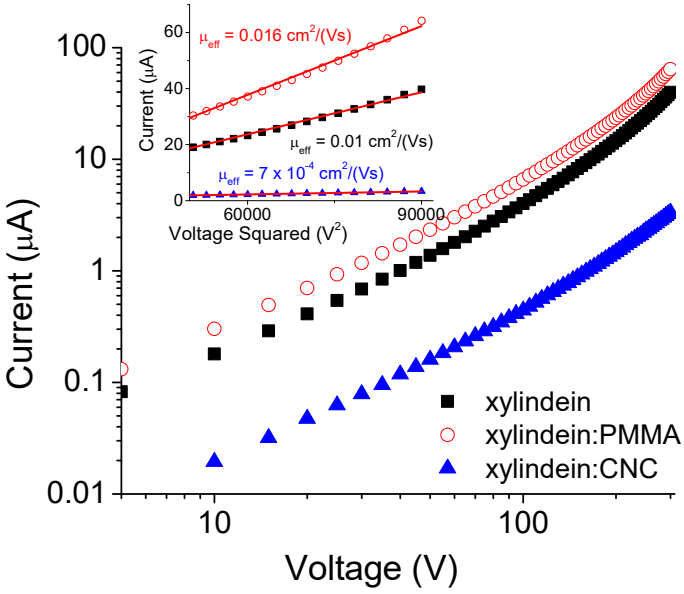

Figure 4.10. Current-voltage characteristics for a pristine xylindein, xylindein:PMMA, and xylindein:CNC films on interdigitated Au electrodes with a 25 μm gap. Inset shows the high-voltage data for these three films replotted as a function of V^2, with linear fits that were used to calculate effective mobilities in the thin-film approximation of the SCLC in the planar electrode geometry as discussed in the text.

In planar devices using gold (Au) electrodes, the transition from the linear to the quadratic SCLC regime was also observed in the current-voltage characteristics; however, it occurred at considerably higher voltages as compared to those in devices with Al electrodes, reflecting differences in the charge carrier injection properties depending on the electrode material. From the I vs V^2 linear fits to the SCLC regime

in devices on planar Au electrodes (inset of Fig. 4.10), in the thin-film approximation one obtains the effective mobilities μ_{eff} of ~0.01 $cm^2/(Vs)$, 0.016 $cm^2/(Vs)$, and 7 x 10^{-4} $cm^2/(Vs)$ in pristine xylindein, xylindein:PMMA, and xylindein:CNC films, respectively. If the hole injection is dominant in these devices, the μ_{eff} values represent a lower bound on the hole mobility in these systems, as the trap-free regime was not achieved in these devices.[102] However, based on the alignment of the Au work function with the energy levels of xylindein (Fig. 4.8) it is not clear whether the injection of a single type of the carrier can be ensured, in which case interpretation of the effective charge carrier mobility is considerably less straightforward[103] and it relies on the knowledge of recombination mobility, which is not known for our materials.

In order to probe the mechanism of conduction in xylindein-based films, we performed temperature dependent measurements of electric currents in the dark and under a 633 nm cw photoexcitation. All samples exhibited a thermally activated response (~exp[$-E_a/k_BT$], where E_a is the activation energy, k_B is the Boltzmann constant, and T is the temperature) characterized by the activation energies E_a of 0.31 eV, 0.25, and 0.24 eV for the dark currents in pristine xylindein, xylindein:PMMA, and xylindein:CNC films, respectively (Fig. 4.11(a)). Such temperature dependence is, for example, characteristic of a hopping charge transport mechanism in the exponentially distributed manifold of trap states with a characteristic energy E_a.[3] The obtained values of E_a are similar to those in a variety of amorphous polymers (e.g. E_a = 0.33 eV and 0.37 eV in polyfluorene-based derivatives PFB and F8BT, respectively) and organic glasses.[104–108] Reduction in the activation energy in blends as compared to pristine xylindein films is consistent with a more uniform morphology achieved in blends although one could argue that larger differences in the activation energies would be expected from the three types of samples with different morphology used in our studies. It has been demonstrated that the activation energy in charge carrier mobility measurements may have contributions from charge traps both from the bulk organic semiconductor material and from the interface with a substrate (formed by strain due to the mismatch in the thermal expansion coefficients between the organic semiconductor and the substrate). For example, the latter accounted for up

to ~0.1 eV differences in the activation energy observed in mobilities of P3HT transistors depending on the gate dielectric.[109] If the charge traps at the interface were responsible for most of the E_a in our samples, this would suggest that at the film-substrate interface there is a thin xylindein layer with only slightly different morphology in all three types of samples used in our studies. It is also interesting to note that the values of E_a are similar to the differences in the LUMO energy levels for the two xylindein tautomers and so the presence of the two tautomers with offset energies, rather than specific morphology of the films or of the interfacial layer, could dominates the disorder contributing to charge transport.

All three types of xylindein-based films also exhibited photoresponse to a 633 nm continuous wave (cw) excitation.[43,56] The temperature dependence of the photocurrents revealed slightly lower activation energies as compared to dark currents (0.2 eV in pristine xylindein and 0.18 eV in xylindein-based blends), as shown in Fig. 4.11(b). These values are comparable to those obtained from photocurrents in various amorphous organic materials,[110–112] and the lower activation energies as compared to dark current activation energies have also been observed in organic glasses,[111] reflecting a slightly narrower energy manifold sampled by the photoexcited charge carriers as compared to injected carriers.

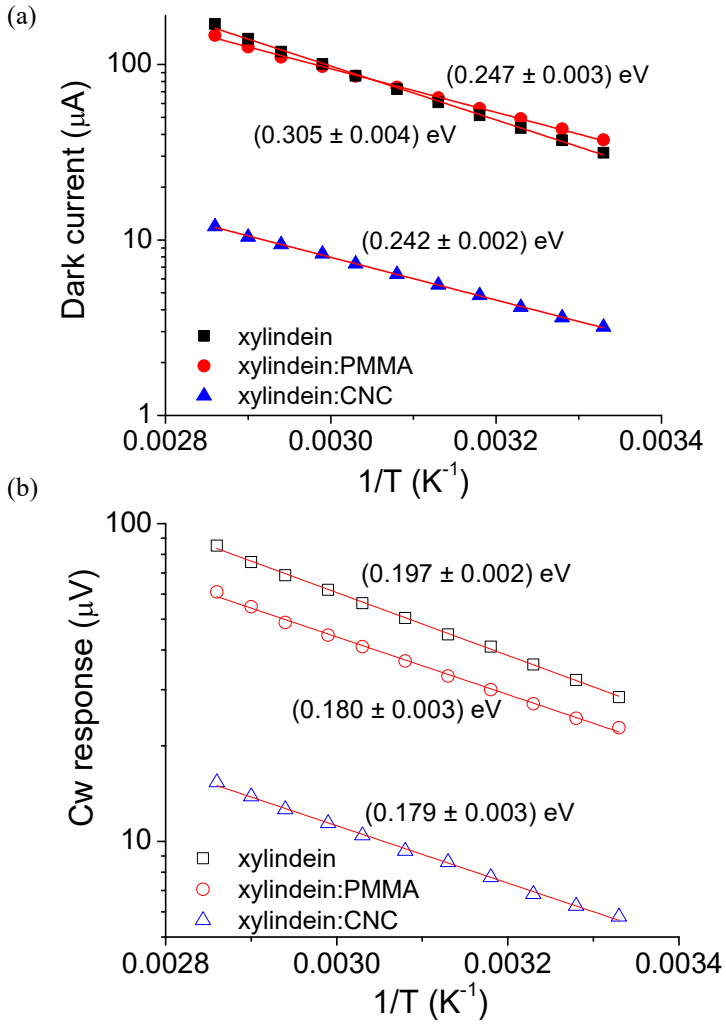

Figure 4.11. Temperature dependence of dark (a) and photo (b) currents obtained in pristine xylindein, xylindein:PMMA, and xylindein:CNC films on interdigitated Au electrodes with a 25 μm gap at 100 V. Arrhenius fits (~exp[-E_a/k_BT]) with the extracted activation energies E_a are also included. The temperature dependence was independent of the applied voltage in the range studied.

4.4 Conclusions

Optical and (opto)electronic properties of a naturally derived pigment xylindein and its blends with PMMA and CNC are presented. Analysis of the optical spectra revealed the presence of two tautomers whose structures and properties were explored using DFT. Propensity for xylindein aggregation depended on the solvent polarity and

was strongly pronounced in polar solvents. Aggregates with similar optical properties were observed in films. Excellent photostability was observed in xylindein solutions as compared to those of benchmark organic semiconductor molecules. Electron mobility of up to 0.4 cm^2/Vs was obtained in amorphous films. Both dark and photocurrent were thermally activated with activation energies of 0.3 and 0.2 eV, respectively, in pristine xylindein films. Xylindein blends with PMMA exhibited (opto)electronic performance comparable to that of pristine xylindein films. In xylindein blends with CNC, both dark and photocurrents were at least an order of magnitude lower than in pristine xylindein films. In both blends, the charge transport activation energies were lower (0.25 eV) than in pristine xylindein films due to a smoother film morphology as revealed by the SEM.

Chapter 5: The role of hydroxyl groups in the photophysics, photostability, and (opto)electronic properties of the fungi-derived pigment xylindein

Authors:

G. Giesbers, T. Krueger, J. Van Schenck, R. Kim, R. Van Court, S. Robinson, C. Beaudry, C. Fang, O. Ostroverkhova

The Journal of Physical Chemistry C (2021)

Journal Online Access

125 (12), 6534-6545

5.1 Introduction

Organic (opto)electronic materials have attracted considerable attention due to their low cost, enhanced processability, and tunable properties.[35] A variety of applications, including organic solar cells, light-emitting diodes, thin-film transistors (TFTs), sensors, and many others have been demonstrated.[23] One of the major issues for the wide-spread applications of organic materials is their relatively low stability with respect to exposure to environmental factors.[23] This issue drives a search for stable organic electronic materials and provides the motivation to understand how stability depends on the molecular structure and packing. In "conventional" organic semiconductors such as acene or thiophene derivatives, examples of molecular design strategies that resulted in enhanced stability of molecules in air include fluorination of the molecular core (e.g., in the case of fluorinated functionalized pentacene (Pn), hexacene, or anthradithiophene (ADT) derivatives as compared to their non-fluorinated counterparts[87,113,114]) and increasing the dimensionality of the molecule (e.g., in the case of bistetracene as compared to tetracene[115]). Additionally, over the past decade, hydrogen (H)-bonded pigments with "unconventional" molecular structures (exemplified by indigo, epindolidione, or quinacridone)[33,53,116] have been explored as organic (opto)electronic materials. These pigments exhibited enhanced photo and/or thermal stability in air, combined with relatively strong (opto)electronic performance,[33,53,116,117] both of which were partially attributable to the effects of intra- and intermolecula[36,72]r H-bonding. More generally, H-bonded organic materials are of interest for organic electronics[33,53,116,117] due to the potential to exploit H-bonds in inducing long-range molecular order,[53,117] which promotes charge carrier delocalization that could lead to enhanced electronic properties.

We recently reported on the optical and electronic properties of a highly stable pigment xylindein (Fig.5.1(a)), which is secreted by wood-staining fungi in the *Chlorociboria* genus.[56,57,99] Xylindein belongs to a special class of external pigments produced by wood-decaying spalting fungi to defend the territory as they slowly grow and deeply penetrate into wood.[72] Because it can take years for the spalting fungi to fully colonize a log, the pigment they make must persist and not degrade in air under

UV light, heat, and other environmental conditions. Xylindein has been used in art and intarsia since the 15th century, and its impressive color retention in these works of art in the present time is a testament to xylindein's environmental stability.[36,72] In terms of photostability in the presence of continuous illumination in air, xylindein considerably outperformed benchmark organic semiconductors TIPS-Pn and a relatively stable fluorinated ADT derivative diF TES-ADT.[57] The enhanced stability was accompanied by electron mobility of up to 0.4 cm2/(Vs) in amorphous xylindein films.[57] However, how the enhanced stability and a relatively strong electronic performance of xylindein are determined by various aspects of its molecular structure, for example its peri-xanthenoxanthene (PXX) molecular core versus the presence of the hydroxyl (OH) groups (Fig. 5.1(a)) and H-bonding they enable, has not been established and is explored in the present paper.

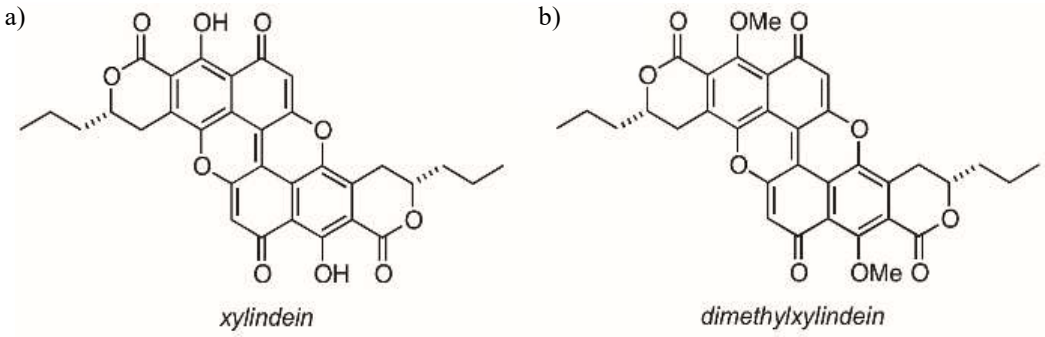

Figure 5.1. Molecular structure of xylindein (a) and dimethylxylindein (b).

The photophysical and (opto)electronic properties of molecules with the PXX core have been considerably less studied than those of benchmark organic semiconductors such as acene derivatives. For instance, photophysics of PXX and a small subset of its derivatives was characterized in detail only in the past three years.[82,118,119] The unsubstituted PXX exhibits optical absorption (fluorescence) maximum at ~440 nm (450 nm), fluorescence quantum yields (QYs) of 0.5–0.97 depending on the solvent, and solvent-dependent lifetimes of ~5–8 ns.[118] The functionalized PXX derivatives exhibited enhanced stability in air as compared to their parent carbon-based compound anthanthrene (which was attributed to the reaction-active site passivation

due to heteroatoms/substituents on the molecular core) and compared to Pn; the enhanced stability was accompanied by TFT hole mobilities of up to 0.8 $cm^2/(Vs)$.[41] Because the unsubstituted PXX produced poor film morphology, several PXX derivatives featuring various solid-state packing motifs were synthesized and characterized in TFTs, exhibiting hole mobilities in the 0.04–0.9 $cm^2/(Vs)$ range.[41,79] Although predicted theoretically,[77] n-type behavior has not been experimentally observed in functionalized PXX derivatives.

The photophysical and electronic properties of xylindein are distinctly different from those of unsubstituted PXX and its derivatives studied in the literature.[41,79,82,118,119] For example, xylindein is non-fluorescent (QY < 0.1%), and it favors electron (n-type) transport. Therefore, in order to better understand properties of xylindein and relate them to the specifics of its molecular structure, we sought a molecule with a structure closer to that of xylindein as compared to PXX. In particular, we synthesized a methylated derivative of xylindein (dimethylxylindein, Fig. 5.1(b)), which has most of the features of xylindein's molecular structure (Figs. 5.1(a)) except for the OH groups that are substituted with OCH^3 (OMe) groups. We performed a side-by-side comparison of optical and (opto)electronic properties of these two compounds, revealing dramatic differences in their photophysics and (photo)conductivity. In particular, we demonstrated that the processes enabled by the OH groups in xylindein are critical for its remarkable photostability and enhanced electronic properties.

5.2 Materials and Methods

5.2.1 Extraction of Xylindein

Xylindein was extracted in accordance with procedures detailed in our previous publications from both wild and lab grown sources.[56,57,99] Briefly, wild type xylindein was harvested from wood collected at Tidewater, Oregon, USA. The wood was identified from the characteristic blue-green color unique to *Chlorociboria* species. DNA extraction followed by Sanger sequencing of the internal transcribed spacer

region and GenBank Megablast comparison identified the species responsible for staining the wood as *Chlorociboria aeruginosa*.[57] Lab grown xylindein was produced by *C. aeruginosa* (strain UAMH 11657) cultures maintained on 2% malt agar plates. These cultures were used to inoculate multiple 250 mL borosilicate mason jars each containing 50 mL of sterile 2% malt agar liquid media, which were then shaken at 99 rpm (Orbital GeneTM Scientific Industries) during growth. Mature colonies were collected and xylindein was extracted with a liquid-liquid dichloromethane (DCM)-water extraction, after blending to break apart cell walls with an Oster classic series blender. Extracted xylindein was then evaporated from DCM solution and rinsed multiple times with ethanol to remove contaminants.[99]

5.2.2 Synthesis of Dimethylxylindein

Dimethylxylindein was prepared by diazomethane-mediated methylation of xylindein following the method of Hashimoto.[63] The synthesis was performed by Ryan Kim (Beaudry lab, OSU Chemistry).

5.2.3 Sample Preparation

For optical measurements, xylindein or dimethylxylindein powder was dissolved into DCM or toluene at various concentrations ranging from 10^{-5} M – 10^{-2} M.
Xylindein films were cast from solutions in either DCM or CB at a concentration of 5 mg/ml. Pristine polycrystalline films of dimethylxylindein were cast from a 20 mg/ml solution in DCM. To create more homogeneous films and inhibit crystal formation, dimethylxylindein was mixed with PMMA (Aldrich Mw=75,000) at a 4:1 weight ratio, and dissolved in DCM at an overall concentration of 20 mg/ml.
Films were prepared by drop-casting onto glass substrates, with patterned, treated Au electrodes for electrical measurements. Electrodes were patterned using conventional lift off photolithography, with thermally evaporated Au (80 nm) with a 10 nm Cr adhesion layer. Au electrodes were treated with polyethylenimine, ethoxylated (PEIE) to form a ~10 nm interlayer for work function reduction according to the procedures

of Zhou et al.[120] Both coplanar and interdigitated electrode geometries, described in our previous publications,[46,88] were used.
For measurements of electronic properties in the sandwich geometry, xylindein:PMMA and dimethylxylindein:PMMA films at 1:1 and 1:2 weight ratios were prepared on Al (200 nm)/glass substrates followed by thermal deposition of another 200-nm Al layer patterned with a shadow mask.

5.2.4 Measurements of Optical Properties

Optical absorption spectra were measured using a tungsten-halogen lamp (LS-1, Ocean Optics) and a fiber-coupled Ocean Optics USB2000 spectrometer. Absorbance (A) was calculated from the incident (I_0) and transmitted (I) beam intensities as $A=-\log(I/I_0)$. Reflection losses were taken into account by referencing with respect to a cuvette with pure DCM. PL spectra were obtained using a cw 532 nm laser (Nd:YVO4 from Coherent, Inc.) or a 633 nm He-Ne laser. For solution PL, light was collected using a parabolic mirror and detected with a fiber-coupled spectrometer (Ocean Optics USB2000-FLG). Film absorption and PL were measured on an inverted microscope (Olympus IX-71) with a 10× objective, fiber-coupled to a spectrometer. As a reference material for the PL quantum yield estimates of dimethylxylindein and xylindein, previously studied functionalized pentacene (Pn) derivative TES-Pn with QY = 0.75 in toluene,4,24 was used.
Fluorescence lifetime measurements were performed using a 532 nm frequency-doubled Nd:YAG laser (HE-1060, Fianium, Inc.) with a repetition rate of 0.5 MHz as the excitation source. A single-photon avalanche photodiode (SPAD, Molecular Photonic Devices) was used in conjunction with a time-correlated single-photon counter (TCSPC) data analysis board (PicoQuant TimeHarp 200) for detection.

5.2.5 Femtosecond Transient Absorption (fs-TA) Spectroscopy

The experimental set up for fs-TA spectroscopy has been described in detail previously.[121,122] In brief, we used a Ti:sapphire regenerative laser amplifier (Legend

Elite-USP-1K-HE, Coherent, Inc.) with fundamental output laser pulses at ~800 nm center wavelength, ~35 fs pulse duration, ~3.7 W average power, and 1 kHz repetition rate. Second harmonic generation of a fraction of the 800 nm fundamental pulse in a 0.3-mm-thick Type-I BBO crystal produced the 400 nm actinic pump in the fs-TA experiments of xylindein and dimethylxylindein. In both experiments, the pump power was attenuated to ~0.2 mW. To achieve a longer detection time window that extends to ~4 ns, a quadruple-pass setup (with two UBBR2.5-2S broadband hollow retroreflectors, Newport, Inc.) was installed to effectively quadruple the delay line distance (NRT150, Thorlabs, Inc.) and the time delay controllable between the pump and probe interactions with the sample. Regarding the probe pulse, a portion of the laser fundamental output was focused onto a 2-mm-thick quartz cuvette filled with deionized water to generate supercontinuum white light (SCWL) without further temporal compression, so the probe pulse duration was on the ~150 fs range.[123,124] The transmitted probe beam (with a small crossing angle with the pump beam that was blocked past the sample) was dispersed in a spectrograph (Acton SpectraPro SP-2356, 300 mm focal length, Princeton Instruments) with a 300 grooves/mm, 500 nm blaze wavelength reflective grating before being imaged onto a front-illuminated Lumogen UV-coated CCD array camera (PIXIS:100F, Princeton Instruments), which was synchronized with the main laser repetition clock. Spectral data were processed and stored by a customized LabVIEW suite before further analysis using the IGOR Pro 6.2 software (WaveMetrics, Inc.). Sample concentration for fs-TA experiments on xylindein and dimethylxylindein was made to reach the absorbance OD≈0.3 per mm at 400 nm. The steady-state UV/Visible spectra were taken before and after each time-resolved fs-TA experiment to check and ensure sample integrity under light irradiation conditions used in our studies at room temperature.

5.2.6 Measurements of Photostability

For measurements of photostability, 10 μM solutions of xylindein and dimethylxylindein were prepared, and their optical absorption measured. The spectra were integrated in the S_0-S_1 absorption region (600–700 nm for xylindein, 520–590

nm for dimethylxylindein) yielding a data point at time t = 0. The solutions in vials sealed with a paraffin film to prevent solvent evaporation were then placed under the fume hood lights, in air, and spectral measurements were repeated at various time intervals. The S_0-S_1 spectra were integrated and the result normalized by that at t = 0. The experiment was carried out up to 3 weeks. For accelerated photobleaching testing, 10 μM solutions were placed in front of a solar simulator (Oriel 96000 with an AM 1.5G filter) with an aluminum foil lined encasement in order to increase the uniformity and total power of the light hitting the samples. Total irradiance was roughly 100 mW/cm^2, similar to the irradiance from the sun on a clear day. Absorbance was measured every 30 minutes over the course of 5.5 hours. Sample temperature was measured at 25° C. Synthetic indigo was purchased from Sigma-Aldrich.

5.2.7 Measurements of (Opto)electronic Characteristics

For measurements of current-voltage characteristics, voltage was applied to the samples using a Keithley 237 source-measure unit and current in the dark was measured as a function of applied voltage ranging from 0–300 V. Continuous-wave (cw) photocurrents in films were measured under 100 mW/cm2 532 nm (Nd:YVO4, Coherent, Inc.) or 633 nm (HeNe) photoexcitation. For ac photocurrent measurements, the light beam was chopped using an optical chopper at 100 Hz. A dc voltage of 100 V was applied to the samples consisting of films deposited on PEIE-treated Au interdigitated electrodes with a 25 μm gap using a Keithley 237 source-measure unit. For dc photocurrent measurements, the time evolution of the total current under the continuous light excitation (which was turned on and, after 20 s, turned off with shutter) was measured using the Keithley 237 source-measure unit and the photocurrent was calculated as the difference between the total and the dark current. For ac photocurrent measurements, the photoresponse from the sample was measured using a Stanford Research Systems (SRS830) lock-in amplifier as the voltage over a 10 kΩ resistor.[125]

5.2.8 Measurements of Temperature Dependence

For temperature-dependent measurements, films deposited on PEIE-treated Au interdigitated electrodes with a 25 μm gap were incorporated in an optical cryostat (Janis STC-500), and temperature was controlled and measured with a PID temperature controller (Lakeshore model 335). Dark current and photocurrent measurements were carried out at 100 V in vacuum in the temperature range of 300–400 K with air as a coolant. Temperature-dependent photoluminescence measurements were taken from films deposited on glass substrates in the same manner except with liquid nitrogen as a coolant and in the temperature range of 100–300 K.

5.2.9 Density Functional Theory (DFT) Calculations

The geometric structure and frontier orbital energies (Table 5.1) were calculated by Density Functional Theory using the Gaussian 16 software suite with the details described in our previous publication.[57] Briefly, the geometric structure was optimized with the B3LYP function and 6-311G++(d,p) basis set along with a polarizable continuum model for DCM to simulate the solvent environment. Additionally, energies for the first excited states were calculated using time-dependent DFT in the ground state geometry; vertical transition energies are shown in Table 5.1. The triplet energies and molecular orbital energies for both xylindein and dimethylxylindein were also calculated using DFT methods (Table 5.1). An unrestricted B3LYP functional with the 6-311G++(d,p) basis set together with a polarizable continuum model for DCM was used to optimize the geometric configuration of both molecules.

5.3 Results and Discussion

5.3.1 Photophysics in Solution

Optical absorption and photoluminescence (PL) spectra of xylindein and dimethylxylindein in dichloromethane (DCM) are shown in Fig. 5.2. The absorption spectrum of xylindein exhibits a structure that is well described by two vibronic progressions, with the energies of 0-0 transitions offset by 0.06 eV (at 1.84 and 1.90 eV, or 674 nm and 654 nm) and vibrational energies of 0.13 eV and 0.16 eV (Table 5.1).[57] The presence of two vibronic progressions was previously attributed to the contribution of two xylindein tautomers, arising from different orientations of OH groups, at a 70:30 ratio.[57] In support of this finding, the absorption spectrum of dimethylxylindein, which lacks OH groups, exhibits a single vibronic progression with the 0-0 energy at 2.17 eV (~571 nm) and vibrational energy of 0.18 eV.

Table 5.1. Parameters obtained from fitting optical spectra of xylindein and dimethylxylindein solutions in DCM to Eqs. (4.1) and its analogue for PL.

Fit parameters	Xylindein (absorption)	Dimethylxylindein (absorption)	Dimethylxylindein (PL)
A_0 (norm.)	0.3; 0.7	1	1
S	0.77; 0.92	0.77	0.77
E_X (eV)	1.84; 1.90	2.18	2.07
E_V (eV)	0.13; 0.16	0.18	0.12
σ (eV)	0.06; 0.08	0.10	0.22
Δσ (eV)	0.03; 0.05	0.03	0

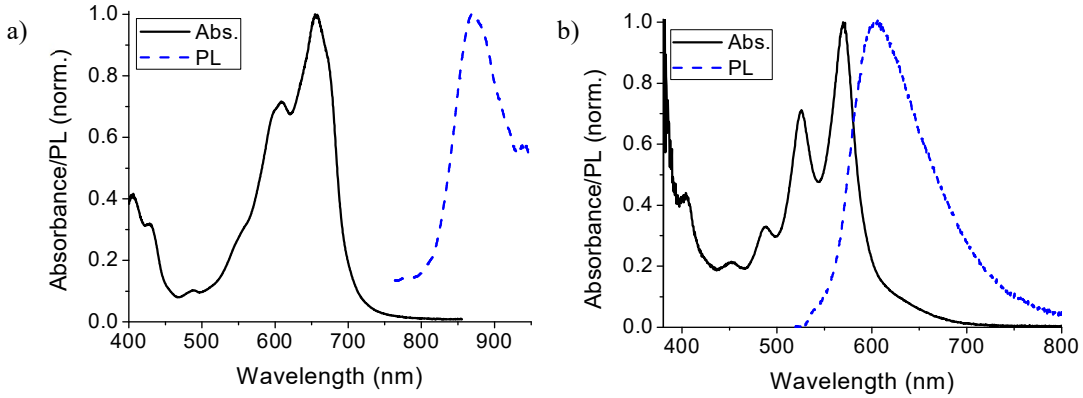

Figure 5.2. (a) Optical absorption and photoluminescence (PL) spectra of a dilute solution of (a) xylindein and (b) dimethylxylindein in dichloromethane (DCM). In xylindein (dimethylxylindein), PL was measured with a 633 nm (532 nm) excitation source.

Vibrational energies observed in xylindein and dimethylxylindein are comparable to those observed in a wide variety of conjugated molecules in which the dominant coupling occurs to a C–C/C=C stretching mode.[46,77,118,126] This is most likely the case for molecules under current study, although other vibrational modes in the 0.13–0.2 eV range, previously identified in PXX derivatives,[77] could also contribute.
The PL emission in both xylindein and dimethylxylindein was weak, with the PL QYs of below 0.1% and 0.7%, respectively, in dilute DCM solutions. The dominant PL emission of xylindein, which peaks at ~870 nm in solution (Fig. 5.2(a)), has a large Stokes shift of 0.45 eV (~211 nm) and a lifetime of below~200 ps, limited by the time resolution of our PL measurements (Fig. 5.3). This observation is consistent with results from transient absorption spectroscopy with a near-infrared probe in xylindein solutions that revealed an ultrafast excited-state intramolecular proton transfer (ESIPT) from the OH group to the neighboring carbonyl group (both OH groups in the xylindein molecular framework participate in the ESIPT process that is further supported by quantum calculations), which enables a large Stokes shift to occur on sub-picosecond time scales within the electronic excited state. These findings with a focus on ultrafast spectroscopy and photophysics will be reported in detail in a separate publication.31 Notably, the ESIPT process is nontrivial for understanding the efficient energy dissipation upon photoexcitation and the excellent (photo)stability of xylindein in the condensed phase. While the ESIPT could be considered to occur with hydroxyl groups, there was limited experimental evidence to support it and its role in (photo)conductivity, which is the focus of our current work. In contrast to xylindein, the Stokes shift in dimethylxylindein, wherein no ESIPT can occur, was considerably smaller at ~0.12 eV (~35 nm), which is comparable to a variety of PXX derivatives.17,20 The PL emission of dimethylxylindein could be described by a vibronic progression with the 0-0 energy at 2.07 eV (~598 nm) and vibrational energy of 0.12 eV (Table 5.1). The vibronic peaks were more than a factor

of two broader in the PL spectra of dimethylxylindein as compared to the absorption spectra. This trend is also common in PXX derivatives, which is indicative of differences in conformations and local environment experienced by the molecules in the ground and excited states. The dominant PL lifetime in dimethylxylindein was 250 ps, longer than that of xylindein (Fig. 5.3) but considerably shorter than typical lifetimes of previously studied PXX derivatives.[118]

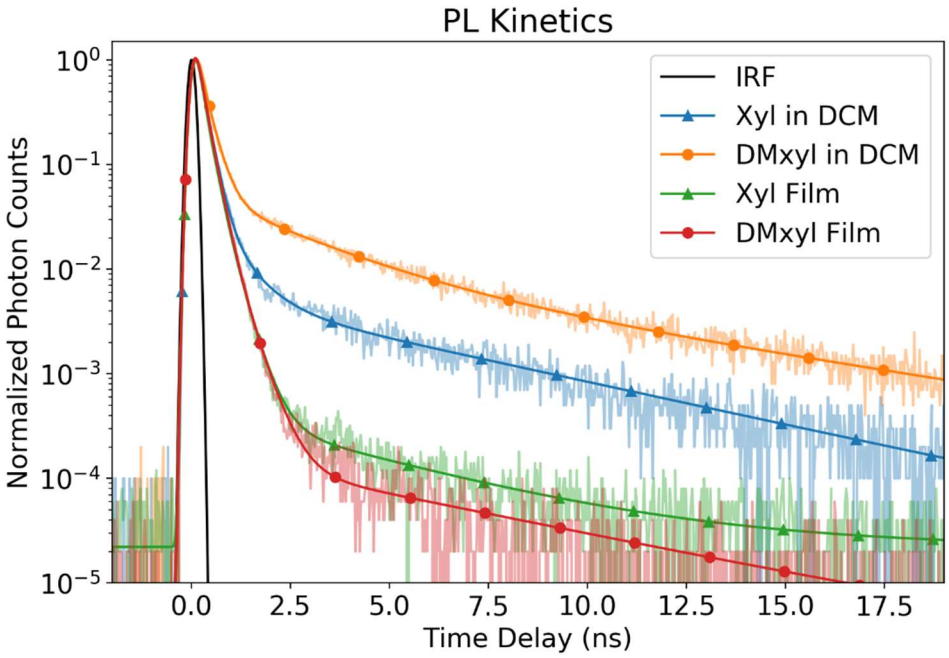

Figure 5.3. PL decay dynamics for xylindein (Xyl) and dimethylxylindein (DMXyl) in DCM solution and in pristine films obtained under a pulsed 532 nm excitation. The photon counts (normalized for a maximum value of 1) for each sample are shown with 50% opacity and fits utilizing Maximum Likelihood Estimation are overlaid with solid lines. The instrument response function (IRF) is also shown in black.

A rather low PL QY of dimethylxylindein, at 0.7%, although higher than that of xylindein (<0.1%), is interesting, considering that a variety of PXX derivatives with Stokes shifts and other features of the optical spectra similar to those of dimethylxylindein exhibit QYs of >30%.[119] In order to gain insights into this observation, the excited state dynamics of these molecules was further investigated in

ultrafast spectroscopy experiments, results of which for xylindein and dimethylxylindein in DCM solution are shown in Fig 5.4.

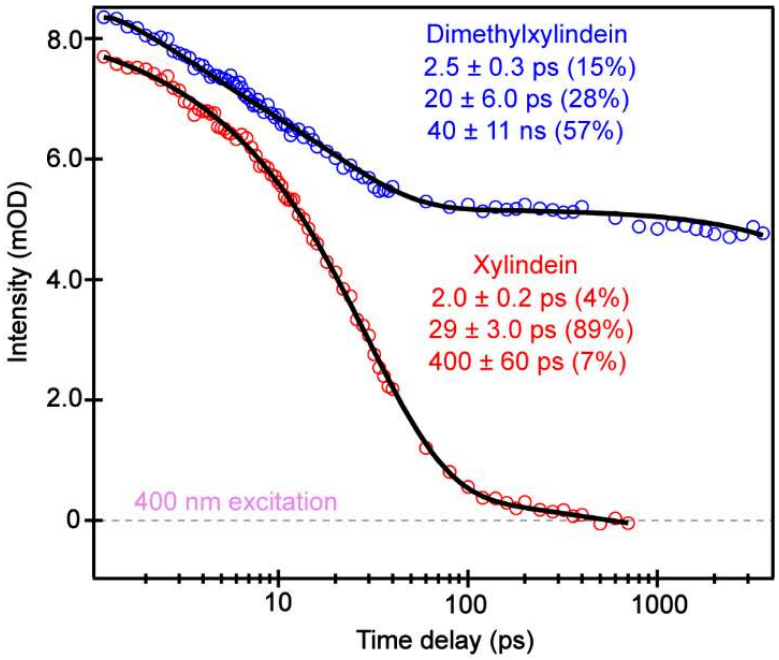

Figure 5.4. Ultrafast transient absorption obtained at 400 nm excitation as a function of pump-probe time delay for xylindein and dimethylxylindein in DCM, with associated decay rates and relative weights from the least-squares fits. The gray dashed line denotes the zero change of absorbance. Data was taken by Taylor Krueger (Fang lab, OSU Chemistry).

Following 400 nm excitation, we tracked the excited state absorption band from 515–520 nm for xylindein and from 465–470 nm for dimethylxylindein. The 400-nm actinic pump at the blue side of the S_0-S_1 electronic absorption populates higher-lying excited electronic states. We explored multiple actinic pump wavelengths and observed similar transient absorption dynamics, which infer an efficient $S_n \rightarrow S_1$ relaxation so we could focus on the decay dynamics of S_1. Both xylindein and dimethylxylindein exhibit a short (~2 ps) lifetime component accounting for ~4% and 15%, respectively, of the overall excited state relaxation, due to ultrafast solvation in the DCM environment. Both molecules also share a notable ~20–30 ps component, though this component is much more dominant in xylindein (~89%) than dimethylxylindein (~28%). The prevalence of this component in both cases rules out

the possibility of intermolecular proton transfer as the mechanism of this relaxation, since dimethylxylindein has no dissociable protons, therefore it more likely involves characteristic conformational motions on the tens of ps time scale.[127,128] Conformational changes in the unsubstituted PXX have been previously observed;[118] therein, they manifested into dependence of the Huang-Rhys factor and wavelength of emission maximum on the temperature and dependence of the excited state lifetime on solvent viscosity. For example, the thermally-activated conformational change with an activation energy of ~25–50 meV was inferred from the temperature dependence of PL spectral properties in solution. In xylindein and dimethylxylindein, the effect of conformational changes on the excited states dynamics is more dramatic, although the exact nature of the changes remains a research subject. Nevertheless, for any conformational change, the associated relaxation mechanism (responsible for the 20–30 ps lifetime) is non-radiative, and it may facilitate the molecule's approach to the S_1/S_0 conical intersection. Based on the relative contribution of this component to the overall excited state dynamics, this process is much more efficient in xylindein as compared to dimethylxylindein, and it could be responsible for the much lower PL QY in xylindein. For corroboration, we observed that the ground state bleaching (GSB) band (selected from 655–660 nm probe region) recovers with time constants of 36 ps (94%) and 300 ps (6%) in xylindein, largely matching its ESA band decay (red points in Fig. 5.4). Finally, there is a minor (7%) component with a ~400 ps lifetime in xylindein which may have a contribution from radiative relaxation manifested through the weak PL of this compound (Fig. 5.2(a)). No long-lived states were observed in xylindein (Figs. 5.3 and 5.4), confirming efficient deactivation of the excited state population in this molecule. We note that the matching ESA decay and GSB recovery of xylindein with a dominant ~30 ps time constant supports a nonradiative return directly from S_1 to S_0.

In contrast, dimethylxylindein exhibits a dominant (57% of the overall dynamics) long-lived state with a lifetime of ~40 ns (Fig. 5.4). This value represents a lower bound on the true lifetime of the long-lived state, as the exact determination is limited by our detection time span (~4 ns) of transient absorption experiments. Therefore, the true lifetime is most likely longer. The recovery of the negative GSB band of

dimethylxylindein is difficult to analyze at early times due to spectral overlap with the positive ESA band; however, the GSB band never fully recovers and we could fit it with a lifetime of 122 ns, corroborating the aforementioned ESA band decay dynamics (blue points in Fig. 5.4). The dominant presence of such a lingering component in dimethylxylindein implies the efficient formation of a dark state, which is consistent with our PL data showing no emission with a long lifetime (Fig. 5.3). Similar to the excited state deactivation via a conical intersection, the dark state formation would also contribute to the PL quenching and resulting low PL QY in this compound (Table 5.2). Additionally, it has important implications for the photostability as discussed below.

Table 5.2. Properties of molecules in solution

	HOMO [1] (eV)	**LUMO [1] (eV)**	**E_g[1] (eV)**	**S_1 [1] (eV)**	**T_1 [1] (eV)**	**Abs Max, [2] nm (eV)**	**PL Max, [2] nm (eV)**	**Stokes Shift, [3] nm (eV)**	**PLQY[4]**
Xylindein	**– 6.49; – 6.30**	**– 4.31; – 3.99**	**2.18; 2.31**	**1.89; 1.93**	**1.03**	**674, 654 (1.84; 1.90)**	**870 (1.43)**	**211 (0.45)**	**<0.1%**
Dimethyl xylindein	**– 6.35**	**– 3.89**	**2.46**	**2.14**	**1.18**	**571 (2.17)**	**606 (2.05)**	**35 (0.12)**	**0.7%**

[1]Calculated using DFT, as described in Methods. The two reported values are from xylindein tautomers A and B. For T_1, only the tautomer A energy is included. [2]Wavelength (energy) of the absorption or PL peak maximum in DCM; xylindein absorption maxima for the two tautomers were extracted from fits of the absorption spectrum to two vibronic progressions as discussed in Ref. [57]. [3]Calculated as a difference between the optical absorption and PL maxima in dilute DCM solution; in the case of xylindein, the absorption maximum (659 nm, Fig. 5.2(a)), with contribution from both tautomers, in DCM is used. [4]Measured in DCM as described in Methods.

5.3.2 Photostability

Xylindein has been known to have remarkable photostability.[57] For example, our accelerated photobleaching testing of xylindein and a well-known pigment indigo (whose enhanced photostability has been attributed to ESIPT-promoted fast deactivation of the excited state[94]) demonstrated superior stability of xylindein over indigo (Figs. 5.6 and 5.7). Elucidation of features of the xylindein molecular

structure and photophysics responsible for its enhanced photostability is thus one of the motivations for the present work. Figure 5.5 shows integrated absorption over the S_0-S_1 transition for xylindein (600–700 nm) and dimethylxylindein (520–590 nm) in solution under continuous white light exposure in air. Notably, dimethylxylindein degraded substantially after only two weeks of exposure, while xylindein showed no evidence of photodegradation under identical illumination conditions. The latter consistent with our previous studies[57] in which xylindein lasted 25 weeks under the same illumination conditions before showing any signs of photodegradation, whereas TIPS-Pn decomposed within just three days. Similar trends for xylindein vs dimethylxylindein stability were observed under accelerated photobleaching testing conditions (Figs. 5.6 and 5.7). Significant photodegradation was also observed in deprotonated xylindein, further demonstrating the importance of the hydroxyl group to the photostability of the molecule. The stark difference between the stability of xylindein and dimethylxylindein molecules can be related to the dramatic differences in their excited state dynamics revealed by transient absorption spectroscopy discussed above (Fig. 5.4). The dominant ~30 ps nonradiative deactivation of the excited-state xylindein prevents efficient interaction of this molecule with oxygen, thus extending its lifespan. In contrast, dominant formation of a long-lived dark state in dimethylxylindein could facilitate interactions with oxygen, thus promoting formation of reactive oxygen species and consequent destruction of the parent molecule. We hypothesize that the dark state is a triplet state (T_1) and an effective degradation pathway is facilitated by energy transfer from the triplet state of dimethylxylindein to the ground-state triplet oxygen. Such energy transfer would be enabled by the triplet energy of dimethylxylindein (1.18 eV, Table 5.2) that is higher than 0.98 eV necessary to generate the reactive singlet oxygen species.[114,129]

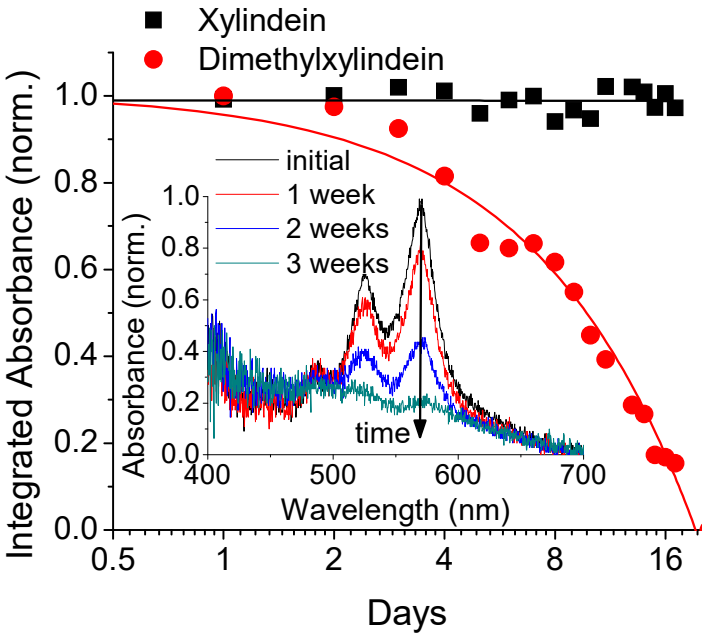

Figure 5.5. Integrated absorption spectra of xylindein and dimethylxylindein solutions in DCM versus time during exposure to white light in air. Trend lines are added to guide the eye. Inset shows dimethylxylindein absorption spectra at periodic intervals as the compound degrades upon exposure to light.

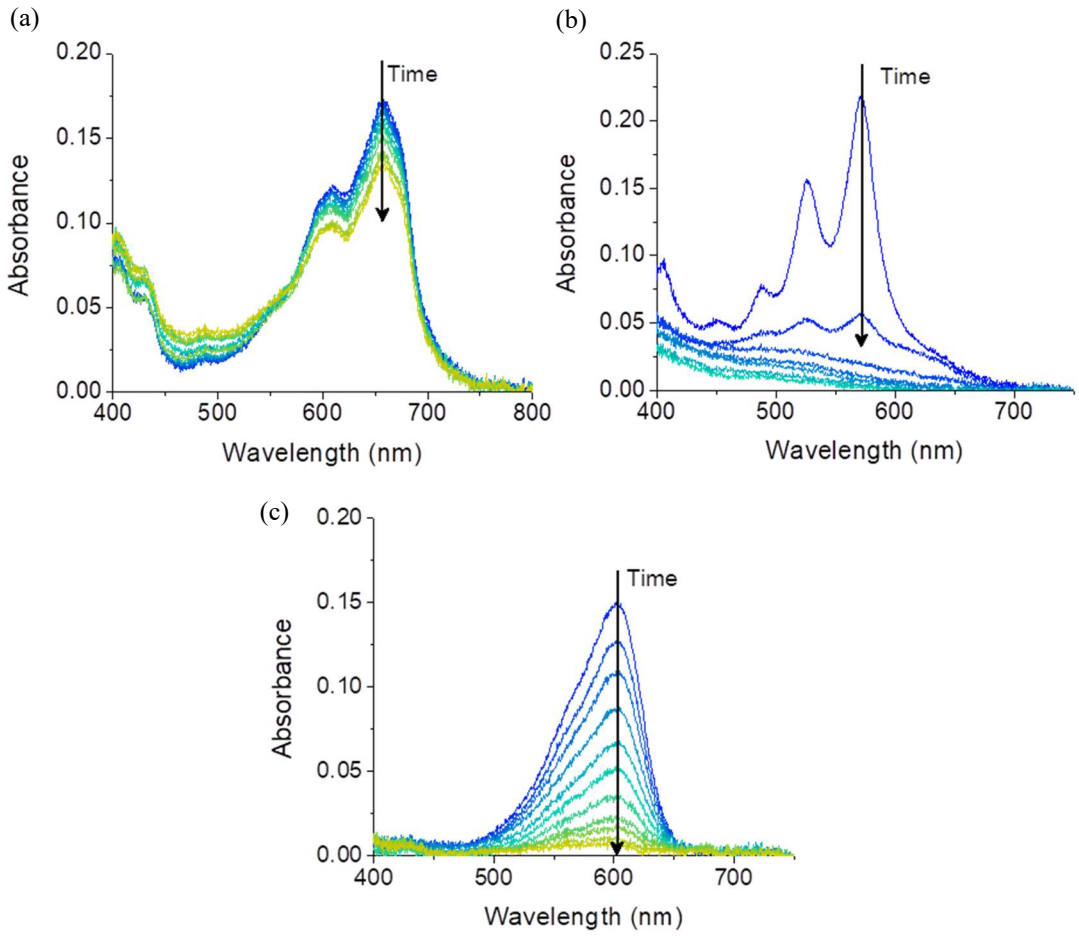

Figure 5.6. Absorbance spectra of 10 µM solutions of xylindein (a) dimethylxylindein (b), and indigo (c) in chloroform under continuous bright white light conditions. Absorbance measurements were taken every half hour, over the course of 5.5 hours. Only 3 hours' worth of data is shown for dimethylxylindein (b) due to the rapid bleaching of the molecule. Solutions were placed in front of a solar simulator (Oriel 96000 with an AM 1.5G filter) with an Al foil lined encasement in order to increase the uniformity and total power of the light illuminating the samples. Total irradiance was roughly 100 mW/cm^2, similar to the irradiance from the sun on a clear day.

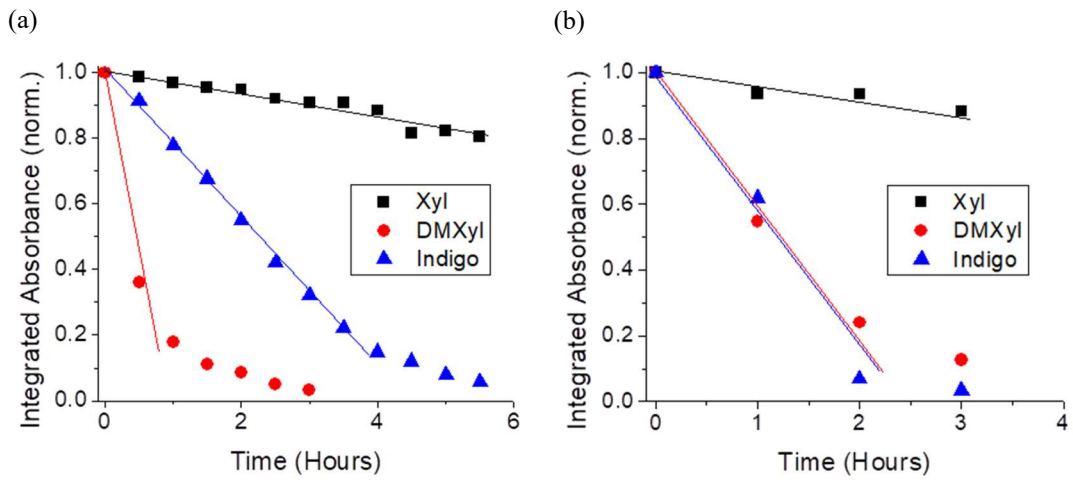

Figure 5.7. Integrated absorbance spectra as a function of time for chloroform (a) and DCM (b) solutions. Absorbance spectra (from Fig. 5.5 for (a)) were integrated of the S0-S1 transition (550-700nm for xylindein (a), 500-600nm for dimethylxylindein (b), and 500-650nm for Indigo(c)) to compare the rate of photobleaching under continuous simulated solar irradiation. Dilute (10 μM) solutions and bright white light (~100 mW/cm^2 AM1.5G) conditions were used. Lines are drawn as guides for the eye. In both solvents, xylindein exhibited photostability superior to that of indigo.

5.3.3 Optical Absorption and Photoluminescence: Films

Thin films of xylindein are amorphous, and no evidence of crystallization was observed regardless of film deposition conditions or processing. This is consistent with previous work:[63] although xylindein did crystallize when processed from hot phenol, solvent molecules were incorporated in the crystal structure; the attempts for their removal resulted in crystal collapsing, yielding an amorphous solid instead. In contrast, dimethylxylindein was prone to forming microscopic crystals, and so pristine dimethylxylindein films had both an amorphous and a crystalline phase as confirmed by XRD (Fig. 5.8). The two phases coexisted and the film morphology depended on deposition conditions; however, even in the best samples, crystallites were small and randomly oriented, resulting in rough disordered films, an observation similar to literature on unsubstituted PXX.[41] Our previous work with xylindein showed that 4:1 blends of xylindein with PMMA exhibited optical and electronic properties comparable with those of pristine xylindein, but had an improved film morphology and processability.[56] The same strategy was applied here to prevent

crystallization and create more homogeneous dimethylxylindein films, thus 4:1 blends of dimethylxylindein:PMMA were investigated in addition to pristine dimethylxylindein films. In the discussion below, these films, with a minimized formation of the crystalline phase, will be referred to as “amorphous”. Pristine dimethylxylindein films which had both amorphous and crystalline regions will be referred to as “crystalline”.

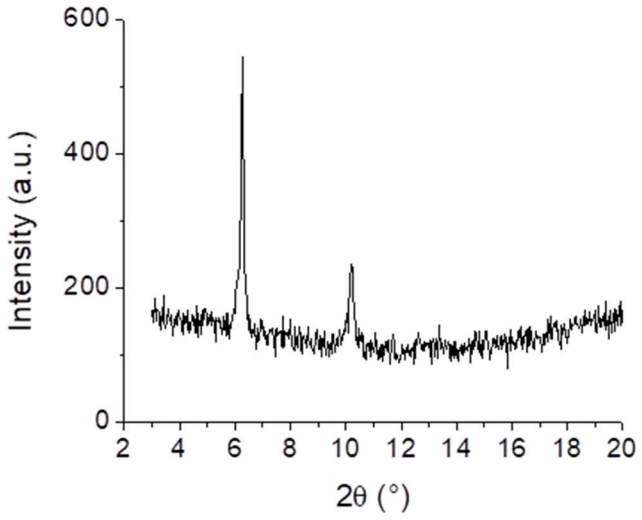

Figure 5.8. X-ray diffraction from a pristine thin film of dimethylxylindein. The features correspond to d-spacings of 14.1 Å and 8.7 Å. No such features were observed in xylindein films.

Figure 5.9 shows optical absorption and PL emission spectra for pristine xylindein, dimethylxylindein:PMMA, and pristine dimethylxylindein films. All absorption spectra exhibit a redshift Δ (see Table 5.3) in film with respect to those in solution, as well as peak broadening. These features have been previously attributed to enhanced intermolecular interactions in the film.[88,125] Amorphous xylindein film shows a larger Δ of ~110 meV (42 nm) as compared to ~70 meV (20 nm) in amorphous dimethylxylindein:PMMA film, but lower than ~240 meV (72 nm) in the crystalline pristine dimethylxylindein film (Fig. 5.9(b)). Varying solution-solid redshifts Δ have been previously observed in films of varying morphology and crystallinity; for

example, amorphous TIPS-Pn films exhibit shifts Δ lower than 10 nm, whereas shifts of 45–70 nm were obtained in crystalline TIPS-Pn films.[125] A similar trend was obtained here in dimethylxylindein films, wherein an interplay of the absorption features of the amorphous and crystalline regions was observed in the optical absorption spectra, depending on film morphology (Fig. 5.10). Given that there is no crystalline order present in xylindein films, a relatively large solution-solid redshift Δ could be related to the enhanced intermolecular interactions due to intermolecular H-bonding which is absent in dimethylxylindein. A similar effect of H-bonding on Δ has been previously observed in other H-bonded pigments.[116] The redshift in the optical absorption was accompanied by a redshift in the PL emission spectra of films as compared to solutions, in both xylindein and dimethylxylindein, such that the dominant PL emission of xylindein films is at ~930 nm and that in dimethylxylindein films is at ~670–720 nm depending on morphology. The PL emission spectra from amorphous dimethylxylindein:PMMA and crystalline pristine dimethylxylindein films are shown in Fig. 5.9(b), illustrating a redshift in the dominant emission from crystalline versus amorphous regions. Both xylindein and dimethylxylindein films exhibited short dominant PL lifetimes of <200 ps, limited by the time resolution of our PL measurements (Fig. 5.3).

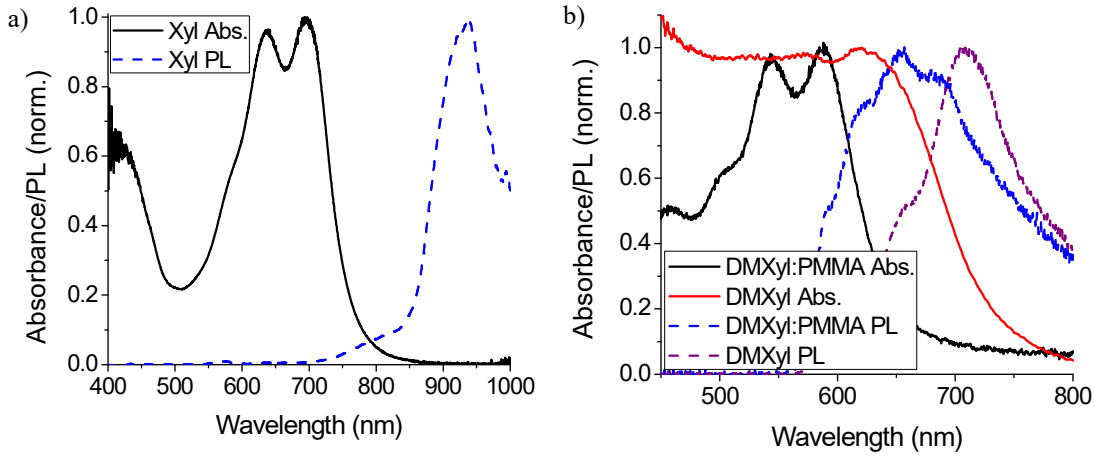

Figure 5.9. (a) Optical absorption and PL spectra of a xylindein film. PL was measured under 633 nm excitation. (b) Optical absorption and PL spectra of amorphous dimethylxylindein:PMMA and crystalline pristine dimethylxylindein films. PL spectra were measured under 532 nm excitation.

Table 5.3. Optical and (photo)conductive properties of films

	Δ, [1] nm (eV)	Abs Max,[2] nm	PL Max,[2] nm	$E_{a,PL}$[3] (eV)	μ_{eff}[4](cm^2/(Vs))	$E_{a,dark}$[5] (eV)	$E_{a,photo}$[6] (eV)
Xylindein	**42 (0.11)**	**701**	**933**	**0**	**0.05**	**0.24**	**0.18**
Dimethylxylindein :PMMA	**20 (0.07)**	**591**	**649**	**0**	**1.1×10^{-6}**	**0.46**	**0.23**
Pristine dimethylxylindein	**72 (0.24)**	**643**	**713**	**0.082**	**1.1×10^{-6}**	**0.61**	**0.23**

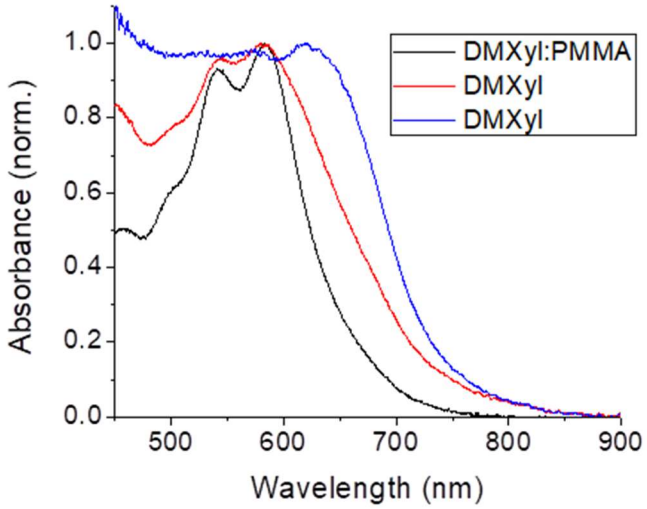

Figure 5.10. Normalized absorption spectra from amorphous dimethylxylindein:PMMA (DMXyl:PMMA) and pristine dimethylxylindein (DMXyl) films with more pronounced amorphous (red) and crystalline (blue) morphologies. More crystalline films exhibit formation of a redshifted absorption band, consistent with aggregation and associated exciton delocalization.

Pristine dimethylxylindein films exhibit features of photodegradation under continuous 532 nm illumination in air, as shown in its PL spectral evolution (Fig. 5.11). No such degradation was observed in xylindein or amorphous dimethylxylindein:PMMA films, which may suggest that the mechanism of photodegradation in crystalline dimethylxylindein films relies on particular

intermolecular arrangements that facilitate formation of dimers, as has been observed in, for example, crystalline acenes.[126]

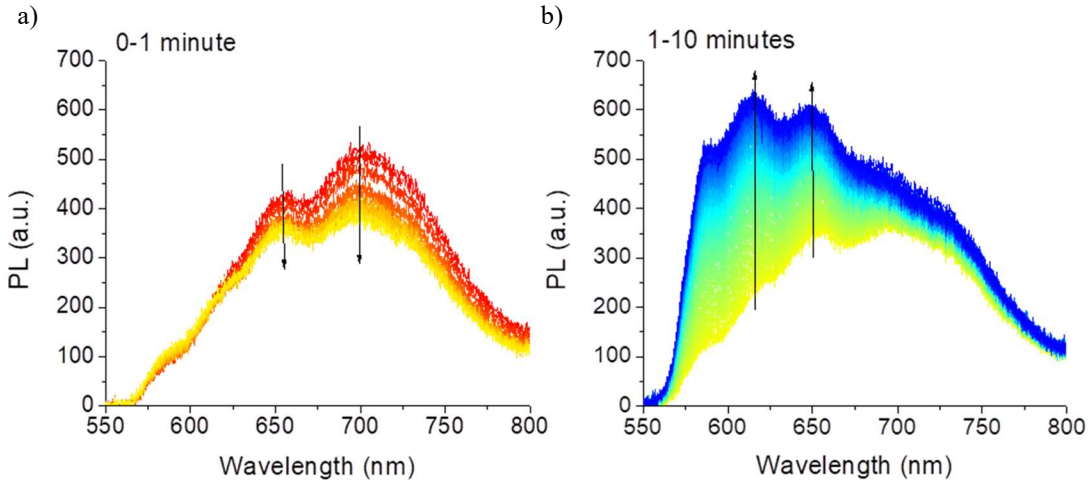

Figure 5.11. PL spectra evolution for a pristine dimethylxylindein film measured over 10 minutes under continuous illumination from a 532nm cw laser at ~100 W/cm^2 in air, due to photodegradation. The film exhibits a notable decrease in the intensity of PL at longer wavelengths at shorter time scales (below 1 min) followed by an increase in the PL intensity at shorter wavelengths at longer times.

Similar to solution, the Stokes shift in xylindein films (~230 nm) is considerably larger than that in dimethylxylindein-based films (~60–70 nm) (Table 5.3). This suggests that the ESIPT, responsible for a large Stokes shift of xylindein in solution, proceeds on ultrafast time scales in the xylindein solid form as well.

In addition to differences in the PL spectral characteristics, amorphous dimethylxylindein:PMMA and crystalline pristine dimethylxylindein films exhibited drastically different temperature dependence in the 80 – 300 K temperature range. In particular, the amorphous binary film showed weak temperature dependence in the entire temperature range studied; the same behavior was observed in xylindein films. In contrast, the PL from pristine dimethylxylindein film exhibited a strong, fully reversible, temperature dependence below ~200 K (Fig. 5.12). We attribute this feature to a decreased exciton diffusion at low temperatures, which inhibits nonradiative recombination, resulting in a higher QY. This can be modelled with a thermally activated nonradiative decay rate, k_{nr} (T):[88]

$$k_{nr}(T) = k_{nr}^{0} + k_{nr}^{*}\, e^{-\frac{E_{a,PL}}{k_B T}} \tag{5.1}$$

Here, k_{nr}^{0} and k_{nr}^{*} are constants, k_B is the Boltzmann constant, and $E_{(a,PL)}$ is the activation energy. The PL intensity can be modelled as follows:

$$I(T) \propto \frac{k_r}{k_r + k_{nr}(T)} \tag{5.2}$$

where k_r is the temperature-independent radiative rate. The integrated PL spectra (Fig. 5.12) were fit to Eq. (5.2) to extract an activation energy $E_{a,PL}$ of (82 ± 5) meV. Similar behavior has been observed in a variety of polycrystalline films,[88,130] for example those of functionalized ADT derivatives or Alq3 with activation energies of ~69 meV[46] and ~74 meV,[131] respectively. Considerably weaker temperature dependence of PL in amorphous than crystalline films, observed in dimethylxylindein, has been previously reported in, for example, Alq3 films.[131] This finding indicates that thermally-activated exciton diffusion to the PL quenching sites, which causes non-radiative recombination, is considerably more efficient in crystalline regions than that in amorphous regions.

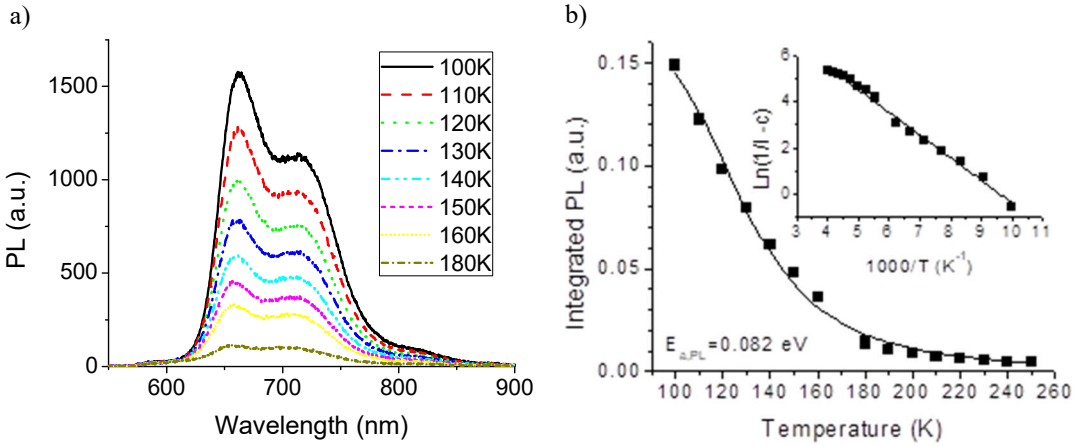

Figure 5.12. (a) PL spectra from a crystalline pristine dimethylxylindein thin film at temperatures below 200 K. (b) Integrated PL for crystalline dimethylxylindein film versus temperature, fit with Eq. (5.2). Inset shows a linearized version of the data to show quality of fit, where I is the integrated PL and c is a constant extracted from the fit related to k_{nr}^{0} in Eq. (5.1).

5.3.4 Conductive and Photoconductive Properties

Conductive properties were investigated by measuring current-voltage (I-V) characteristics of pristine xylindein, dimethylxylindein:PMMA, and pristine dimethylxylindein films deposited on coplanar electrodes. Different electrode metals such as Au and Al, as well as different electrode treatments were investigated to optimize electrical performance, aiming to reduce contact resistance and improve matching of the work function to the free carrier energy level of the material. In our previous work,[57] xylindein films performed considerably better on Al electrodes (work function of ~4.2 eV) than the untreated Au electrodes (work function of ~5.1 eV), with effective electron mobilities of 0.1–0.4 $cm^2/(Vs)$ obtained from space-charge-limited currents (SCLCs). This is consistent with the expectations of a preferential electron transport in xylindein, supported by DFT calculations of the HOMO and LUMO energies of xylindein, which yielded −6.49 (−6.30) and −4.31 (−3.99) eV, respectively, for the two xylindein tautomers (Table 5.2) present in our samples. In dimethylxylindein, DFT calculations of the HOMO and LUMO orbitals yielded HOMO and LUMO energies of –6.35 eV and –3.89 eV. The low LUMO energy of dimethylxylindein suggests that similar to xylindein, dimethylxylindein should exhibit a preferential electron or ambipolar transport. In accord with these expectations, and similar to xylindein, the currents improve by a factor of 3–5 in dimethylxylindein films on Au electrodes treated with a thin layer of polyethylenimine ethoxylated (PEIE) to effectively reduce the work function (e.g. to 3.9 eV as measured by Kelvin probe in air in Ref. [120]) versus those on untreated Au electrodes.

Figure 5.13(a) shows the room-temperature I-V characteristics of pristine xylindein, dimethylxylindein:PMMA, and pristine dimethylxylindein films on PEIE-treated Au electrodes. Xylindein films exhibited more than four orders of magnitude higher currents than either dimethylxylindein:PMMA blend or pristine dimethylxylindein films. The SCLC regime where current varies quadratically with respect to voltage[23,57] was observed in all samples at high voltages.

In the case of the planar electrode geometry used in our experiments, the current flows along a thin layer of unknown thickness, and the current density (j) is expressed in units of A/m (as opposed to A/m^2 for the "sandwich" electrode geometry). Although there is no analytical solution for the relationship between the SCLC linear current density (j) and the applied voltage (V) in a film of finite thickness on coplanar electrodes, there are solutions for the extreme cases of the infinitely thin film ("thin-film approximation") and the infinite half-space ("infinite half-space approximation").[45] In the thin-film regime, the linear current density (j) is $j = (2/\pi)\mu_{eff}\varepsilon\varepsilon_0 V^2/L^2$. Here $j = I/d$, where I is the measured current and d is the length of the electrode, L is the gap between the electrodes, ε_0 is the vacuum permittivity, ε is the dielectric constant (assumed here to be equal to 3), and μ_{eff} is the effective mobility. The SCLC j−V dependence in the infinite half-space approximation differs from the expression above only in the coefficient $2/\pi$, which is replaced by 0.28.[45] Our films are 3-5 μm thick, and thus for the electrode geometry with the 5 μm gap (L) used for measurements in Fig. 5.13, neither the thin-film nor the half-space approximation is strictly valid and the true effective mobility lies in between the values obtained in these extreme cases. The choice of the small gap L was dictated by the need to achieve measurable currents in dimethylxylindein-based films in a wide range of applied voltages necessary to probe the transition from the linear to the SCLC regime.

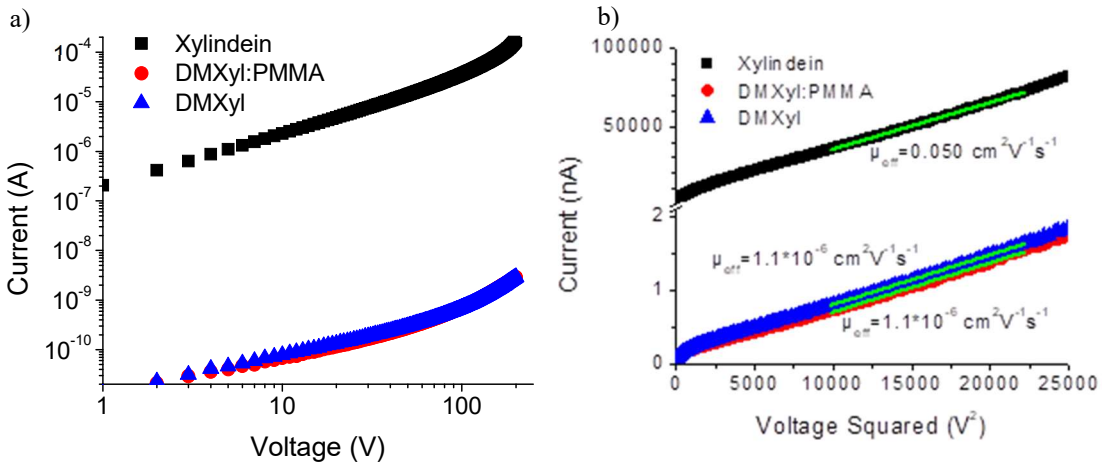

Figure 5.13. (a) Current-voltage characteristics for xylindein, dimethylxylindein:PMMA, and pristine dimethylxylindein (DMXyl) films. (b) Current versus voltage squared and linear fits to the data. The slope of the linear fit was used to calculate the effective SCLC mobilities, shown for the case of the infinite half-space approximation discussed in the text.

Figure 5.13(b) shows current versus voltage squared for xylindein, dimethylxylindein:PMMA, and pristine dimethylxylindein films, all on PEIE-treated Au electrodes, along with linear fits from which the effective electron mobility μ_{eff} was extracted. In this geometry, xylindein exhibited effective electron mobility of ~0.022 $cm^2/(Vs)$ (0.05 $cm^2/(Vs)$) in the thin-film (half-space) approximation. These values for the effective mobilities should be considered a lower bound on actual electron mobility in these materials since trap-free SCLC regime was not achieved in either film. The effective mobility in xylindein films was more than four orders of magnitude higher than ~5×10^{-7} $cm^2/(Vs)$ (1.1×10^{-6} $cm^2/(Vs)$) obtained in both dimethylxylindein:PMMA and pristine dimethylxylindein films in the thin-film (half-space) approximation. In order to confirm that the observed drastic differences in electronic characteristics of xylindein and dimethylxylindein films are not driven by surface states, we investigated I-V characteristics of films in conventional sandwich cell geometry. In this geometry, pristine xylindein and dimethylxylindein could not be studied due to their porous and polycrystalline structure, respectively, prone to creating electrical shorts. Therefore, xylindein:PMMA and dimethylxylindein:PMMA films at relatively high dilution (i.e. high PMMA content, at 1:1 and 1:2 weight ratio) were employed, demonstrating similar trends to those observed in devices with planar geometry of Fig. 5.13.

In order to explore the mechanism of conduction in films under study, temperature-dependent measurements of the I-V characteristics were carried out. Figure 5.14(a) shows temperature dependence of dark currents obtained in xylindein and dimethylxylindein films. All samples exhibited a thermally activated response (~$\exp[-E_{a,dark}/k_BT]$, where $E_{a,dark}$ is the activation energy, k_B is the Boltzmann constant, and T is the temperature), characteristic of thermally activated hopping of

charge carriers between states exponentially distributed in energy. Dark currents in xylindein films exhibited activation energies of ~0.24 eV, similar to 0.24−0.25 eV previously obtained in blends of xylindein with PMMA or nanocellulose.[57] These activation energies are slightly lower than that of 0.3 eV obtained in pristine xylindein films on untreated substrates with Au electrodes,[57] which is due to an improved interface morphology resulting from the PEIE treatment of the Au electrodes. The activation energies for dark currents in dimethylxylindein films were substantially higher than those for xylindein films, yielding ~0.46 and 0.61 eV in dimethylxylindein:PMMA and pristine dimethylxylindein films, respectively (Fig. 5.14(a)), indicative of the presence of deep charge traps in both dimethylxylindein-based films. The higher activation energy in the crystalline pristine dimethylxylindein films suggests that the crystallite boundaries create an additional source of deep traps. At higher temperatures, with additional thermal energy that promotes charge release from traps and enhances hopping, the difference between dark currents in xylindein and dimethylxylindein films was significantly reduced and thus, the intrinsic mobilities of these two materials are closer than Fig. 5.13(b) would suggest. However, even at 400 K (the highest temperature in our measurements) the currents in xylindein films were about a factor of ~50 higher than those in dimethylxylindein films.

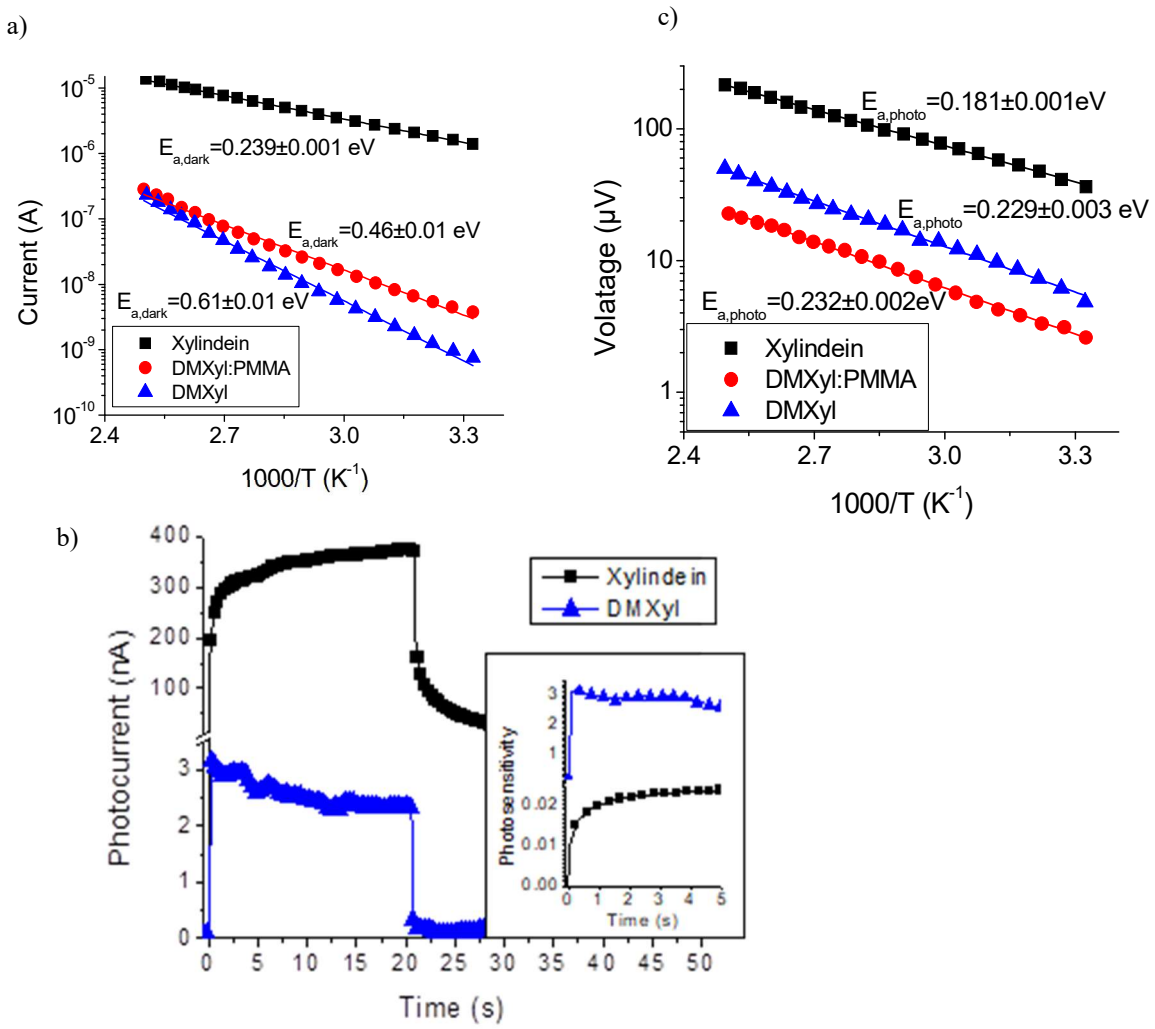

Figure 5.14. Temperature dependence of dark (a) and ac photo (c) currents obtained in pristine xylindein, dimethylxylindein:PMMA, and pristine dimethylxylindein (DMXyl) films. Arrhenius fits (~exp[–E_a/k_BT]) with the extracted activation energies $E_{a,dark}$ and $E_{a,photo}$ are also included. The temperature dependence was independent of the applied voltage in the range studied. (b) Photocurrent from pristine xylindein and dimethylxylindein films at 100 V under 532 nm cw laser illumination turned on at time t = 0 and off after 20 seconds. Inset shows the photosensitivity of the same films, defined as a ratio of the photocurrent to dark current.

The substantial difference in charge transport properties of xylindein and dimethylxylindein:PMMA films may indicate the importance of intermolecular H-bonding, discussed above in the context of optical properties, for creating molecular networks with enhanced conductive properties and reduced charge trapping. It was

demonstrated[117] that intermolecular H-bonding can enhance charge transfer integrals by reducing the intermolecular distance and facilitating the electronic wave function overlap. For example, in crystalline ellipticine, similar charge carrier mobilities were obtained in the H-bonding and π-π stacking directions (4.2 $cm^2/(Vs)$ and 6.5 $cm^2/(Vs)$, respectively).[117] In amorphous xylindein and dimethylxylindein:PMMA films, although some differences are expected in the π-π stacking properties due to the bulky OMe side groups in dimethylxylindein as compared to the OH groups in xylindein, we hypothesize that the H-bonding enabled in xylindein but not in dimethylxylindein plays a dominant role in differences between charge-transport properties of these two materials. Interestingly, in pristine dimethylxylindein films, the presence of crystalline regions did not result in higher effective charge carrier mobility than that in amorphous dimethylxylindein:PMMA films, at least in the 300—400 K temperature range studied, because of poor morphology leading to enhanced charge trapping.

Next, we examined the photoconductive properties of all films under a 532 nm and 633 nm continuous-wave excitation. Similar to dark currents, the photocurrents obtained from xylindein films were higher than those in dimethylxylindein:PMMA and pristine dimethylxylindein films, but the difference in the photocurrents was smaller than that in the dark currents. For example, at room temperature the dc photocurrents measured under the same illumination conditions excitation were about two orders of magnitude higher in xylindein than in dimethylxylindein (Fig. 5.14(b)), for both excitation wavelengths studied, as compared to about four orders of magnitude difference in dark currents in the same samples. This behavior can be understood from comparisons of the photosensitivity of xylindein and dimethylxylindein, defined as the ratio of photocurrent to dark current (inset of Fig. 5.14(b)). In particular, the photosensitivity was considerably higher in dimethylxylindein, which suggests a significantly higher charge photogeneration efficiency in this material versus xylindein. This is most likely due to the differences in the excited state dynamics of these two compounds discussed above (Fig. 5.4). While the exact mechanism of charge photogeneration in these films requires further

investigation, it is possible that exciton interaction with defects would need to be invoked in order to overcome high Frenkel exciton binding energy (≳0.3 eV, Table 5.1). Such process would rely on exciton diffusion and depend on the exciton lifetime; for example, in rubrene crystals the charge photogeneration relies on long-range diffusion of triplet excitons to surface electron traps that promote exciton dissociation.[132] If a similar mechanism is responsible for charge photogeneration in films under study, fast depopulation of the excited state in xylindein, which is much less efficient in dimethylxylindein, would limit the efficiency of exciton dissociation into mobile charge carriers, leading to observations in the inset of Fig. 5.14(b).

The difference between the ac photocurrents in xylindein and dimethylxylindein films was reduced as compared to that for the dc photocurrents, from two orders of magnitude to a factor of ~10−20 at 100 Hz at room temperature (Fig. 5.14(c)). This reduction is due to the pronounced contribution of shallow traps to the photocurrents in xylindein which leads to the considerably slower photocurrent dynamics[133] in xylindein films, as compared to dimethylxylindein (Fig. 5.14(b)), and manifests into frequency-dependent photoresponse.[125]

In order to better understand the contribution of traps to the photoresponse versus dark currents, we investigated temperature dependence of the ac photocurrent in all films under study (Fig. 5.14(c)) and compared it to that of the dark currents (Fig. 5.14(a)). Similar to dark currents, the observed temperature dependence of the photocurrents could be well described by the Arrhenius function ($\sim\exp[-E_{a,photo}/k_BT]$). However, in contrast to dark currents, the activation energy for the ac photocurrents $E_{a,photo}$ was considerably lower, at ~0.18 eV for xylindein films (similar to that previously observed in xylindein:PMMA blends[57]) and ~0.23 eV for both dimethylxylindein:PMMA and pristine dimethylxylindein films. The observed $E_{a,photo}$ values, and the considerably lower activation energies for ac photocurrents as compared to dark currents are common for a variety of organic materials; for example, in an organic DCDHF glass, activation energies of 0.18 eV (0.72 eV) were obtained from the temperature dependence of photo (dark) currents.[111] The lower values of $E_{a,photo}$ as compared to $E_{a,dark}$ suggest that a considerably smaller subset of states is participating in the photoinduced charge transport sampled at millisecond

time-scales as compared to that of injected carriers, and so deep charge traps contributing to the dark current in dimethylxylindein films do not contribute to the ac photocurrent.

5.4 Conclusions

We compared optical and (opto)electronic properties of fungi-derived pigment xylindein and its methylated derivative, dimethylxylindein via an integrated platform from wood sciences, organic synthesis, ultrafast spectroscopy, quantum chemistry calculations, to device physics. The hydroxyl groups in xylindein, which are not present in dimethylxylindein, were found to play a critical role in optical absorption and PL properties, excited state dynamics, photostability, and conductivity. Enhanced photostability of xylindein is attributed to fast deactivation of the excited state; this channel is not as efficient in dimethylxylindein with a long-lived dark (triplet) state formation being observed instead, which considerably reduces its photostability. At room temperature, amorphous xylindein films were found to be over four orders of magnitude more conductive than both amorphous and crystalline dimethylxylindein films. On the other hand, the photosensitivity of dimethylxylindein films is considerably higher than that of xylindein films, attributed to higher photogeneration efficiency in dimethylxylindein. Charge transport was thermally activated in all films under study, with the activation energies considerably lower in xylindein films as compared to dimethylxylindein films. The observed large difference in electronic properties is partly attributed to H-bonding in xylindein which promotes morphology supportive of efficient conductive network in xylindein films and reduces the average charge trap depth.

Chapter 6: Xylindein Device Applications

6.1 Introduction

Organic semiconductors have been explored in a number of electronic device applications in recent years. Three of the most common device applications are organic light emitting diodes (OLEDs), organic field effect transistors (OFETs), and organic photovoltaics (OPVs). OLEDs have already reached a level of performance such that they are widely used in state-of-the-art display technologies in consumer electronics. OFETs and OPVs are not widely used in industry, but still widely researched with performance metrics that are steadily increasing over the years, as discussed below. Xylindein was investigated for use in OFET, OPV, and more device applications. The remarkable photostability, decent electron mobility, sustainability, and non-toxicity make xylindein an appealing candidate for (opto)electronic device applications.

6.1.1 Organic Field Effect Transistors

OFETs are three terminal devices in which source and drain electrodes are in contact with an organic semiconductor whose conductivity is modulated by a gate electrode separated from the semiconductor by a dielectric layer in a capacitive structure. The applied voltage at the gate electrode controls the concentration of charge carriers in the semiconductor, thus modulating the current between source and drain electrodes, turning on or off. OFETs typically operate in accumulation mode, in which the device is in an off state when there is little to no gate bias, and an on state when the appropriate gate bias is applied. For example, an OFET based on a p-type material will turn on when a negative gate bias is applied, inducing an excess of positive charge carriers in the material. The source drain current has two regimes: linear, where the current varies linearly with the drain voltage, and saturated, where the current is independent of the drain voltage. The transition between the two regimes occurs at the threshold voltage V_T and can be modeled with the following equations.

$$I_{SD} = \frac{W}{L} C_i \mu (V_G - V_T) V_D \quad 6.1$$

For the linear regime ($V_G < V_T$).

$$I_{SD} = \frac{W}{2L} C_i \mu (V_G - V_T)^2 \quad 6.2$$

For the saturated regime ($V_G > V_T$). Here, *L* and *W* are the length and width respectively of the gap between source and drain electrodes, C_i is the capacitance per unit area of the gate dielectric, and μ is the charge carrier mobility. OFETs are useful not only in that they are functional devices, but that the charge carrier mobility can be extracted from the current-voltage curves, although this also depends heavily on the quality of the semiconductor film and other device materials. Current voltage characteristics are typically measured as either source-drain current with respect to drain voltage at several constant gate voltage values (known as the output characteristics), or as source-drain current with respect to gate voltage at constant drain voltage (known as the transfer characteristics). Charge carrier mobility can be extracted in the linear regime from the slope of the output characteristics, or in the saturated regime from the slope of the square root of the current in the transfer characteristics, though it is more common to extract the mobility from the saturated regime. Charge carrier mobility is also the most important material parameter that affects overall device performance.[25,26] OFETs were first developed in the 1980's with charge carrier mobilities of 10^{-5} $cm^2/V^{-1}s^{-1}$.[15] Performance has advanced rapidly since then, today with charge carrier mobilities in excess of 10 $cm^2/V^{-1}s^{-1}$.[25,26] This exceeds the performance of amorphous silicon at ~1 $cm^2/V^{-1}s^{-1}$, but is still much lower than that of crystalline inorganic materials. Figure 6.1 illustrates the evolution of OFET performance over the past 35 years.

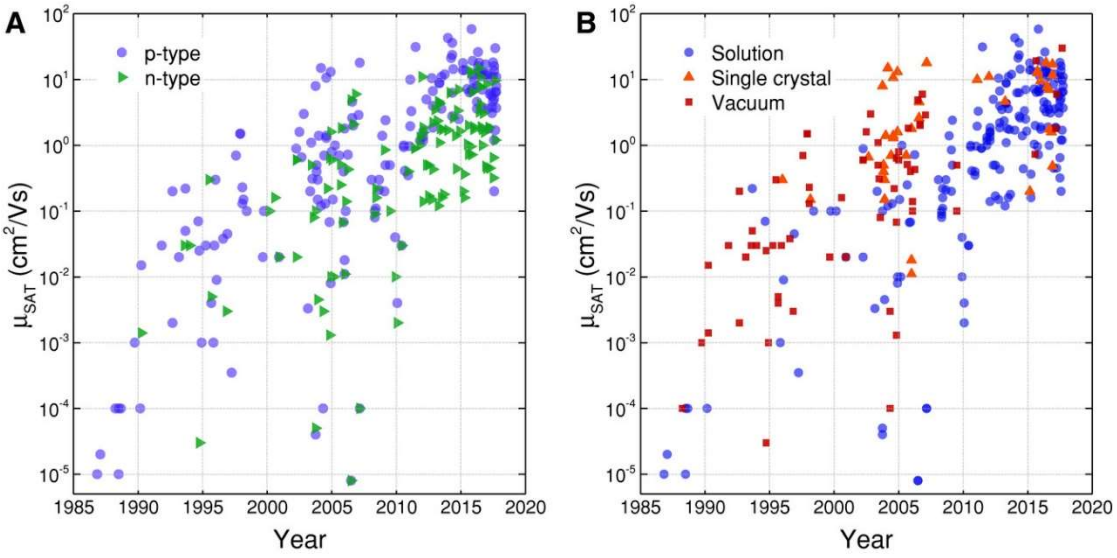

Figure 6.1. OFET mobility values over time, from reference [5]. The data is categorized by charge carrier type (a), and processing technique (b).

6.1.2 Organic Photovoltaics

Organic solar cells are constructed as a diode structure with a thin organic active layer in the middle. The active layer is typically comprised of a heterojunction of a p-type donor material and an n-type acceptor material. When light is absorbed at the interface of these two materials, an exciton is created and enters a charge transfer state due to the difference in energy of the HOMO and LUMO on the donor and acceptor material. The built-in voltage of the diode structure creates an electric field sufficient to dissociate the electron and hole in order to extract charge and supply electrical power. The diode structure can be achieved with a low work function metal as one electrode, and a high work function metal on the other side. Performance can be increased by adding interfacial layers to further reduce or increase the work function on either side of the active layer to increase the built-in voltage and block opposite charge carriers. In order to maximize the interfacial area between donor and acceptor in the active area to support the formation of charge transfer states, the donor and acceptor materials are commonly mixed together to form what is known as a bulk heterojunction (BHJ).

There are several key metrics in measuring performance of the solar cells (Fig. 6.2). There is the short circuit current density (J_{SC}), which is the current density at 0V. The open circuit voltage (V_{OC}) is likewise the voltage at zero current. At some point in between these two extrema there a maximum power (P_{Max}). Perhaps the most important figure of merit for a solar cell is the power conversion efficiency (PCE), defined as the ratio of P_{Max} to the power of light incident upon the cell. Related to this is the fill factor, which is a measure of internal efficiency defined as the ratio of P_{Max} to the product of J_{SC} and V_{OC}.

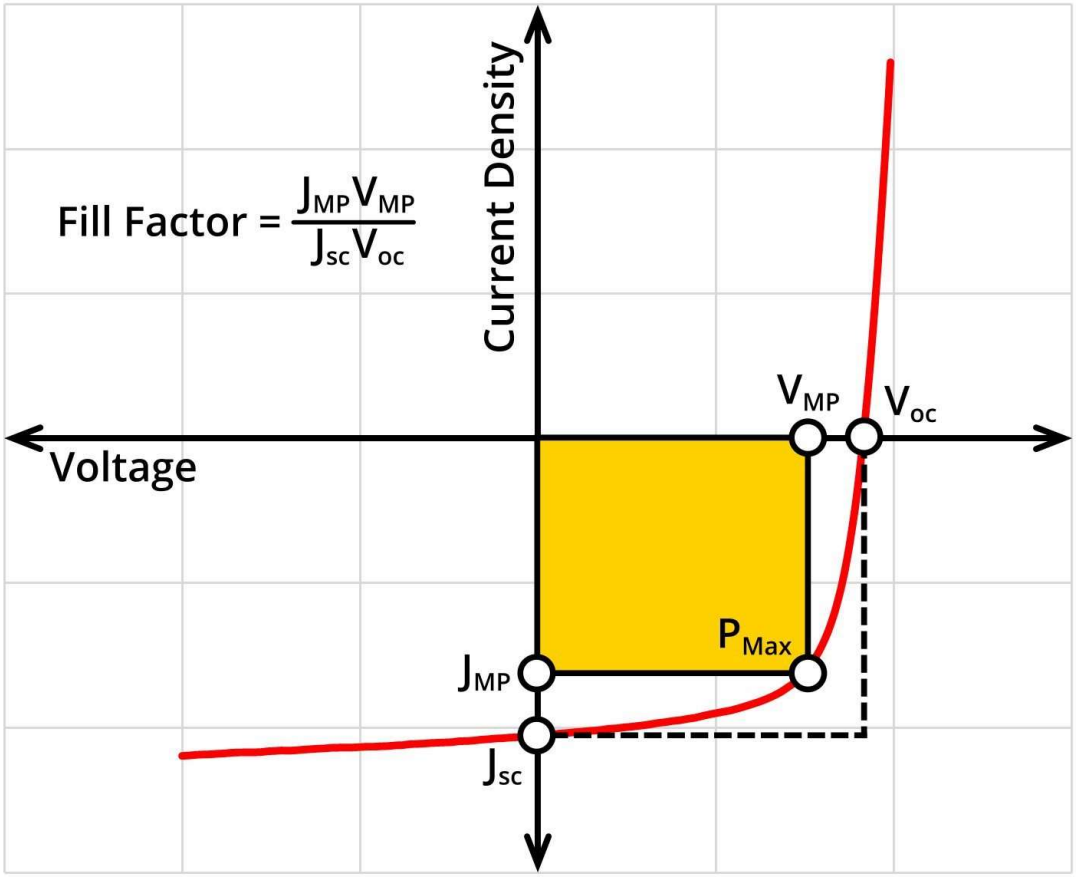

Figure 6.2. Typical current voltage characteristics of a solar cell under illumination, from reference [6]. Points corresponding to short circuit current, open circuit voltage, maximum power point, and current and voltage at maximum power are plotted. The fill factor is illustrated as the ration of the yellow area to the area outlined by dashed lines.

OPV technology is relatively new, and has seen large increases in performance during recent years (Fig. 6.3).[7] That being said, it still lags considerably in performance compared to inorganic solar cells in typical testing configurations, and has issues with stability. Single layer OPV cells have only recently achieved PCEs of 18%,[134] as compared to silicon solar cells, which have efficiencies up to 26.7%, and even higher for GaAs.[135] However, OPVs do show promise under indoor low light conditions, exhibiting PCEs of up to 28%, surpassing silicon and comparable to GaAs under the same conditions.[136] This shows particular promise for small, low power consumption electronic devices, which make up a large part of the growing "internet of things" (IoT).[136]

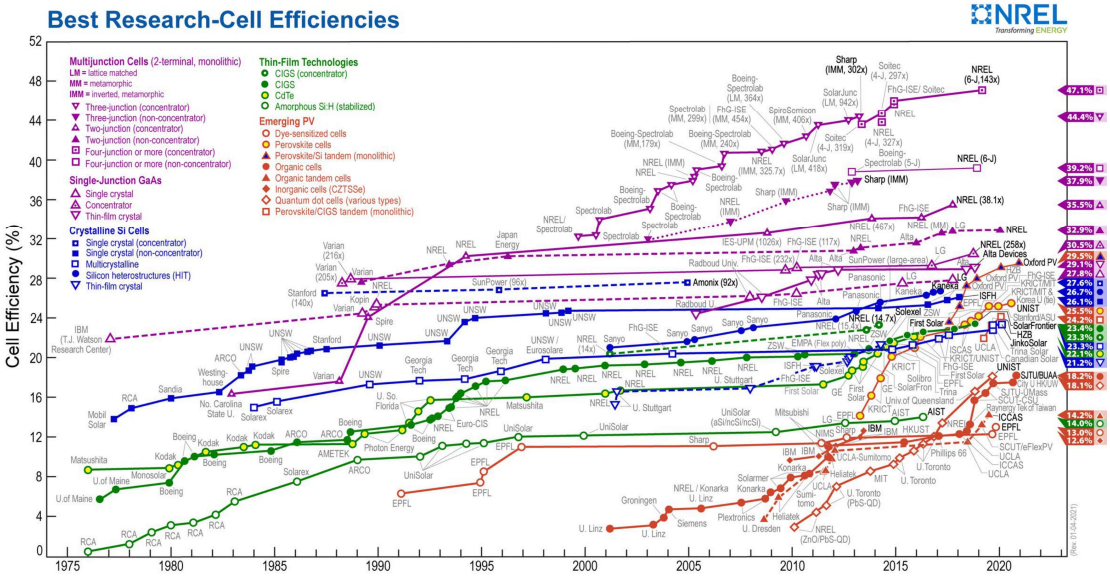

Figure 6.3. Solar cell efficiency records by technology from the National Renewable Energy Lab.[7] Organic solar cells are plotted with solid red circles.

OFETs and OPVs are both very active areas of research with continued progress in device performances, though there are many other types of devices that employ organic semiconductors as well. This chapter details some of the efforts to utilize xylindein in OFETs, organic solar cells, and more.

6.2 Materials and Methods

6.2.1 Materials

Xylindein was extracted and processed as described in previous chapters and publications. ITO coated slides were purchased from Delta Technologies. Poly(3,4-ethylenedioxythiophene) polystyrene sulfonate (PEDOT:PSS) was purchased from Polysciences Inc. PTB7-Th was purchased from California Organic Semiconductor Inc. $PC_{60}BM$ was purchased from Nano-c. All purchased chemicals were used as is without further purification.

6.2.2 Solar Cell Fabrication

Both conventional and inverted structure solar cells were fabricated starting with glass substrates precoated with indium tin oxide (ITO). For conventional cells, ITO coated glass substrates were cleaned with acetone, IPA, and DI-Water. The substrate was then exposed to a UV plasma treatment (Plasma Etch PE-50) at 50W for 5 minutes prior to spin coating a layer of poly(3,4-ethylenedioxythiophene) polystyrene sulfonate (PEDOT:PSS). The active layer was then spin coated on and top Al electrodes were deposited through a shadow mask in a dot pattern via thermal evaporation (Veeco 7700). For inverted geometry solar cells, ITO coated glass substrates were cleaned and a 30nm layer of ZnO was added via sputter deposition (AJA Orion 5). The active layer was spin coated on and top Au electrodes were deposited through a shadow mask in a dot pattern via thermal evaporation (Veeco 7700). Active layer blends were mixed with a magnetic stirrer overnight before spin coating.

6.2.3 Transistor fabrication

Several organic field effect transistor (OFET) geometries were explored. Bottom gate bottom contact (BGBC) devices were fabricated from silicon substrates with a 100 nm thermally oxidized dielectric layer. Au source and drain electrodes were patterned with conventional lift-off photolithography and deposited via thermal evaporation

(Veeco 7700). Xylindein was either spun or drop cast onto the transistor structure. More BGBC devices were fabricated using patterned aluminum gate electrodes thermally deposited on glass, and an anodized aluminum oxide (AlOx) dielectric layer. Source and drain electrodes were thermally evaporated through a shadow mask and xylindein was deposited on top. A few other structures were also attempted, but are not listed for brevity.

Organic electrochemical transistors (OECTs) and water gated transistors were constructed from Au interdigitated electrodes thermally evaporated onto glass substrates, patterned with conventional lift-off photolithography. Either poly(3,4-ethylenedioxythiophene) polystyrene sulfonate (PEDOT:PSS) or xylindein was spun or drop casted onto the electrodes and a drop of 0.1M NaCl or DI-water was carefully placed on the center of the device. An Ag/AgCl pellet served as the gate electrode.

6.3 Results and Discussion

6.3.1 Organic Solar Cells

Xylindein was investigated as a non-fullerene acceptor material in various solar cell geometries. Initial studies explored potential D/A blends of xylindein with other materials, looking for signs of charge transfer. No clear signs of charge transfer states were observed spectroscopically in blends with P3HT, ADT-TES-F, PTB7-Th, or $PC_{60}BM$. Thin films of these blends were deposited onto glass substrates with patterned Au electrodes to measure photoconductivity. Blends of P3HT:Xylindein and ADT:Xylindein were less photoconductive than pristine P3HT and ADT respectively. A film composed of a PTB7-Th:Xylindein blend had a higher photosensitivity (defined as the ratio of photocurrent to dark current) than either pristine PTB7-Th or pristine Xylindein (Fig. 6.4). This blend was thus chosen to be further investigated in solar cell devices as the active layer.

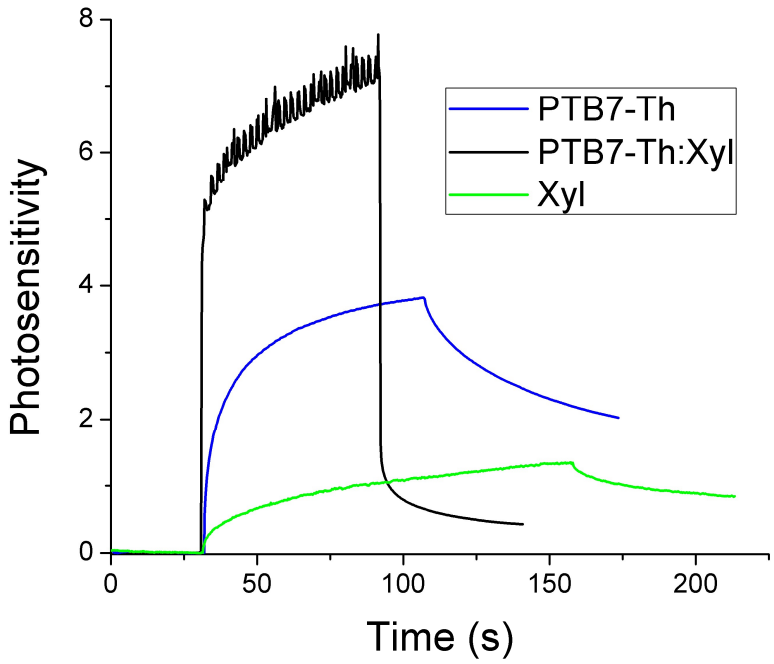

Figure 6.4. Photosensitivity of thin films of PTB7-Th, Xylindein, and a 1:1 w/w blend of each dropcast onto interdigitated Au electrodes on glass. The blend shows an increase in photosensitivity with respect to the pristine materials, indicating potential as a D/A blend in solar cells.

Several solar cell geometries were explored to create benchmark devices to compare to. Conventional geometry solar cells were constructed with ITO coated glass as an anode, PEDOT:PSS as a hole transport layer, and aluminum as a low work function top electrode. Deposition processes for low work function materials such as LiF or Ca typically used as electron transport layers were not readily available and device performance was sub-optimal because of this. Inverted geometry cells were then fabricated using ITO coated glass substrates as a bottom electrode and sputtered ZnO as an electron transport layer and Au as a high work function top electrode. These devices exhibited better performance, though could be improved further with a suitable high work function hole transport layer such as MoO_3.

Figure 6.5 shows current voltage characteristics of solar cells under illumination from a solar simulator with PTB7-Th as a donor material. The benchmark cell with $PC_{60}BM$ shows modest performance with $J_{SC} \approx 6$ mA/cm^2 and $V_{OC} \approx 0.4$V. Pristine

PTB7-Th, for comparison, exhibits a short circuit current density of <1 mA/cm^2 and V_{OC}≈ 0.1V. Solar cells with xylindein as an acceptor material have a negligible short circuit current and open circuit voltage. In contrast to the initial photosensitivity measurement, xylindein is found to be detrimental to performance in this configuration.

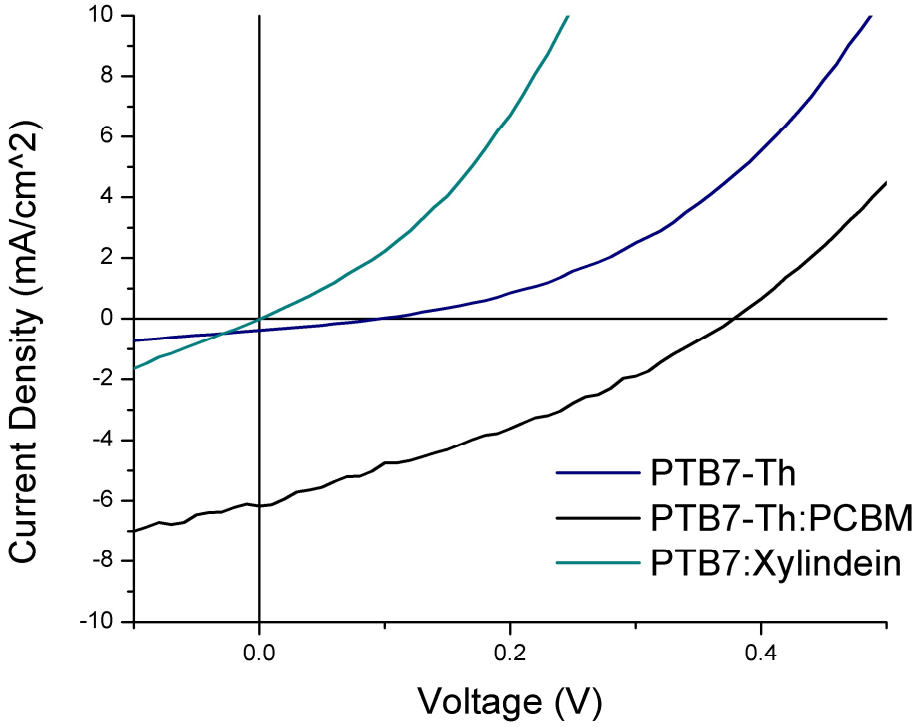

Figure 6.5. I-V curves for organic solar cells under illumination from a solar simulator with PTB7-Th as a donor material. D/A blend of PTB7-Th/xylindein performs well below benchmark D/A blend PTB7-Th/$PC_{60}BM$ and worse than donor only solar cells.

In order to investigate the cause of this poor performance in the solar cell with xylindein, ternary blend solar cells were fabricated with PTB7-Th and $PC_{60}BM$ and small amounts of xylindein. Figure 6.6 shows current voltage characteristics for ternary blend solar cells under illumination from a solar simulator with 0-5 % xylindein.

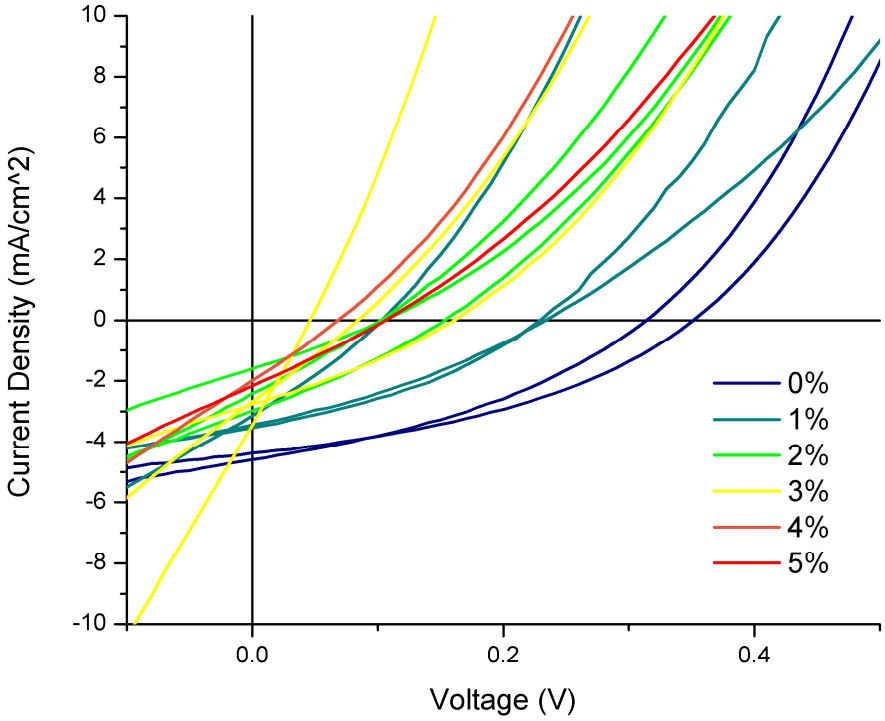

Figure 6.6. Current voltage characteristics for PTB7-Th:$PC_{60}BM$:xylindein 1:1:0-5% ternary blend solar cells under illumination from a solar simulator. Total irradiance was ~100mW/cm^2.

Even small amounts of xylindein result in a significant decrease in performance, reducing both J_{SC} and V_{OC}. One reason for this could be the short exciton lifetime of xylindein films. Diffusion length is directly related to exciton lifetime through equation 6.4:

$$L_D = \sqrt{D\tau} \tag{6.4}$$

Here L_D is the diffusion length, D is the diffusion coefficient, and τ is the exciton lifetime. While in a coplanar geometry the applied voltage may be enough to quickly dissociate the excitons and induce a photocurrent, the small built-in potential of a solar cell may not be enough to efficiently dissociate excitons to extract charge. In this way the xylindein would act as a trap for excitons, recombining them and thus

hindering device performance. Furthermore, the most dominant excited state relaxation pathway occurs through ESIPT (Ch. 5), and any fluorescence radiated after this transition would be too low in energy to be reabsorbed and harvested as current. Morphology may also play a role, as the poor solubility of xylindein can lead to inhomogeneities in thin films. With these results, xylindein was not deemed a viable acceptor material in BHJ solar cells.

6.3.2 Transistors

Performance of n-type OFETs currently lags behind p-type transistors, and stable n-type materials are rare. The high stability and decent effective electron mobility along make xylindein an attractive candidate for an n-type OFET material. Xylindein was tested in various geometries with several different dielectric materials, though minimal switching behavior was observed. The poor solubility of xylindein makes it very difficult to use solution deposition methods to create films that are thin and uniform enough for a field effect to be observed. It has been shown in other naturally derived hydrogen bonded pigments that the dielectric material and purity of the pigment have a large influence on device performance.[137,138] In particular, hydrogen bonded materials can only exhibit maximal field effect on highly non-polar, aliphatic dielectric material.[138] Vacuum deposition processes, which are unfortunately not currently available for xylindein, are currently used to deposit hydrogen bonded materials in OFETs due to the poor solubility and hydrophobic nature of a suitable dielectric material. If xylindein were to be thoroughly purified and vacuum deposited on a suitable dielectric, it would be interesting to see the device performance.

There are applications in which film quality is less critical. In investigating more hydrogen bonded pigments and their applications, it was seen that melanin, another hydroxyl containing naturally occurring pigment molecule, is known to exhibit protonic conductivity.[139] One signature of this is that the conductivity of melanin increased drastically with humidity.[139] It was found that films of xylindein also increase in conductivity in the presence of moisture, indicating xylindein too exhibits

protonic conductivity, facilitated by the hydroxyl groups. This protonic conduction is a form of ionic conduction. Materials that have significant ionic and electronic conduction have a number of different applications, and a few have so far been investigated for xylindein.

One device application for organic mixed conductors is an organic electrochemical transistor (OECT). OECTs have a similar geometry to OFETs, except that the solid dielectric layer is replaced by an electrolytic solution (Fig 6.7 (b)). As a benchmark to compare to xylindein and ensure proper fabrication and measurement, poly(3,4-ethylenedioxythiophene) polystyrene sulfonate (PEDOT:PSS) OECTs were fabricated. PEDOT:PSS is a conductive polymer mixture that is the most widely used and one of the best performing active materials in OECTs.[140] Figure 6.7 (a) shows output characteristics of a PEDOT:PSS OECT in a conventional geometry using a 0.1M NaCl solution as the electrolyte and an Ag/AgCl gate electrode. Unlike typical OFETs, PEDOT:PSS OECTs operate in depletion mode, where the device is in an on state when there is no gate bias applied, and an off state when positive voltage is applied. The switching behavior is due to ions from the electrolyte penetrating into the polymer film doping the film. In the case of PEDOT:PSS, which is already p-doped with sulfonate anions from the PSS, the applied voltage causes cations to penetrate into the film, negating the doping effects of PSS and decreasing the conductivity of the film.[140]

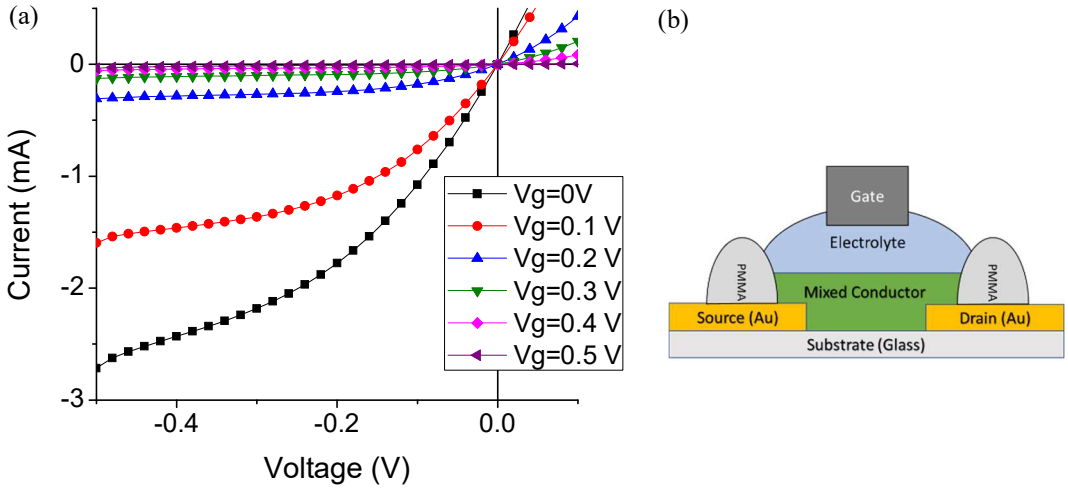

Figure 6.7. (a) Output curves of a PEDOT:PSS OECT. (b) Drawing of OECT configuration.

Xylindein was tested in the same OECT geometry as PEDOT:PSS. Some switching behavior was initially observed, but upon further testing it became evident that the output curves were not characteristic of a properly functioning OECT. Figure 6.8 shows output curves of a xylindein film in an OECT geometry. The large hysteresis and peaks present in the data are features characteristic of cyclic voltammetry data and not transistor output curves. These features are evidence of redox activity in the material as the dominant factor affecting the measurement.

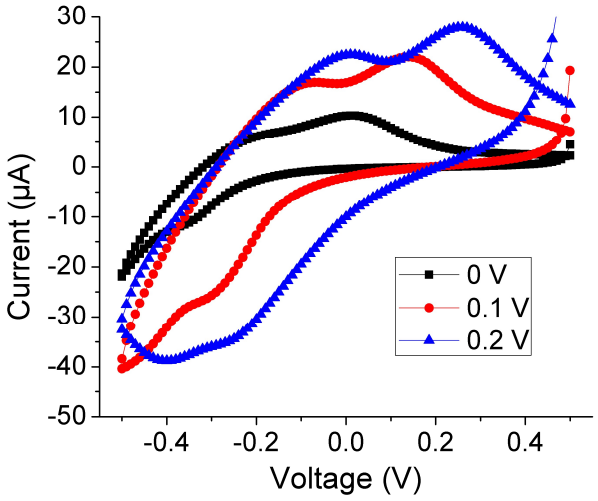

Figure 6.8. Output curves from a xylindein device in an OECT configuration with NaCl solution as electrolyte. The resulting curves are closer to cyclic voltammetry than of a properly functioning transistor.

Another class of transistors similar to the OECT is the water gated organic field effect transistor (WGOFET). The configuration of a WGOFET is essentially the same as an OECT, except that DI-water is used in place of an electrolyte solution. Dissolved ions in the water from exposure to air form an electronic double layer when voltage is applied and a field effect occurs in the material.[141–143] Thus, the working mechanism is closer to that of an OFET than of an OECT. P3HT is a material that has been commonly investigated for WGOFETs. Transconductance values are generally in the range of μA/V[142], though this does depend on geometry. Both OECTs and WGOFETs have applications in biotechnology such as biosensors and neuromorphic devices.[140,144] Xylindein is particularly suited to these applications due to its non-toxicity.

Several different solutions were tested for xylindein devices as a gating medium after initially testing with NaCl in a typical OECT configuration. When DI-water was used, an n-type response was observed (Figure 6.9). Transconductance values are on the order of μA/V, comparable to other WGOFET devices.[142,143] However, the response time for switching behavior in this device was notably slow, on the order of minutes. This would be highly unexpected for an electronic response such as a field effect, and still many times slower than the response of a typical OECT. The working mechanism of this device is potentially different than a FET or an OECT and requires further investigation.

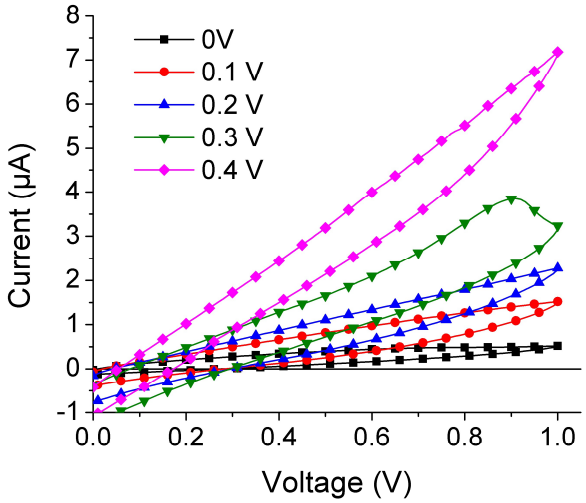

Figure 6.9 Output curves from a xylindein water gated transistor.

The redox behavior exhibited in xylindein OECT devices may be advantageous in energy storage applications. Several other natural pigments, such as melanin and alizarin, have shown promise in battery applications.[145–147] Quinone molecules have been studied extensively in this application, and xylindein is a quinone derivative. The slow response time in water gated xylindein devices may point to charge being stored in the material, which would of course be advantageous in a battery application. Xylindein tends to form porous films, which may allow ions to penetrate into the film and creates for surface area for electrochemical interactions. Xylindein may thus be of use in energy storage applications.

6.4 Conclusion

Xylindein has proven to have some very favorable properties, such as a high stability, decent charge carrier mobility, and non-toxicity. However, these properties cannot be easily utilized in all applications. Xylindein is unsuitable for organic solar cell applications in large part because of a short exciton lifetime, a primary reason for the stability of the molecule. Poor solubility also makes processing difficult. Because of this, suitable films for OFETs could not be fabricated using solution deposition techniques. This is less of an issue for electrochemical applications. Functional water

gated transistors were fabricated, although device response is slow and the exact physical mechanisms behind operation are yet to be fully elucidated. Redox activity observed in some electrochemical transistor curves indicate that xylindein may be useful in battery applications as well. There are many other potential device applications that are yet to be explored. Similar molecules have been explored for use in fuel cell photocatalysis[148] and as molecular switches[149]. Potential bioelectronic applications include biosensors, analytical/diagnostic devices, and neural interfaces.[150] Further research is needed to fully harness xylindein's desirable properties.

Chapter 7: Polaritonic Devices

7.1 Introduction

Polaritons are quasiparticles formed from photons strongly coupled with an electronic or magnetic dipole-carrying excitation, such as an exciton. Strong coupling occurs when the coupling rate of the excitation to the photon is faster than any dissipation. Exciton polaritons can be formed by placing a suitable material inside an optical cavity where the resonant energy of the cavity aligns with the exciton energy of the material. Under these conditions, the excitonic energy is split into two hybridized energy states, the upper polariton (UP) and the lower polariton (LP). The degree of coupling can be quantified by the minimum separation between the two polariton branches in the dispersion curve, known as the Rabi splitting energy ($\hbar\Omega_R$).

$$\hbar\Omega_R = 2\sqrt{\frac{\hbar\omega_c}{\epsilon_0 V}}\mu\sqrt{n_{ph}+1} \tag{7.1}$$

Here $\hbar\omega_c$ is the cavity resonance, ϵ_0 is the vacuum permittivity, V is the mode volume, μ is the transition dipole moment, and n_{ph} is the number of photons in the cavity mode. It is interesting to note that even when n_{ph} is equal to zero and there is no light incident on the cavity, the splitting is non zero.

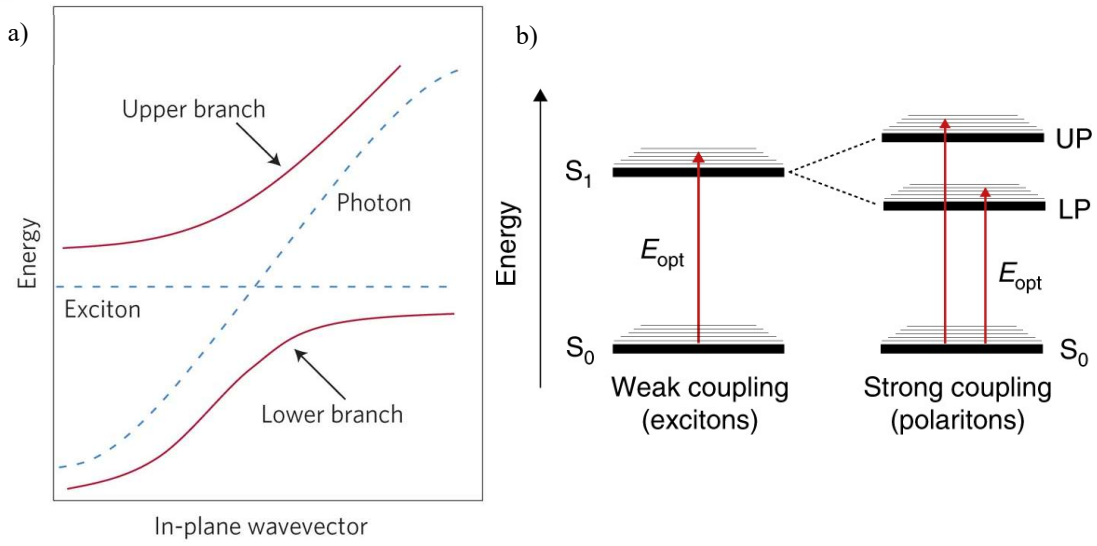

Figure 7.1. (a) Typical polariton dispersion curve for a single excitonic state. From reference [8]. (b) Energy diagram showing the first singlet exciton excited state (S_1) splitting into to polariton states. Red arrows denote electronic transitions from the ground state. From reference [9].

Polaritons in organic materials exhibit some very interesting physical phenomena. Bose-Einstein condensation, for example, has been demonstrated for exciton polaritons at room temperature.[151] There have been several theoretical studies detailing properties of polaritons that may be favorable in electronic applications. It has been demonstrated that microcavity induced polaritonic states can increase the coherence length of the exciton, leading to ballistic transport and potentially increasing organic electronic device performance.[31] Increases in charge transfer[152] and conductance[32] have also been predicted theoretically. There have recently been several attempts at utilizing these favorable characteristics to boost performance in devices. Strong coupling has been exploited to reduce energy losses in organic solar cells, for example.[9] In 2015, Orgiu et al. succeeded in fabricating organic field effect transistors with periodic hole arrays to form plasmon polariton states, and observed an increase in conductivity as compared to a reference device.[153] In 2017, Held et al. fabricated light emitting field effect transistors combined with an optical cavity with no apparent charge transport effects from the presence of the cavity induced exciton-polariton states.[154] Recently in 2021, Kang et al. published results of charge transport

in transistors coupled to optical cavities as well, with no clear effects on electron or hole mobilities.[155] Thus, there is some contention on the effects of polaritons in the electrical characteristics of an organic field effect transistor.

This chapter details efforts to measure the effects of cavity induced exciton-polariton states in organic field effect transistors using 2,8-Difluoro-5,11-bis(triethylsilylethynyl)anthradithiophene (diF-TES-ADT) as an active material. diF-TES-ADT is a well-studied material in the field of organic electronics, and has been shown to exhibit high charge carrier mobility values up to 20 $cm^2V^{-1}s^{-1}$.[156] Furthermore, our lab has demonstrated strong coupling in optical cavities with Rabi splitting of up to 340 meV.[157] This makes diF-TES-ADT an excellent candidate for polariton field effect transistors. This work deviates from the previous work on cavity coupled transistors[154,155] in that these optical cavities are thinner in order to be tuned to the fundamental cavity mode, and phototransistor operation is explored.

7.2 Materials and methods

7.2.1 Transistor fabrication

Transistors were fabricated on glass substrates. First, the substrate was cleaned by sonicating for 5 minutes in a bath of acetone, then rinsed and sonicated in a bath of isopropyl alcohol (IPA) for 5 minutes and subsequently rinsed with IPA and dried with clean compressed air. The substrate was further cleaned with a UV-plasma (Plasma Etch PE-50) treatment at 50 W for 5 minutes. 200 nm of aluminum was thermally evaporated (Veeco 7700) through a shadow mask to form the patterned gate electrode. The aluminum was anodized in a bath of 1mM/10mM citric acid/sodium citrate at a constant current of 2mA followed by a constant voltage, which varied depending on the desired thickness. The relative concentration of citric acid and sodium citrate was chosen to achieve an optimal pH of 6 for the formation of non-porous barrier type aluminum oxide. Films anodized at various voltages were fabricated separately and measured with an ellipsometer (V-VASE J.A. Woollam) to

determine a film thickness that varied linearly with respect to applied voltage of ~1.25/V. After anodization, substrates were rinsed with DI water and dried on a hotplate at 100 °C for 5 minutes. A 20 mg/ml solution of diF-TES-ADT was then spin-coated at 2000 rpm. 40 nm of Au was thermally evaporated (Veeco 7700) onto the diF-TES-ADT through a shadow mask film to form source drain electrodes in a top contact configuration. The channel width of the transistors was 1mm, and channels lengths were 30, 40, 50, 60, and 80 µm. The top insulating layer was deposited on the devices using a gentle atomic layer deposition (ALD) process using trimethylaluminum (TMA) as a precursor and water as an oxidizer. ALD was conducted at 100 °C with 450 cycles for a film thickness of ~45 nm. 10 nm Al top mirrors were deposited via thermal evaporation (Veeco 7700) through a shadow mask on some rows of the devices, leaving the rest as control devices (see Fig. 7.2).

(a) (b)

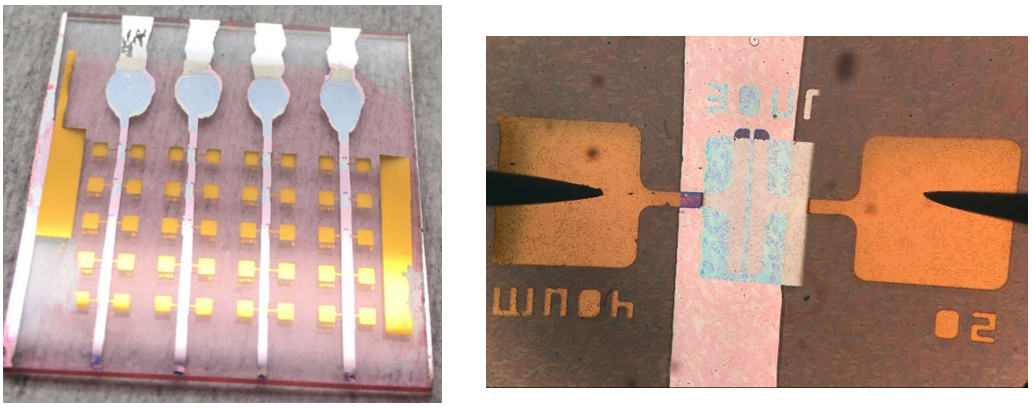

Figure 7.2. (a) A set of completed transistors, with the top three rows including a semitransparent top mirror to complete the optical cavity. (b) A closeup of a single cavity transistor.

7.2.2 Measurements

Reflection measurements were taken on an inverted microscope setup (Olympus IX-71) with a fiber coupled Ocean Optics USB2000 UV-VIS spectrometer. The white

light source (LS-1, Ocean Optics) was connected with a fiber optic cable to a home-built setup to collimate the light and focus it onto the sample at normal incidence.

Transistor measurements were taken on an Alessi REL-4800 probe station with an Agilent 4155C semiconductor analyzer. Output and transfer curves were measured in the dark and under illumination from the built-in white light source from the microscope in the probe station in order to measure photo characteristics.

Photocurrent time series measurements were taken with a Keithley 237 source-measurement unit on a home-built probe station setup. Samples were illuminated with either a 532 nm laser ($Nd:YVO_4$ from Coherent, Inc.) or a 633 nm HeNe laser, both operating in continuous wave (cw) mode at ~1 mW/mm^2 (Fig. 7.3).

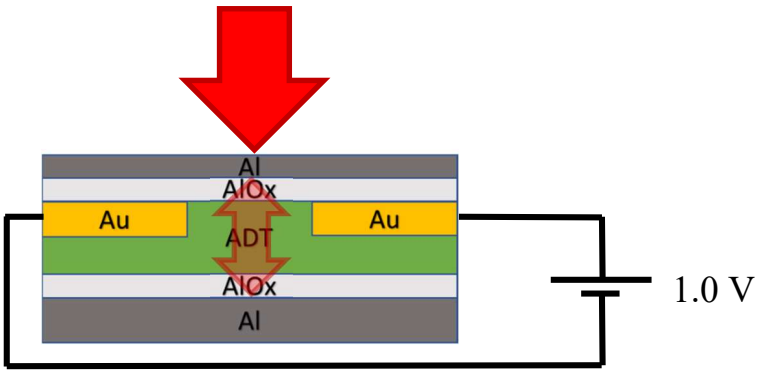

Figure 7.3. Photocurrent time series experimental setup.

7.3 Results and Discussion

Figure 7.4 shows normal incidence reflectance for the four substrates, corresponding to different thicknesses of the cavity, as well as a control with no top mirror. The thicknesses were chosen to get a range such that the cavity resonance below, at, and above the bare exciton energy at normal incidence. This helps to ensure optical coupling in at least one of the substrates and to study the effects of different ranges of coupling. The control spectrum in black shows a reflectance that corresponds directly

to the absorption of a pristine ADT polycrystalline film, with a primary peak at ~550nm corresponding to the S_0-S_1 transition. The secondary peaks correspond to the S_0-S_1 transition coupled to vibrational modes in the molecule. The first set of transistors, labeled “TFT1” and in red on the graph, is the thinnest cavity structure and shows a reflectance dip at ~470nm, below the wavelength of the bare exciton. Minimal coupling is expected in this set due to that difference. The next set (TFT2 in blue) appears to have the cavity tuned near 550 nm to observe splitting at normal incidence. The ~550nm dip of the bare ADT film is split into two dips at ~535nm and ~590nm, corresponding to the upper and lower polariton branches respectively. The next sets (TFT3 and TFT4 in dark cyan and magenta) both appear to have cavity resonances at wavelengths somewhat above the optimal range to observe splitting at normal incidence, with dips at ~620nm and ~660nm. Rabi splitting is at a maximum where the excitonic and photonic energies would cross on a dispersion curve (see Fig. 7.1). Outside of this region, the two polariton branches become more exciton like and more photon like in nature. There may still be some coupling and polariton nature in these sets as the secondary peaks are still slightly shifted form the bare exciton, at ~540nm and ~545nm. It may be of particular interest to tune the cavity at a wavelength just above the bare exciton energy as with these two sets in order to extend the photoresponsive range in a phototransistor application. This will likely rely on some degree of coupling for the more photonic like cavity like branch to be converted into current.

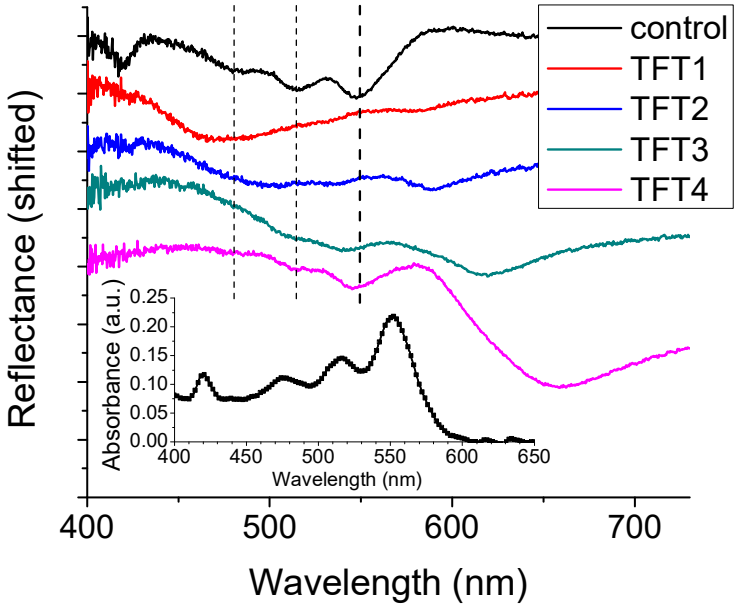

Figure 7.4. Normal incidence reflection curves from cavity structures in each set of transistors, as well as a control device. Each set of transistors has a different cavity thickness, spanning a range around the bare exciton energies (dashed lines). Inset shows ADT absorption spectrum for reference. Inset data was taken by Andrew Platt.

Table 7.1. Transistor sets with cavity resonances

Transistor Set:	TFT1	TFT2	TFT3	TFT4
Normal Incidence Resonance:	470 nm	550 nm	620 nm	660 nm

There have been theoretical studies showing that polariton states can induce charge transfer rates[152] and exciton conductance,[32] so we may expect there to be an increase in the measured mobility and photocurrent in the second set of transistors (TFT2) and maybe the third (TFT3). However, this does not appear to be the case. Figure 7.5 shows saturation charge carrier mobilities (a) and photocurrent (b) for each set of transistors, corresponding to different thicknesses of the cavity structure. There are some trends between the sets of transistors, which is not surprising they have different dielectric thicknesses. There does not, however, seem to be any clear enhancement in the charge carrier mobility or the photocurrent in the cavity devices. It is important to

note that only roughly 25% of the incident light transmits through the top mirror for photocurrent measurements, however. The lack on enhancement in mobility was recently corroborated by Kang et al. who made very similar devices using phthalocyanine as an active material.[155] They also came up with several explanations for why there was no enhancement. One particular reason stated in that work is that excitons (and exciton-polaritons) have a net neutral charge, thus the polaritonic states may not respond to an external electric field.[155] Another possible reason may be that the cavity is structured such that the direction of resonant light waves (vertical in these devices) is orthogonal to the applied electric field. It is interesting to note that of all the transistor sets, the fourth shows the most evidence of mobility enhancement in the cavity structures, though not necessarily in the photocurrent measured with normal incident light. This cavity is tuned in such a way that there would be little coupling at normal incidence, but may achieve some coupling at high angles where there is a component in the same direction as the applied electric field. Further investigation is needed to find if any conditions will result in enhanced charge carrier mobility. Angular dependent photocurrent measurements may help confirm this hypothesis. A vertical field effect transistor may still be a viable geometry for this effect at normal incidence.

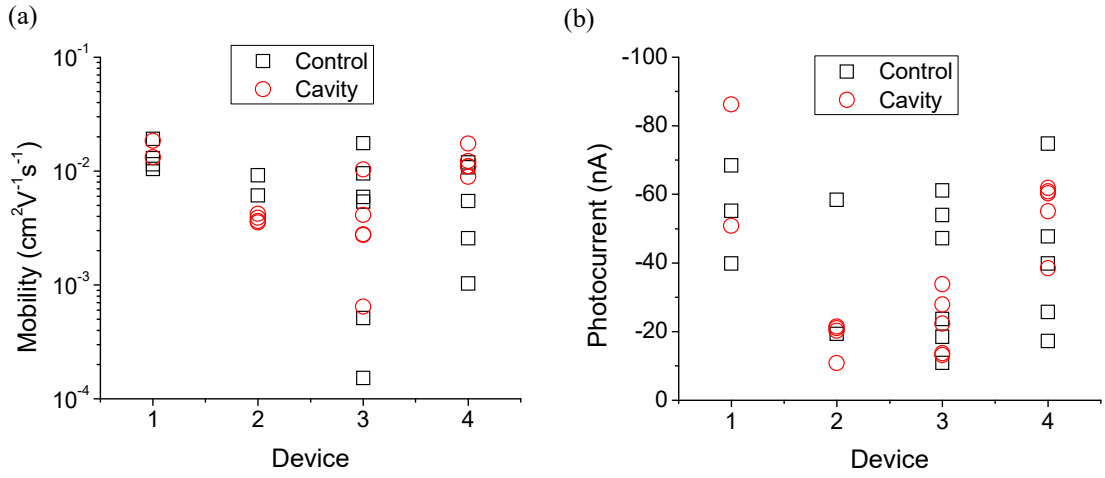

Figure 7.5. (a) Hole mobility values for transistors in each set (device numbers correspond to those in Table 7.1), with control devices labeled with black squares and cavity devices labeled with red circles. Mobility values are extracted from the slope

of the square root of the drain current from the transfer curves. (b) Photocurrent for transistors in each set, with control devices labeled with black squares and cavity devices labeled with red circles. Photocurrent was extracted from output curves at 3V source drain and 3V gate, in the dark and under illumination from a white light source in the probe station setup.

Even without an enhancement in charge carrier mobility or photocurrent levels, there may still be some utility to the cavity structure in extending the photoresponsive wavelength range in phototransistor operation. There is also a question whether an incoherent or coherent light source makes a difference in the level of photocurrent. To investigate this, photocurrent measurements were taken with normally incident laser sources. Figure 7.6 shows photocurrents in ungated devices from illumination by cw 532 nm and 633 nm lasers. Figure 7.6 (a), (b), (c), and (d) correspond to transistor sets 1,2,3, and 4 respectively, in order of increasing cavity thickness. The cavity device in the second set shows a clear decrease in the photocurrent for both wavelengths, indicating that coherent light is not a discerning factor for photocurrent enhancement in these structures. The third set shows a small increase in the photocurrent for both wavelengths, and the fourth shows a slightly larger increase for both wavelengths. This is especially promising given the attenuation of light incident upon the cavity, and the top mirror thickness could be optimized. The increase in 633 nm photocurrent shows that the photosensitive range may be extended, though the 532 nm is also larger, and may be within the range of sample-to-sample variation. Further investigation is needed for a definitive increase in the photoresponse from red light.

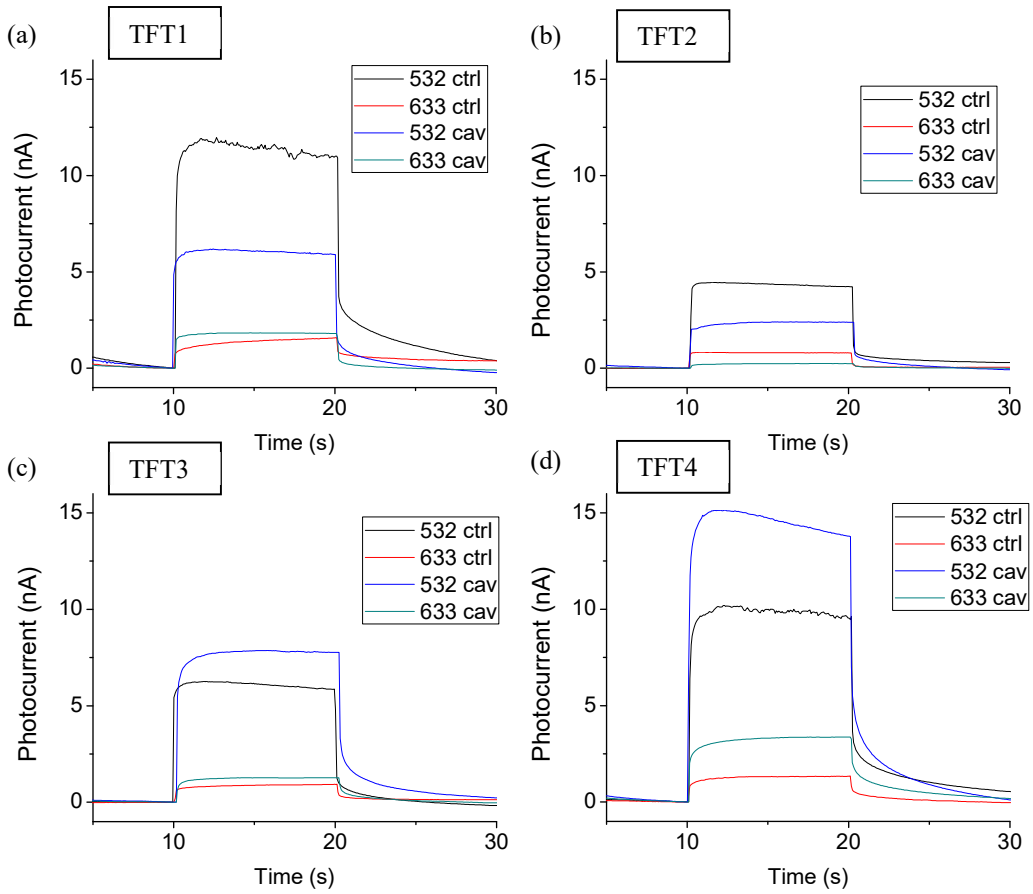

Figure 7.6. Photocurrent time series measurements for cavity and control samples in each set of transistors. (a), (b), (c), and (d) correspond to sets 1,2,3 and 4 respectively. TFT1 is tuned below the exciton wavelength, TFT2 near it, and TFT3 and TFT4 above (Table 7.1). The gate was left unbiased and 1V was applied between source and drain electrodes. The sample was illuminated with 532 nm or 633 nm cw laser light at t=10 s.

7.4 Conclusion

Polaritons have been shown to have unique physical properties that have the potential to increase the performance of organic (opto)electronic devices. Despite theoretical studies on enhancement of charge transport properties[32,152] and an experimental result of enhanced field effect mobility using plasmonic structures,[153] no clear mobility enhancement was seen in optical cavity transistor devices. This in agreement with the recent findings of Kang et al.[155] It is proposed that this may be geometry related, as the cavity structure is orthogonal to the direction of charge transport. There may be

some evidence in this as the thickest cavity transistor set, which is detuned at normal incidence but may couple at higher angles of incidence, has the best mobility relative to control devices. There is also no clear enhancement in photocurrent at normal incidence, though some evidence is put forth that the cavity structure can be used to expand the photosensitive spectral range in a phototransistor.

Chapter 8: Summary and Outlook

This work comprises a comprehensive study of the optical and electronic properties of the fungi-derived pigment xylindein and its (opto)electronic device applications, as well as investigation of effects of exciton polaritons on performance of anthradithiophene field effect transistors. A brief introduction to organic semiconductors and organic (opto)electronic devices was provided. The current market and weaknesses for organic devices along with strategies to mitigate those weaknesses was discussed. This work has focused primarily on the fungi-derived pigment xylindein to learn from and potentially utilize its favorable properties in order to address the current bottlenecks for commercial viability in organic semiconductor devices. Ch. 7 considered polaritonics-based approaches to address some of these issues.

In Ch. 2, xylindein is introduced and basic optical and electronic properties of the fungi derived pigment xylindein are explored. Optical absorption measurements reveal aggregate formation, manifested via an appearance of a ~720 nm absorption band, red-shifted from the spectra of dilute solutions, in solutions with higher concentrations and in films as compared to dilute solutions. The nature of such aggregates that are created by an interplay of intermolecular hydrogen bonding and π-π stacking requires further investigation. Addition of PMMA to pristine xylindein is a promising route to improve the film morphology and solution processability without detriment to the electrical characteristics of the film. Charge carrier (hole) mobilities on the order of 10^{-3} $cm^2/(Vs)$ were obtained both from pristine xylindein and xylindein:PMMA films. A factor of ~2 improvement in photosensitivity was observed in xylindein:PMMA films as compared to pristine xylindein films, due to an enhanced charge generation efficiency caused by an improved film morphology.

Variations in optical and electronic measurements on xylindein from batch to batch led to an effort to minimize and quantify the effects of impurities present. Dramatic effects from an ethanol wash on the optical and electronic properties of the xylindein

solution precursor and xylindein-based thin films, respectively, were observed (Ch. 3). Considerably reduced UV absorption and PL at below 600 nm were obtained in "post-wash" solutions as compared to "pre-wash" solutions. These changes were correlated with a two orders of magnitude enhancement in charge carrier mobility in films drop-cast from "post-wash" solutions as compared to those from "pre-wash" solutions. Mass spectrometry revealed several contributors, hypothesized to be fungal secondary metabolites, responsible for these observations. Removal of these molecules, which serve as contaminants in "pre-wash" xylindein-based devices that disrupt the π-π stacking and hydrogen bonding between xylindein molecules, dramatically increases conductivity of xylindein-based films.

With better protocols for purity in place, a more in-depth study was conducted (Ch. 4). Optical and (opto)electronic properties of xylindein and its blends with PMMA and CNC are presented. Analysis of the optical spectra revealed the presence of two tautomers whose structures and properties were explored using DFT. Propensity for xylindein aggregation depended on the solvent polarity and was strongly pronounced in polar solvents. Aggregates with similar optical properties were observed in films. Excellent photostability was observed in xylindein solutions as compared to those of benchmark organic semiconductor molecules. Electron mobility of up to 0.4 cm^2/Vs was obtained in amorphous films. Both dark and photocurrent were thermally activated with activation energies of 0.3 and 0.2 eV, respectively, in pristine xylindein films. Xylindein blends with PMMA exhibited (opto)electronic performance comparable to that of pristine xylindein films. In xylindein blends with CNC, both dark and photocurrents were at least an order of magnitude lower than in pristine xylindein films. In both blends, the charge transport activation energies were lower (0.25 eV) than in pristine xylindein films due to a smoother film morphology as revealed by the SEM.

In order to better understand the relationship between xylindein's molecular structure and its properties, we compared optical and (opto)electronic properties of xylindein with its methylated derivative, dimethylxylindein via an integrated platform from

wood sciences, organic synthesis, ultrafast spectroscopy, quantum chemistry calculations, to device physics (Ch. 5). The hydroxyl groups in xylindein, which are not present in dimethylxylindein, were found to play a critical role in optical absorption and PL properties, excited state dynamics, photostability, and conductivity. Enhanced photostability of xylindein is attributed to fast deactivation of the excited state; this channel is not as efficient in dimethylxylindein with a long-lived dark (triplet) state formation being observed instead, which considerably reduces its photostability. At room temperature, amorphous xylindein films were found to be over four orders of magnitude more conductive than both amorphous and crystalline dimethylxylindein films. On the other hand, the photosensitivity of dimethylxylindein films is considerably higher than that of xylindein films, attributed to higher photogeneration efficiency in dimethylxylindein. Charge transport was thermally activated in all films under study, with the activation energies considerably lower in xylindein films as compared to dimethylxylindein films. The observed large difference in electronic properties is partly attributed to H-bonding in xylindein which promotes morphology supportive of efficient conductive network in xylindein films and reduces the average charge trap depth.

Device applications were explored in Ch. 6. Xylindein has proven to have some very favorable properties, such as a high stability, decent charge carrier mobility, and non-toxicity. However, these properties cannot be easily utilized in all applications. Xylindein was found to be unsuitable for organic solar cell applications in large part because of a short exciton lifetime, a primary reason for the stability of the molecule. Poor solubility also makes processing difficult. Because of this, suitable films for OFETs could not be fabricated using solution deposition techniques. This is less of an issue for certain electrochemical applications. Functional water gated transistors were fabricated, although device response is slow and the exact physical mechanisms behind operation are yet to be fully elucidated. Redox activity observed in some electrochemical transistor curves indicate that xylindein may be useful in battery applications as well. There are many other potential device applications that are yet to be explored. Similar molecules have been explored for use in fuel cell

photocatalysis[148] and as molecular switches[149]. Potential bioelectronic applications include biosensors, analytical/diagnostic devices, and neural interfaces.[150] Further research is needed to fully harness xylindein's desirable properties.

Field effect transistors are further explored in Ch. 7, using a different strategy to help understand how to overcome current bottlenecks: polaritons. A conventional benchmark organic semiconductor, diF-TES-ADT, is used to study the effects of exciton-polaritons in (opto)electronic devices. Polaritons have been shown to have unique physical properties that have the potential to increase the performance of organic (opto)electronic devices. Despite theoretical studies on enhancement of charge transport properties[32,152] and an experimental result of enhanced field effect mobility using plasmonic structures,[153] no clear mobility enhancement was seen in optical cavity transistor devices. This in agreement with the recent findings of Kang et al.[155] It is proposed that this may be geometry related, as the cavity structure is orthogonal to the direction of charge transport. There may be some evidence in this as the thickest cavity transistor set, which is detuned at normal incidence but may couple at higher angles of incidence, has the best mobility relative to control devices. There is also no clear enhancement in photocurrent at normal incidence, though some evidence is put forth that the cavity structure can be used to expand the photosensitive spectral range in a phototransistor.

Xylindein has been shown to have some very interesting properties. With further processing developments, it may have use as a naturally sourced, sustainable material in organic (opto)electronic devices. One can learn from the molecular features of xylindein to guide the design of next generation organic semiconductors. Hydrogen bonding in particular is a useful mechanism to increase stability and conductivity. Polaritonics may also be a useful mechanism for organic (opto)electronic devices. Enhancements in the spectral range of photosensitive devices are possible, and with the right geometry, enhanced charge transport may still be possible. There is still much work that can be done towards understanding and utilizing both naturally derived pigments as organic semiconductors, and polaritonics in organic

(opto)electronic devices. This work has shown potential for organic semiconductor device developments and guides future research towards continued progress.

Bibliography

(1) Nano, A. Towards Optical Memories : Switchable Optical Systems for Electron and Energy Transfer Processes, 2015.

(2) Burdett, J. J.; Müller, A. M.; Gosztola, D.; Bardeen, C. J. Excited State Dynamics in Solid and Monomeric Tetracene: The Roles of Superradiance and Exciton Fission. *J. Chem. Phys.* **2010**, *133* (14). https://doi.org/10.1063/1.3495764.

(3) Baranovskii, S. D. Theoretical Description of Charge Transport in Disordered Organic Semiconductors. *Phys. Status Solidi Basic Res.* **2014**. https://doi.org/10.1002/pssb.201350339.

(4) Gevorgyan, S. A.; Madsen, M. V.; Roth, B.; Corazza, M.; Hösel, M.; Søndergaard, R. R.; Jørgensen, M.; Krebs, F. C. Lifetime of Organic Photovoltaics: Status and Predictions. *Adv. Energy Mater.* **2016**, *6* (2), 1501208. https://doi.org/10.1002/aenm.201501208.

(5) Paterson, A. F.; Singh, S.; Fallon, K. J.; Hodsden, T.; Han, Y.; Schroeder, B. C.; Bronstein, H.; Heeney, M.; McCulloch, I.; Anthopoulos, T. D. Recent Progress in High-Mobility Organic Transistors: A Reality Check. *Adv. Mater.* **2018**, *30* (36), 1801079. https://doi.org/10.1002/adma.201801079.

(6) Oscilla. Solar Cells : A Guide to Theory and Measurement. **2018**, 1–22.

(7) Best Research-Cell Efficiency Chart | Photovoltaic Research | NREL https://www.nrel.gov/pv/cell-efficiency.html (accessed Apr 3, 2021).

(8) Holmes, R. J. Organic Polaritons: Long-Distance Relationships. *Nature Materials*. Nature Publishing Group May 4, 2014, pp 669–670. https://doi.org/10.1038/nmat3986.

(9) Nikolis, V. C.; Mischok, A.; Siegmund, B.; Kublitski, J.; Jia, X.; Benduhn, J.; Hörmann, U.; Neher, D.; Gather, M. C.; Spoltore, D.; Vandewal, K. Strong Light-Matter Coupling for Reduced Photon Energy Losses in Organic Photovoltaics. *Nat. Commun.* **2019**, *10* (1), 1–8. https://doi.org/10.1038/s41467-019-11717-5.

(10) Akamatu, H.; Inokuchi, H. On the Electrical Conductivity of Violanthrone,

Iso-Violanthrone, and Pyranthrone. *J. Chem. Phys.* **1950**, *18* (6), 810–811. https://doi.org/10.1063/1.1747780.

(11) Akamatu, H.; Inokuchi, H.; Matsunaga, Y. Organic Semiconductors with High Conductivity. I. Complexes between Polycyclic Aromatic Hydrocarbons and Halogens. *Bull. Chem. Soc. Jpn.* **1956**, *29* (2), 213–218. https://doi.org/10.1246/bcsj.29.213.

(12) Kallmann, H.; Pope, M. Bulk Conductivity in Organic Crystals. *Nature* **1960**, *186* (4718), 31–33. https://doi.org/10.1038/186031a0.

(13) Shirakawa, H.; Louis, E. J.; MacDiarmid, A. G.; Chiang, C. K.; Heeger, A. J. Synthesis of Electrically Conducting Organic Polymers: Halogen Derivatives of Polyacetylene, (CH)X. *J. Chem. Soc. Chem. Commun.* **1977**, No. 16, 578–580. https://doi.org/10.1039/C39770000578.

(14) Heeger, A. J.; MacDiarmid, A. G.; Shirakawa, H. The Nobel Prize in Chemistry 2000. **2000**, *12* (1974), 11–20.

(15) Gamota, D. R.; Brazis, P.; Kalyanasundaram, K.; Zhang, J. *Printed Organic and Molecular Electronics*; 2004. https://doi.org/10.1007/978-1-4419-9074-7.

(16) Tang, C. W.; Vanslyke, S. A. Organic Electroluminescent Diodes. *Appl. Phys. Lett.* **1987**, *51* (12), 913–915. https://doi.org/10.1063/1.98799.

(17) Tang, C. W. Two-Layer Organic Photovoltaic Cell. *Appl. Phys. Lett.* **1986**, *48* (2), 183–185. https://doi.org/10.1063/1.96937.

(18) Organic Electronics Market Size, Share, Trends, Opportunities & Forecast https://www.kbvresearch.com/organic-electronics-market/ (accessed May 12, 2021).

(19) Bässler, H.; Köhler, A. Charge Transport in Organic Semiconductors. *Top. Curr. Chem.* **2012**, *312* (5), 1–65. https://doi.org/10.1007/128_2011_218.

(20) Lu, N.; Li, L.; Geng, D.; Liu, M. A Review for Polaron Dependent Charge Transport in Organic Semiconductor. *Organic Electronics*. Elsevier B.V. October 1, 2018, pp 223–234. https://doi.org/10.1016/j.orgel.2018.05.053.

(21) Ostroverkhova, O.; Cooke, D. G.; Shcherbyna, S.; Egerton, R. F.; Hegmann, F. A.; Tykwinski, R. R.; Anthony, J. E. Bandlike Transport in Pentacene and Functionalized Pentacene Thin Films Revealed by Subpicosecond Transient

Photoconductivity Measurements. *Phys. Rev. B - Condens. Matter Mater. Phys.* **2005**, *71* (3). https://doi.org/10.1103/PhysRevB.71.035204.

(22) Dong, J.; Wu, C. Crossover from Hopping to Band-like Transport in Crystalline Organic Semiconductors: The Effect of Shallow Traps. *J. Chem. Phys.* **2019**, *150* (4), 44903. https://doi.org/10.1063/1.5066563.

(23) Ostroverkhova, O. *Handbook of Organic Materials for Electronic and Photonic Devices*; 2019. https://doi.org/10.1016/c2016-0-05254-3.

(24) Wasikiewicz, J. M.; Abu-Sen, L.; Horn, A. B.; Koelewijn, J. M.; Parry, A. V. S.; Morrison, J. J.; Yeates, S. G. Towards Solution Processable Air Stable P-Type Organic Semiconductors: Synthesis and Evaluation of Mono and Di-Fluorinated Pentacene Derivatives. *J. Mater. Chem. C* **2016**, *4* (30), 7309–7315. https://doi.org/10.1039/c6tc01221c.

(25) Quinn, J. T. E.; Zhu, J.; Li, X.; Wang, J.; Li, Y. Recent Progress in the Development of N-Type Organic Semiconductors for Organic Field Effect Transistors. *J. Mater. Chem. C* **2017**, *5* (34), 8654–8681. https://doi.org/10.1039/c7tc01680h.

(26) Wang, C.; Zhang, X.; Dong, H.; Chen, X.; Hu, W. Challenges and Emerging Opportunities in High-Mobility and Low-Energy-Consumption Organic Field-Effect Transistors. *Advanced Energy Materials*. Wiley-VCH Verlag August 24, 2020, p 2000955. https://doi.org/10.1002/aenm.202000955.

(27) Paudel, K.; Giesbers, G.; Van Schenck, J.; Anthony, J. E.; Ostroverkhova, O. Molecular Packing-Dependent Photoconductivity in Functionalized Anthradithiophene Crystals. *Org. Electron.* **2019**, *67*, 311–319. https://doi.org/10.1016/j.orgel.2018.12.040.

(28) Van Schenck, J. D. B.; Mayonado, G.; Anthony, J. E.; Graham, M. W.; Ostroverkhova, O. Molecular Packing-Dependent Exciton Dynamics in Functionalized Anthradithiophene Derivatives: From Solutions to Crystals. *J. Chem. Phys.* **2020**, *153* (16), 164715. https://doi.org/10.1063/5.0026072.

(29) Komissarova, E. A.; Dominskiy, D. I.; Zhulanov, V. E.; Abashev, G. G.; Siddiqui, A.; Singh, S. P.; Sosorev, A. Y.; Paraschuk, D. Y. Unraveling the Unusual Effect of Fluorination on Crystal Packing in an Organic

Semiconductor. *Phys. Chem. Chem. Phys.* **2020**, *22* (3), 1665–1673. https://doi.org/10.1039/c9cp05455c.

(30) Giesbers, G.; Krueger, T. D.; Van Schenck, J. D. B.; Kim, R.; Van Court, R. C.; Robinson, S. C.; Beaudry, C. M.; Fang, C.; Ostroverkhova, O. Role of Hydroxyl Groups in the Photophysics, Photostability, and (Opto)Electronic Properties of the Fungi-Derived Pigment Xylindein. *J. Phys. Chem. C* **2021**, *125*, 6545. https://doi.org/10.1021/acs.jpcc.0c09627.

(31) Spano, F. C. Optical Microcavities Enhance the Exciton Coherence Length and Eliminate Vibronic Coupling in J-Aggregates. *J. Chem. Phys.* **2015**, *142* (18), 34109. https://doi.org/10.1063/1.4919348.

(32) Feist, J.; Garcia-Vidal, F. J. Extraordinary Exciton Conductance Induced by Strong Coupling. *Phys. Rev. Lett.* **2015**, *114* (19). https://doi.org/10.1103/PhysRevLett.114.196402.

(33) Irimia-Vladu, M.; Glowacki, E. D.; Sariciftci, N. S.; Bauer, S. Natural Materials for Organic Electronics. In *Small Organic Molecules on Surfaces*; 2013; Vol. 173, pp 295–318. https://doi.org/10.1007/978-3-642-33848-9.

(34) Marrocchi, A.; Facchetti, A.; Lanari, D.; Petrucci, C.; Vaccaro, L. Current Methodologies for a Sustainable Approach to Π-Conjugated Organic Semiconductors. *Energy Environ. Sci.* **2016**, *9*, 763–786. https://doi.org/10.1039/C5EE03727A.

(35) Ostroverkhova, O. Organic Optoelectronic Materials : Mechanisms and Applications. *Chem. Rev.* **2016**. https://doi.org/10.1021/acs.chemrev.6b00127.

(36) Robinson, S. Decay, Discovery, and Artistry – A Journey. *Am. Sci.* **2014**, *102* (3), 206–213.

(37) Robinson, S. C.; Hinsch, E.; Weber, G. Method of Extraction and Resolubilisation of Pigments from Chlorociboria Aeruginosa and Scytalidium Cuboideum, Two Prolific Spalting Fungi. *Color. Technol.* **2014**, *130* (3), 221–225.

(38) Weber, G.; Chen, H. L.; Hinsch, E.; Freitas, S.; Robinson, S. Pigments Extracted from the Wood-Staining Fungi Chlorociboria Aeruginosa, Scytalidium Cuboideum, and S. Ganodermophthorum Show Potential for Use

as Textile Dyes. *Color. Technol.* **2014**, *130* (6), 445–452. https://doi.org/10.1111/cote.12110.

(39) Robinson, S. C.; Tudor, D.; Snider, H.; Cooper, P. A. Stimulating Growth and Xylindein Production of Chlorociboria Aeruginascens in Agar-Based Systems. *AMB Express* **2012**, *2* (1), 15. https://doi.org/10.1186/2191-0855-2-15.

(40) Mei, J.; Diao, Y.; Appleton, A. L.; Fang, L.; Bao, Z. Integrated Materials Design of Organic Semiconductors for Field-Effect Transistors. *J. Am. Chem. Soc.* **2013**, *135*, 6724–6746.

(41) Kobayashi, N.; Sasaki, M.; Nomoto, K. Stable Peri-Xanthenoxanthene Thin-Film Transistors with Efficient Carrier Injection. *Chem. Mater.* **2009**, *21* (3), 552–556. https://doi.org/10.1021/cm802826m.

(42) Yoneya, N.; Ono, H.; Ishii, Y.; Himori, K.; Hirai, N.; Abe, H.; Yumoto, A.; Kobayashi, N.; Nomoto, K. Flexible Electrophoretic Display Driven by Solution-Processed Organic Thin-Film Transistors. *J. Soc. Inf. Disp.* **2012**, *20*, 143–147.

(43) Harrison, R.; Quinn, A.; Weber, G.; Johnson, B.; Rath, J.; Remcho, V.; Robinson, S.; Ostroverkhova, O. Fungi-Derived Pigments as Sustainable Organic (Opto)Electronic Materials. In *SPIE*; 2017; Vol. 10101, p 101101U. https://doi.org/10.1117/12.2251265.

(44) Shepherd, W. E. B.; Platt, A. D.; Hofer, D.; Ostroverkhova, O.; Loth, M.; Anthony, J. E. Aggregate Formation and Its Effect on (Opto)Electronic Properties of Guest-Host Organic Semiconductors. *Appl. Phys. Lett.* **2010**, *97* (16), 163303. https://doi.org/10.1063/1.3505493.

(45) Day, J.; Platt, A. D.; Subramanian, S.; Anthony, J. E.; Ostroverkhova, O. Influence of Organic Semiconductor-Metal Interfaces on the Photoresponse of Functionalized Anthradithiophene Thin Films. *J. Appl. Phys.* **2009**, *105* (10), 1–10. https://doi.org/10.1063/1.3129693.

(46) Platt, A.; Kendrick, M.; Loth, M.; Anthony, J.; Ostroverkhova, O. Temperature Dependence of Exciton and Charge Carrier Dynamics in Organic Thin Films. *Phys. Rev. B* **2011**, *84* (23), 235209. https://doi.org/10.1103/PhysRevB.84.235209.

(47) Sytnyk, M.; Głowacki, E. D.; Yakunin, S.; Voss, G.; Schöfberger, W.; Kriegner, D.; Stangl, J.; Trotta, R.; Gollner, C.; Tollabimazraehno, S.; Romanazzi, G.; Bozkurt, Z.; Havlicek, M.; Sariciftci, N. S.; Heiss, W. Hydrogen-Bonded Organic Semiconductor Micro- and Nanocrystals: From Colloidal Syntheses to (Opto-)Electronic Devices. *J. Am. Chem. Soc.* **2014**, *136* (47), 16522–16532. https://doi.org/10.1021/ja5073965.

(48) Dou, L.; You, J.; Hong, Z.; Xu, Z.; Li, G.; Street, R. A.; Yang, Y. 25th Anniversary Article : A Decade of Organic / Polymeric Photovoltaic Research. *Adv. Mater.* **2013**, 6642–6671. https://doi.org/10.1002/adma.201302563.

(49) Bisquert, J. Effects of Morphology on the Functionality of Organic Electronic Devices. *J. Phys. Chem. Lett.* **2012**, *3* (11), 1515–1516. https://doi.org/10.1021/jz300600j.

(50) Hunter, S.; Chen, J.; Anthopoulos, T. D. Microstructural Control of Charge Transport in Organic Blend Thin-Film Transistors. *Adv. Funct. Mater.* **2014**, *24* (38), 5969–5976. https://doi.org/10.1002/adfm.201401087.

(51) Irimia-Vladu, M. “Green” Electronics: Biodegradable and Biocompatible Materials and Devices for Sustainable Future. *Chemical Society Reviews*. 2014. https://doi.org/10.1039/c3cs60235d.

(52) Irimia-Vladu, M.; Gåowacki, E. D.; Troshin, P. A.; Schwabegger, G.; Leonat, L.; Susarova, D. K.; Krystal, O.; Ullah, M.; Kanbur, Y.; Bodea, M. A.; Razumov, V. F.; Sitter, H.; Bauer, S.; Sariciftci, N. S. Indigo - A Natural Pigment for High Performance Ambipolar Organic Field Effect Transistors and Circuits. *Adv. Mater.* **2012**. https://doi.org/10.1002/adma.201102619.

(53) Głowacki, E. D.; Voss, G.; Leonat, L.; Irimia-Vladu, M.; Bauer, S.; Sariciftci, N. S. Indigo and Tyrian Purple - From Ancient Natural Dyes to Modern Organic Semiconductors. *Israel Journal of Chemistry*. John Wiley & Sons, Ltd June 1, 2012, pp 540–551. https://doi.org/10.1002/ijch.201100130.

(54) Dittmann, M.; Graupner, F. F.; Maerz, B.; Oesterling, S.; Devivie-Riedle, R.; Zinth, W.; Engelhard, M.; Lüttke, W. Photostability of 4,4′-Dihydroxythioindigo, a Mimetic of Indigo. *Angew. Chemie - Int. Ed.* **2014**. https://doi.org/10.1002/anie.201307016.

(55) Głowacki, E. D.; Irimia-Vladu, M.; Bauer, S.; Sariciftci, N. S. Hydrogen-Bonds in Molecular Solids-from Biological Systems to Organic Electronics. *Journal of Materials Chemistry B*. 2013. https://doi.org/10.1039/c3tb20193g.

(56) Giesbers, G.; Van Schenck, J.; Vega Gutierrez, S.; Robinson, S.; Ostroverkhova, O. Fungi-Derived Pigments for Sustainable Organic (Opto)Electronics. In *MRS Advances*; 2018; Vol. 3, pp 3459–3464. https://doi.org/10.1557/adv.2018.446.

(57) Giesbers, G.; Van Schenck, J.; Quinn, A.; Van Court, R.; Vega Gutierrez, S. M.; Robinson, S. C.; Ostroverkhova, O. Xylindein: Naturally Produced Fungal Compound for Sustainable (Opto)Electronics. *ACS Omega* **2019**, *4* (8), 13309–13318. https://doi.org/10.1021/acsomega.9b01490.

(58) Benson, D. A.; Karsch-Mizrachi, I.; Clark, K.; Lipman, D. J.; Ostell, J.; Sayers, E. W. GenBank. *Nucleic Acids Res.* **2012**. https://doi.org/10.1093/nar/gkr1202.

(59) Robinson, S. C.; Gutierrez, S. M. V.; Garcia, R. A. C.; Iroume, N.; Vorland, N. R.; McClelland, A.; Huber, M.; Stanton, S. Potential for Carrying Dyes Derived from Spalting Fungi in Natural Oils. *J. Coatings Technol. Res.* **2017**. https://doi.org/10.1007/s11998-017-9919-4.

(60) Frisch, M. J.; Trucks, G. W.; Schlegel, H. E.; Scuseria, G. E.; Robb, M. A.; Cheeseman, J. R.; Scalmani, G.; Barone, V.; Petersson, G. A.; O., F.; Foresman, J. B.; Fox, J. D. Gaussian 16. *Gaussian, Inc., Wallingford CT,*. 2016.

(61) Gospodinova, N.; Tomšík, E. Hydrogen-Bonding versus π-π Stacking in the Design of Organic Semiconductors: From Dyes to Oligomers. *Progress in Polymer Science*. 2015. https://doi.org/10.1016/j.progpolymsci.2014.10.010.

(62) Edwards, R. L.; Kale, N. The Structure of Xylindein. *Tetrahedron* **1965**. https://doi.org/10.1016/S0040-4020(01)98346-2.

(63) Saikawa, Y.; Watanabe, T.; Hashimoto, K.; Nakata, M. Absolute Configuration and Tautomeric Structure of Xylindein, a Blue-Green Pigment of Chlorociboria Species. *Phytochemistry* **2000**, *55* (3), 237–240. https://doi.org/10.1016/S0031-9422(00)00282-X.

(64) Arias, A. C.; MacKenzie, J. D.; McCulloch, I.; Rivnay, J.; Salleo, A. Materials

and Applications for Large Area Electronics: Solution-Based Approaches. *Chem. Rev.* **2010**. https://doi.org/10.1021/cr900150b.

(65) Irimia-Vladu, M.; Sariciftci, N. S.; Bauer, S. Exotic Materials for Bio-Organic Electronics. *J. Mater. Chem.* **2011**. https://doi.org/10.1039/c0jm02444a.

(66) Guo, X.; Facchetti, A.; Marks, T. J. Imide- and Amide-Functionalized Polymer Semiconductors. *Chemical Reviews*. 2014. https://doi.org/10.1021/cr500225d.

(67) Nielsen, C. B.; Turbiez, M.; McCulloch, I. Recent Advances in the Development of Semiconducting DPP-Containing Polymers for Transistor Applications. *Advanced Materials*. 2013. https://doi.org/10.1002/adma.201201795.

(68) Daniel Głowacki, E.; Leonat, L.; Irimia-Vladu, M.; Schwödiauer, R.; Ullah, M.; Sitter, H.; Bauer, S.; Serdar Sariciftci, N. Intermolecular Hydrogen-Bonded Organic Semiconductors-Quinacridone versus Pentacene. *Appl. Phys. Lett.* **2012**. https://doi.org/10.1063/1.4736579.

(69) Głowacki, E. D.; Romanazzi, G.; Yumusak, C.; Coskun, H.; Monkowius, U.; Voss, G.; Burian, M.; Lechner, R. T.; Demitri, N.; Redhammer, G. J.; Sünger, N.; Suranna, G. P.; Sariciftci, S. Epindolidiones-Versatile and Stable Hydrogen-Bonded Pigments for Organic Field-Effect Transistors and Light-Emitting Diodes. *Adv. Funct. Mater.* **2015**. https://doi.org/10.1002/adfm.201402539.

(70) Robinson, S. C. Developing Fungal Pigments for “Painting” Vascular Plants. *Applied Microbiology and Biotechnology*. 2012. https://doi.org/10.1007/s00253-011-3858-2.

(71) Blanchette, R. A.; Wilmering, A. M.; Baumeister, M. The Use of Green-Stained Wood Caused by the Fungus Chlorociboria in Intarsia1 Masterpieces from the 15th Century. *Holzforschung* **1992**. https://doi.org/10.1515/hfsg.1992.46.3.225.

(72) Robinson, S. C.; Michaelsen, H.; Robinson, J. C. *Spalted Wood: The History, Science, and Art of a Unique Material*; Schiffer Publishing: Atglen, Pennsylvania, 2016.

(73) Weber, G. A Method to Stimulate Production of Extracellular Pigments from

Wooddegrading Fungi Using a Water Carrier. *Curr. Res. Environ. Appl. Mycol.* **2016**. https://doi.org/10.5943/cream/6/3/10.

(74) Robinson, S. C.; Hinsch, E.; Weber, G.; Leipus, K.; Cerney, D. Wood Colorization through Pressure Treating: The Potential of Extracted Colorants from Spalting Fungi as a Replacement for Woodworkers' Aniline Dyes. *Materials (Basel).* **2014**. https://doi.org/10.3390/ma7085427.

(75) Robinson, S. C.; Laks, P. E. Wood Species Affects Laboratory Colonization Rates of Chlorociboria Sp. *Int. Biodeterior. Biodegrad.* **2010**. https://doi.org/10.1016/j.ibiod.2010.03.003.

(76) Song, C.; Swager, T. M. Conducting Polymers Containing Peri-Xanthenoxanthenes via Oxidative Cyclization of Binaphthols. *Macromolecules* **2009**. https://doi.org/10.1021/ma802755a.

(77) Wang, L.; Duan, G.; Ji, Y.; Zhang, H. Electronic and Charge Transport Properties of Peri-Xanthenoxanthene: The Effects of Heteroatoms and Phenyl Substitutions. *J. Phys. Chem. C* **2012**, *116* (43), 22679–22686. https://doi.org/10.1021/jp306326e.

(78) Mei, J.; Diao, Y.; Appleton, A. L.; Fang, L.; Bao, Z. Integrated Materials Design of Organic Semiconductors for Field-Effect Transistors. *Journal of the American Chemical Society*. 2013. https://doi.org/10.1021/ja400881n.

(79) Lv, N.; Xie, M.; Gu, W.; Ruan, H.; Qiu, S.; Zhou, C.; Cui, Z. Synthesis, Properties, and Structures of Functionalized Peri -Xanthenoxanthene. *Org. Lett.* **2013**, *15* (10), 2382–2385. https://doi.org/10.1021/ol400790d.

(80) Yoneya, N.; Ono, H.; Ishii, Y.; Himori, K.; Hirai, N.; Abe, H.; Yumoto, A.; Kobayashi, N.; Nomoto, K. Flexible Electrophoretic Display Driven by Solution-Processed Organic Thin-Film Transistors. *J. Soc. Inf. Disp.* **2012**. https://doi.org/10.1889/jsid20.3.143.

(81) Yokokura, S.; Takahashi, Y.; Hasegawa, H.; Harada, J.; Inabe, T.; Matsushita, M. M.; Awaga, K. Transport Characteristics of the Organic Field-Effect Transistors Based on Charge Transfer Complex as Semiconductors. *J. Nanosci. Nanotechnol.* **2016**. https://doi.org/10.1166/jnn.2016.12301.

(82) Christensen, J. A.; Zhang, J.; Zhou, J.; Nelson, J. N.; Wasielewski, M. R. Near-

Infrared Excitation of the Peri-Xanthenoxanthene Radical Cation Drives Energy-Demanding Hole Transfer Reactions. *J. Phys. Chem. C* **2018**, *122* (41), 23364–23370. https://doi.org/10.1021/acs.jpcc.8b07819.

(83) Donner, C. D.; Cuzzupe, A. N.; Falzon, C. L.; Gill, M. Investigations towards the Synthesis of Xylindein, a Blue-Green Pigment from the Fungus Chlorociboria Aeruginosa. *Tetrahedron* **2012**. https://doi.org/10.1016/j.tet.2012.02.009.

(84) Blackburn, G. M.; Neilson, A. H.; Todd, Lord. The Structure of Xylindein. *Proc. Chem. Soc.* **1962**. https://doi.org/10.1039/PS9620000317.

(85) Weber, G.; Chen, H. L.; Hinsch, E.; Freitas, S.; Robinson, S. Pigments Extracted from the Wood-Staining Fungi Chlorociboria Aeruginosa, Scytalidium Cuboideum, and S. Ganodermophthorum Show Potential for Use as Textile Dyes. *Color. Technol.* **2014**. https://doi.org/10.1111/cote.12110.

(86) Boonloed, A.; Weber, G. L.; Ramzy, K. M.; Dias, V. R.; Remcho, V. T. Centrifugal Partition Chromatography: A Preparative Tool for Isolation and Purification of Xylindein from Chlorociboria Aeruginosa. *J. Chromatogr. A* **2016**. https://doi.org/10.1016/j.chroma.2016.11.026.

(87) Shepherd, W. E. B.; Grollman, R.; Robertson, A.; Paudel, K.; Hallani, R.; Loth, M. A.; Anthony, J. E.; Ostroverkhova, O. Single-Molecule Imaging of Organic Semiconductors: Toward Nanoscale Insights into Photophysics and Molecular Packing. *Chem. Phys. Lett.* **2015**, *629*, 29–35. https://doi.org/10.1016/j.cplett.2015.04.014.

(88) Platt, A. D.; Day, J.; Subramanian, S.; Anthony, J. E.; Ostroverkhova, O. Optical, Fluorescent, and (Photo)Conductive Properties of High-Performance Functionalized Pentacene and Anthradithiophene Derivatives. *J. Phys. Chem. C* **2009**, *113* (31), 14006–14014. https://doi.org/10.1021/jp904021p.

(89) Paudel, K.; Johnson, B.; Thieme, M.; Haley, M. M.; Payne, M. M.; Anthony, J. E.; Ostroverkhova, O. Enhanced Charge Photogeneration Promoted by Crystallinity in Small-Molecule Donor-Acceptor Bulk Heterojunctions. *Appl. Phys. Lett.* **2014**. https://doi.org/10.1063/1.4891758.

(90) Day, J.; Platt, A. D.; Ostroverkhova, O.; Subramanian, S.; Anthony, J. E.

Organic Semiconductor Composites: Influence of Additives on the Transient Photocurrent. *Appl. Phys. Lett.* **2009**. https://doi.org/10.1063/1.3062850.

(91) Van Schenck, J. D. B.; Giesbers, G.; Kannegulla, A.; Cheng, L. J.; Anthony, J. E.; Ostroverkhova, O. Molecular Packing-Dependent Exciton and Polariton Dynamics in Anthradithiophene Organic Crystals. In *MRS Advances*; 2018. https://doi.org/10.1557/adv.2018.471.

(92) Yamagata, H.; Maxwell, D. S.; Fan, J.; Kittilstved, K. R.; Briseno, A. L.; Barnes, M. D.; Spano, F. C. HJ-Aggregate Behavior of Crystalline 7,8,15,16-Tetraazaterrylene: Introducing a New Design Paradigm for Organic Materials. *J. Phys. Chem. C* **2014**. https://doi.org/10.1021/jp509011u.

(93) Hestand, N. J.; Spano, F. C. Expanded Theory of H- and J-Molecular Aggregates: The Effects of Vibronic Coupling and Intermolecular Charge Transfer. *Chemical Reviews*. American Chemical Society August 8, 2018, pp 7069–7163. https://doi.org/10.1021/acs.chemrev.7b00581.

(94) Yamazaki, S.; Sobolewski, A. L.; Domcke, W. Molecular Mechanisms of the Photostability of Indigo. *Phys. Chem. Chem. Phys.* **2011**, *13* (4), 1618–1628. https://doi.org/10.1039/c0cp01901a.

(95) Robinson, S. C. The Fine Art of Decay. *Am. Sci.* **2014**, *102* (3), 206–213. https://doi.org/10.1511/2014.108.206.

(96) Miliani, C.; Monico, L.; Melo, M. J.; Fantacci, S.; Angelin, E. M.; Romani, A.; Janssens, K. Photochemistry of Artists' Dyes and Pigments: Towards Better Understanding and Prevention of Colour Change in Works of Art. *Angewandte Chemie - International Edition*. 2018. https://doi.org/10.1002/anie.201802801.

(97) Hinsch, E.; Robinson, S. Fungal Pigments as Textlile Dyes. In *Handbook of Textile Coloration and Finishing*; Studium Press LLC, 2018.

(98) Chen, T. L.; Chen, J. J. A.; Catane, L.; Ma, B. Fully Solution Processed P-i-n Organic Solar Cells with an Industrial Pigment - Quinacridone. *Org. Electron.* **2011**. https://doi.org/10.1016/j.orgel.2011.03.039.

(99) Giesbers, G.; Krueger, T.; Van Schenck, J.; Van Court, R.; Morré, J.; Fang, C.; Robinson, S.; Ostroverkhova, O. Fungi-Derived Xylindein: Effect of Purity on Optical and Electronic Properties. *MRS Adv.* **2019**, *4* (31–32), 1769–1777.

https://doi.org/10.1557/adv.2019.269.

(100) Smith, J.; Zhang, W.; Sougrat, R.; Zhao, K.; Li, R.; Cha, D.; Amassian, A.; Heeney, M.; McCulloch, I.; Anthopoulos, T. D. Solution-Processed Small Molecule-Polymer Blend Organic Thin-Film Transistors with Hole Mobility Greater than 5 Cm 2/Vs. *Adv. Mater.* **2012**. https://doi.org/10.1002/adma.201200088.

(101) Niazi, M. R.; Li, R.; Qiang Li, E.; Kirmani, A. R.; Abdelsamie, M.; Wang, Q.; Pan, W.; Payne, M. M.; Anthony, J. E.; Smilgies, D. M.; Thoroddsen, S. T.; Giannelis, E. P.; Amassian, A. Solution-Printed Organic Semiconductor Blends Exhibiting Transport Properties on Par with Single Crystals. *Nat. Commun.* **2015**. https://doi.org/10.1038/ncomms9598.

(102) Blakesley, J. C.; Castro, F. A.; Kylberg, W.; Dibb, G. F. A.; Arantes, C.; Valaski, R.; Cremona, M.; Kim, J. S.; Kim, J. S. Towards Reliable Charge-Mobility Benchmark Measurements for Organic Semiconductors. *Org. Electron.* **2014**. https://doi.org/10.1016/j.orgel.2014.02.008.

(103) Goetz, K. P.; Jurchescu, O. D. Conductivity Measurements of Organic Materials Using Field-Effect Transistors (FETs) and Space-Charge-Limited Current (SCLC) Techniques. In *Handbook of Organic Materials for Electronic and Photonic Devices*; 2019. https://doi.org/10.1016/b978-0-08-102284-9.00014-0.

(104) Hou, Z.; You, W.; Yu, L. Effect of a Trapping Molecule on the Monolithic Organic Photorefractive Materials. *Appl. Phys. Lett.* **2004**. https://doi.org/10.1063/1.1829796.

(105) Martin, S. J.; Lupton, J. M.; Samuel, I. D. W.; Walker, A. B. Modelling Temperature-Dependent Current-Voltage Characteristics of an MEH-PPV Organic Light Emitting Device. *J. Phys. Condens. Matter* **2002**. https://doi.org/10.1088/0953-8984/14/42/307.

(106) Blakesley, J. C.; Clubb, H. S.; Greenham, N. C. Temperature-Dependent Electron and Hole Transport in Disordered Semiconducting Polymers: Analysis of Energetic Disorder. *Phys. Rev. B - Condens. Matter Mater. Phys.* **2010**. https://doi.org/10.1103/PhysRevB.81.045210.

(107) Blom, P. W. M.; Vissenberg, M. C. J. M. Charge Transport in Poly(p-Phenylene Vinylene) Light-Emitting Diodes. *Mater. Sci. Eng. R Reports* **2000**. https://doi.org/10.1016/S0927-796X(00)00009-7.

(108) Choudhury, K. R.; Samoc, M.; Patra, A.; Prasad, P. N. Charge Carrier Transport in Poly(N-Vinylcarbazole):CdS Quantum Dot Hybrid Nanocomposites. *J. Phys. Chem. B* **2004**. https://doi.org/10.1021/jp0360671.

(109) Mei, Y.; Diemer, P. J.; Niazi, M. R.; Hallani, R. K.; Jarolimek, K.; Day, C. S.; Risko, C.; Anthony, J. E.; Amassian, A.; Jurchescu, O. D. Crossover from Band-like to Thermally Activated Charge Transport in Organic Transistors Due to Strain-Induced Traps. *Proc. Natl. Acad. Sci. U. S. A.* **2017**. https://doi.org/10.1073/pnas.1705164114.

(110) Kishore, V. C.; Dhanya, R.; Kartha, C. S.; Sreekumar, K.; Joseph, R. Photoconductivity in Molecularly Doped Poly(Methylmethacrylate) Sandwich Cells. *J. Appl. Phys.* **2007**. https://doi.org/10.1063/1.2710773.

(111) Ostroverkhova, O.; He, M.; Twieg, R. J.; Moerner, W. E. Role of Temperature in Controlling Performance of Photorefractive Organic Glasses. *ChemPhysChem* **2003**, *4* (7), 732–744. https://doi.org/10.1002/cphc.200200633.

(112) Day, J.; Subramanian, S.; Anthony, J. E.; Lu, Z.; Twieg, R. J.; Ostroverkhova, O. Photoconductivity in Organic Thin Films: From Picoseconds to Seconds after Excitation. *J. Appl. Phys.* **2008**. https://doi.org/10.1063/1.2946453.

(113) Purushothaman, B.; Parkin, S. R.; Kendrick, M. J.; David, D.; Ward, J. W.; Yu, L.; Stingelin, N.; Jurchescu, O. D.; Anthony, J. E. Synthesis and Charge Transport Studies of Stable, Soluble Hexacenes. *Chem. Commun.* **2012**, *48* (66), 8261–8263. https://doi.org/10.1039/c2cc33919f.

(114) Grollman, R.; Quist, N.; Robertson, A.; Rath, J.; Purushothaman, B.; Haley, M. M.; Anthony, J. E.; Ostroverkhova, O. Single-Molecule Level Insight into Nanoscale Environment-Dependent Photophysics in Blends. *J. Phys. Chem. C* **2017**, *121* (22), 12483–12494. https://doi.org/10.1021/acs.jpcc.7b03729.

(115) Zhang, L.; Fonari, A.; Liu, Y.; Hoyt, A. L. M.; Lee, H.; Granger, D.; Parkin, S.; Russell, T. P.; Anthony, J. E.; Brédas, J. L.; Coropceanu, V.; Briseno, A. L.

Bistetracene: An Air-Stable, High-Mobility Organic Semiconductor with Extended Conjugation. *J. Am. Chem. Soc.* **2014**, *136* (26), 9248–9251. https://doi.org/10.1021/ja503643s.

(116) Głowacki, E. D.; Irimia-Vladu, M.; Kaltenbrunner, M.; Gsiorowski, J.; White, M. S.; Monkowius, U.; Romanazzi, G.; Suranna, G. P.; Mastrorilli, P.; Sekitani, T.; Bauer, S.; Someya, T.; Torsi, L.; Sariciftci, N. S. Hydrogen-Bonded Semiconducting Pigments for Air-Stable Field-Effect Transistors. *Adv. Mater.* **2013**, *25* (11), 1563–1569. https://doi.org/10.1002/adma.201204039.

(117) Zhang, F.; Lemaur, V.; Choi, W.; Kafle, P.; Seki, S.; Cornil, J.; Beljonne, D.; Diao, Y. Repurposing DNA-Binding Agents as H-Bonded Organic Semiconductors. *Nat. Commun.* **2019**, *10* (1), 1–11. https://doi.org/10.1038/s41467-019-12248-9.

(118) Al-Aqar, R.; Benniston, A. C.; Harriman, A.; Perks, T. Structural Dynamics and Barrier Crossing Observed for a Fluorescent O-Doped Polycyclic Aromatic Hydrocarbon. *ChemPhotoChem* **2017**, *1* (5), 198–205. https://doi.org/10.1002/cptc.201600016.

(119) Sciutto, A.; Berezin, A.; Lo Cicero, M.; Miletić, T.; Stopin, A.; Bonifazi, D. Tailored Synthesis of N -Substituted Peri-Xanthenoxanthene Diimide (PXXDI) and Monoimide (PXXMI) Scaffolds. *J. Org. Chem.* **2018**, *83* (22), 13787–13798. https://doi.org/10.1021/acs.joc.8b02076.

(120) Zhou, Y.; Fuentes-Hernandez, C.; Shim, J.; Meyer, J.; Giordano, A. J.; Li, H.; Winget, P.; Papadopoulos, T.; Cheun, H.; Kim, J.; Fenoll, M.; Dindar, A.; Haske, W.; Najafabadi, E.; Khan, T. M.; Sojoudi, H.; Barlow, S.; Graham, S.; Brédas, J. L.; Marder, S. R.; Kahn, A.; Kippelen, B. A Universal Method to Produce Low-Work Function Electrodes for Organic Electronics. *Science (80-.).* **2012**, *336* (6079), 327–332. https://doi.org/10.1126/science.1218829.

(121) Tang, L.; Zhu, L.; Taylor, M. A.; Wang, Y.; James Remington, S.; Fang, C. Excited State Structural Evolution of a GFP Single-Site Mutant Tracked by Tunable Femtosecond-Stimulated Raman Spectroscopy. *Molecules* **2018**, *23* (9). https://doi.org/10.3390/molecules23092226.

(122) Taylor, M. A.; Zhu, L.; Rozanov, N. D.; Stout, K. T.; Chen, C.; Fang, C.

Delayed Vibrational Modulation of the Solvated GFP Chromophore into a Conical Intersection. *Phys. Chem. Chem. Phys.* **2019**, *21* (19), 9728–9739. https://doi.org/10.1039/c9cp01077g.

(123) Liebel, M.; Schnedermann, C.; Wende, T.; Kukura, P. Principles and Applications of Broadband Impulsive Vibrational Spectroscopy. *J. Phys. Chem. A* **2015**, *119* (36), 9506–9517. https://doi.org/10.1021/acs.jpca.5b05948.

(124) Liu, W.; Wang, Y.; Tang, L.; Oscar, B. G.; Zhu, L.; Fang, C. Panoramic Portrait of Primary Molecular Events Preceding Excited State Proton Transfer in Water. *Chem. Sci.* **2016**, *7* (8), 5484–5494. https://doi.org/10.1039/c6sc00672h.

(125) Ostroverkhova, O.; Shcherbyna, S.; Cooke, D. G.; Egerton, R. F.; Hegmann, F. A.; Tykwinski, R. R.; Parkin, S. R.; Anthony, J. E. Optical and Transient Photoconductive Properties of Pentacene and Functionalized Pentacene Thin Films: Dependence on Film Morphology. *J. Appl. Phys.* **2005**, *98* (3). https://doi.org/10.1063/1.1949711.

(126) Spano, F. C. The Spectral Signatures of Frenkel Polarons in H-and J-Aggregates. *Acc. Chem. Res.* **2009**, *43* (3), 429–439. https://doi.org/10.1021/ar900233v.

(127) Fang, C.; Tang, L.; Oscar, B. G.; Chen, C. Capturing Structural Snapshots during Photochemical Reactions with Ultrafast Raman Spectroscopy: From Materials Transformation to Biosensor Responses. *Journal of Physical Chemistry Letters*. American Chemical Society June 21, 2018, pp 3253–3263. https://doi.org/10.1021/acs.jpclett.8b00373.

(128) Tang, L.; Wang, Y.; Zhu, L.; Lee, C.; Fang, C. Correlated Molecular Structural Motions for Photoprotection after Deep-UV Irradiation. *J. Phys. Chem. Lett.* **2018**, *9* (9), 2311–2319. https://doi.org/10.1021/acs.jpclett.8b00999.

(129) Fudickar, W.; Linker, T. Why Triple Bonds Protect Acenes from Oxidation and Decomposition. *J. Am. Chem. Soc.* **2012**, *134* (36), 15071–15082. https://doi.org/10.1021/ja306056x.

(130) Panzer, F.; Sommer, M.; Bässler, H.; Thelakkat, M.; Köhler, A. Spectroscopic Signature of Two Distinct H-Aggregate Species in Poly(3-Hexylthiophene).

Macromolecules **2015**, *48* (5), 1543–1553. https://doi.org/10.1021/acs.macromol.5b00129.

(131) Ravi Kishore, V. V. N.; Narasimhan, K. L.; Periasamy, N. On the Radiative Lifetime, Quantum Yield and Fluorescence Decay of Alq in Thin Films. *Phys. Chem. Chem. Phys.* **2003**, *5* (7), 1386–1391. https://doi.org/10.1039/b211264g.

(132) Bruevich, V.; Choi, H. H.; Podzorov, V. The Photo-Hall Effect in High-Mobility Organic Semiconductors. *Adv. Funct. Mater.* **2020**. https://doi.org/10.1002/adfm.202006178.

(133) Paudel, K.; Johnson, B.; Neunzert, A.; Thieme, M.; Purushothaman, B.; Payne, M. M.; Anthony, J. E.; Ostroverkhova, O. Small-Molecule Bulk Heterojunctions: Distinguishing between Effects of Energy Offsets and Molecular Packing on Optoelectronic Properties. *J. Phys. Chem. C* **2013**, *117* (47), 24752–24760. https://doi.org/10.1021/jp4093089.

(134) Zhang, M.; Zhu, L.; Zhou, G.; Hao, T.; Qiu, C.; Zhao, Z.; Hu, Q.; Larson, B. W.; Zhu, H.; Ma, Z.; Tang, Z.; Feng, W.; Zhang, Y.; Russell, T. P.; Liu, F. Single-Layered Organic Photovoltaics with Double Cascading Charge Transport Pathways: 18% Efficiencies. *Nat. Commun.* **2021**, *12* (1), 1–10. https://doi.org/10.1038/s41467-020-20580-8.

(135) Andreani, L. C.; Bozzola, A.; Kowalczewski, P.; Liscidini, M.; Redorici, L. Silicon Solar Cells: Toward the Efficiency Limits. *Advances in Physics: X*. Taylor and Francis Ltd. January 1, 2019, p 1548305. https://doi.org/10.1080/23746149.2018.1548305.

(136) Lee, H. K. H.; Wu, J.; Barbé, J.; Jain, S. M.; Wood, S.; Speller, E. M.; Li, Z.; Castro, F. A.; Durrant, J. R.; Tsoi, W. C. Organic Photovoltaic Cells-Promising Indoor Light Harvesters for Self-Sustainable Electronics. *J. Mater. Chem. A* **2018**, *6* (14), 5618–5626. https://doi.org/10.1039/c7ta10875c.

(137) Yumusak, C.; Sariciftci, N. S.; Irimia-Vladu, M. Purity of Organic Semiconductors as a Key Factor for the Performance of Organic Electronic Devices. *Mater. Chem. Front.* **2020**, *4* (12), 3678–3689. https://doi.org/10.1039/d0qm00690d.

(138) Irimia-Vladu, M.; Kanbur, Y.; Camaioni, F.; Coppola, M. E.; Yumusak, C.;

Irimia, C. V.; Vlad, A.; Operamolla, A.; Farinola, G. M.; Suranna, G. P.; González-Benitez, N.; Molina, M. C.; Bautista, L. F.; Langhals, H.; Stadlober, B.; Głowacki, E. D.; Sariciftci, N. S. Stability of Selected Hydrogen Bonded Semiconductors in Organic Electronic Devices. *Chemistry of Materials*. American Chemical Society September 10, 2019, pp 6315–6346. https://doi.org/10.1021/acs.chemmater.9b01405.

(139) Vahidzadeh, E.; Kalra, A. P.; Shankar, K. Melanin-Based Electronics: From Proton Conductors to Photovoltaics and Beyond. *Biosens. Bioelectron.* **2018**, *122*, 127–139. https://doi.org/10.1016/j.bios.2018.09.026.

(140) Rivnay, J.; Inal, S.; Salleo, A.; Owens, R. M.; Berggren, M.; Malliaras, G. G. *Organic Electrochemical Transistors Kingdom of Saudi Arabia*; Vol. 2.

(141) Nguy, T. P.; Hayakawa, R.; Kilinc, V.; Petit, M.; Raimundo, J. M.; Charrier, A.; Wakayama, Y. Stable Operation of Water-Gated Organic Field-Effect Transistor Depending on Channel Flatness, Electrode Metals and Surface Treatment. *Jpn. J. Appl. Phys.* **2019**, *58* (SD), SDDH02. https://doi.org/10.7567/1347-4065/ab09d2.

(142) Yaman, B.; Terkesli, I.; Turksoy, K. M.; Sanyal, A.; Mutlu, S. Fabrication of a Planar Water Gated Organic Field Effect Transistor Using a Hydrophilic Polythiophene for Improved Digital Inverter Performance. *Org. Electron.* **2014**, *15* (3), 646–653. https://doi.org/10.1016/j.orgel.2013.12.024.

(143) Porrazzo, R.; Luzio, A.; Bellani, S.; Bonacchini, G. E.; Noh, Y. Y.; Kim, Y. H.; Lanzani, G.; Antognazza, M. R.; Caironi, M. Water-Gated n-Type Organic Field-Effect Transistors for Complementary Integrated Circuits Operating in an Aqueous Environment. *ACS Omega* **2017**, *2* (1), 1–10. https://doi.org/10.1021/acsomega.6b00256.

(144) Cramer, T.; Campana, A.; Leonardi, F.; Casalini, S.; Kyndiah, A.; Murgia, M.; Biscarini, F. Water-Gated Organic Field Effect Transistors-Opportunities for Biochemical Sensing and Extracellular Signal Transduction. *Journal of Materials Chemistry B*. Royal Society of Chemistry August 21, 2013, pp 3728–3741. https://doi.org/10.1039/c3tb20340a.

(145) Kim, Y. J.; Khetan, A.; Wu, W.; Chun, S. E.; Viswanathan, V.; Whitacre, J. F.;

Bettinger, C. J. Evidence of Porphyrin-Like Structures in Natural Melanin Pigments Using Electrochemical Fingerprinting. *Adv. Mater.* **2016**, *28* (16), 3173–3180. https://doi.org/10.1002/adma.201504650.

(146) Tong, L.; Jing, Y.; Gordon, R. G.; Aziz, M. J. Symmetric All-Quinone Aqueous Battery. *ACS Appl. Energy Mater.* **2019**, *2* (6), 4016–4021. https://doi.org/10.1021/acsaem.9b00691.

(147) Luo, W.; Allen, M.; Raju, V.; Ji, X. An Organic Pigment as a High-Performance Cathode for Sodium-Ion Batteries. *Adv. Energy Mater.* **2014**, *4* (15), 1400554. https://doi.org/10.1002/aenm.201400554.

(148) Sridharan, M.; Kamaraj, P.; Vennila, R.; Huh, Y. S.; Arthanareeswari, M. Bio-Inspired Construction of Melanin-like Polydopamine-Coated CeO2as a High-Performance Visible-Light-Driven Photocatalyst for Hydrogen Production. *New J. Chem.* **2020**, *44* (35), 15223–15234. https://doi.org/10.1039/d0nj02234a.

(149) Früchtl, H.; van Mourik, T. A Quinone Based Single-Molecule Switch as Building Block for Molecular Electronics. *Phys. Chem. Chem. Phys.* **2021**, *23* (3), 1811–1814. https://doi.org/10.1039/d0cp06250b.

(150) Malliaras, G. G. Organic Bioelectronics: A New Era for Organic Electronics. *Biochimica et Biophysica Acta - General Subjects*. Elsevier September 1, 2013, pp 4286–4287. https://doi.org/10.1016/j.bbagen.2012.10.007.

(151) Plumhof, J. D.; Stöferle, T.; Mai, L.; Scherf, U.; Mahrt, R. F. Room-Temperature Bose-Einstein Condensation of Cavity Exciton-Polaritons in a Polymer. *Nat. Mater.* **2014**, *13* (3), 247–252. https://doi.org/10.1038/nmat3825.

(152) Herrera, F.; Spano, F. C. Cavity-Controlled Chemistry in Molecular Ensembles. *Phys. Rev. Lett.* **2016**, *116* (23). https://doi.org/10.1103/PhysRevLett.116.238301.

(153) Orgiu, E.; George, J.; Hutchison, J. A.; Devaux, E.; Dayen, J. F.; Doudin, B.; Stellacci, F.; Genet, C.; Schachenmayer, J.; Genes, C.; Pupillo, G.; Samorì, P.; Ebbesen, T. W. Conductivity in Organic Semiconductors Hybridized with the Vacuum Field. *Nat. Mater.* **2015**, *14* (11), 1123–1129.

https://doi.org/10.1038/nmat4392.

(154) Held, M.; Graf, A.; Zakharko, Y.; Chao, P.; Tropf, L.; Gather, M. C.; Zaumseil, J. Ultrastrong Coupling of Electrically Pumped Near-Infrared Exciton-Polaritons in High Mobility Polymers. *Adv. Opt. Mater.* **2018**, *6* (3). https://doi.org/10.1002/adom.201700962.

(155) Kang, E. S. H.; Chen, S.; Đerek, V.; Hägglund, C.; Głowacki, E. D.; Jonsson, M. P.; Kang, E. S. H. Charge Transport in Phthalocyanine Thin-Film Transistors Coupled with Fabry-Perot Cavities. *J. Mater. Chem. C* **2021**, *9* (7), 2368–2374. https://doi.org/10.1039/d0tc05418f.

(156) Lamport, Z. A.; Barth, K. J.; Lee, H.; Gann, E.; Engmann, S.; Chen, H.; Guthold, M.; McCulloch, I.; Anthony, J. E.; Richter, L. J.; DeLongchamp, D. M.; Jurchescu, O. D. A Simple and Robust Approach to Reducing Contact Resistance in Organic Transistors. *Nat. Commun.* **2018**, *9* (1), 1–8. https://doi.org/10.1038/s41467-018-07388-3.

(157) Van Schenck, J. D. B.; Tanyi, E. K.; Cheng, L. J.; Anthony, J.; Ostroverkhova, O. Strong Exciton-Photon Coupling in Anthradithiophene Microcavities: From Isolated Molecules to Aggregates. *MRS Commun.* **2019**, *9* (3), 956–963. https://doi.org/10.1557/mrc.2019.101.

(158) Sheliakina, M.; Mostert, A. B.; Meredith, P. Decoupling Ionic and Electronic Currents in Melanin. *Adv. Funct. Mater.* **2018**, *28* (46), 1805514. https://doi.org/10.1002/adfm.201805514.

(159) Krueger, T. D.; Giesbers, G.; Van Court, R.; Zhu, L.; Kim, R.; Beaudry, C. M.; Robinson, S. C.; Ostroverkhova, O.; Fang, C. Ultrafast Dynamics and Photoresponse of a Fungi-Derived Pigment Xylindein from Solution to Thin Films. *Chem. - A Eur. J.* **2021**.

(160) Han, C.; Li, H.; Shi, R.; Zhang, T.; Tong, J.; Li, J.; Li, B. Organic Quinones towards Advanced Electrochemical Energy Storage: Recent Advances and Challenges. *Journal of Materials Chemistry A*. Royal Society of Chemistry October 22, 2019, pp 23378–23415. https://doi.org/10.1039/c9ta05252f.

(161) Tong, L.; Jing, Y.; Gordon, R. G.; Aziz, M. J. Symmetric All-Quinone Aqueous Battery. *ACS Appl. Energy Mater.* **2019**, *2* (6), 4016–4021.

https://doi.org/10.1021/acsaem.9b00691.

Appendix:

Further Notes on Xylindein Electrochemical Studies

Xylindein Protonic Conductivity

Melanin is known to exhibit protonic conductivity when hydrated.[139,158] It was hypothesized that xylindein, as another naturally derived hydroxyl containing pigment, could exhibit the same effect. One sign of this is an increase in conductivity with the presence of moisture,[139,158] which indeed was observed for xylindein. To further test the nature of conductivity in xylindein films, frequency dependent electrical measurements were taken using a lock-in amplifier. Figure A1 (a) shows frequency dependent conductivity data for ADT and xylindein. Both materials show little frequency dependence, as one may expect for electronic conduction. Figure A1 (b) shows frequency dependent conductivity data for a xylindein film before and after exposure to steam, effectively hydrating the film. The hydrated film shows a drastic change in the response, with the flat region of the pristine film disappearing and a large increase (up to the set compliance) in the response at very low frequencies. This indicates a change in the mechanism of conduction. Ionic conduction is much slower than electronic conduction, thus would appear as a response at much lower frequencies. This points to ionic (potentially protonic) conduction as the main conductive mechanism in the hydrated xylindein film.

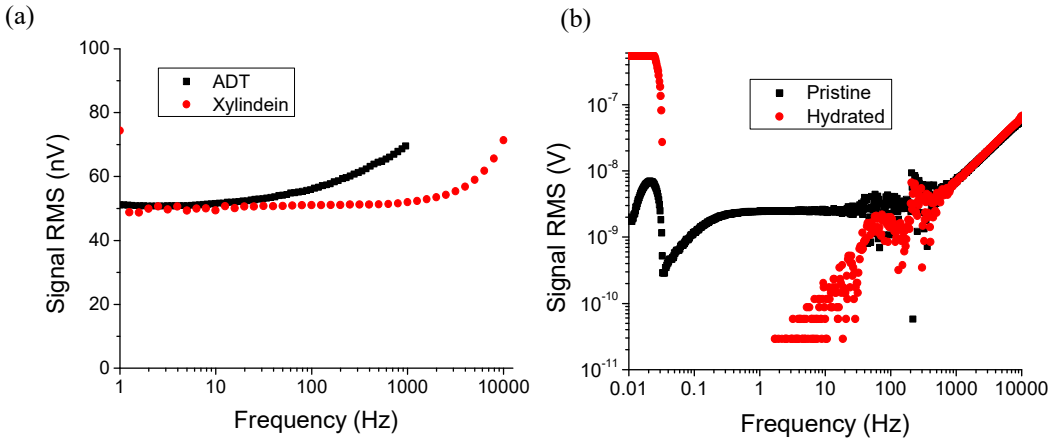

Figure A1. Frequency dependent conductivity data for thin films on interdigitated Au electrodes. (a) diF-TES-ADT versus xylindein. (b) Xylindein thin film before and after hydrating via exposure to steam. Data was taken using a lock-in amplifier to provide a 1V AC source, and measurement.

Xylindein Electrochemical Transistors

After successful organic electrochemical transistors (OECTs) were fabricated using PEDOT:PSS as an active material, the same configuration was used to attempt to fabricate OECTs using xylindein. Devices using this same configuration with NaCl in water as an electrolyte solution resulted in cyclic voltammetry (CV) like curves as seen in the main text. Additionally, some discoloration of the xylindein film was occasionally observed on the electrode. This discoloration tended to be localized to the xylindein that was in contact with one of the electrodes, and more likely to occur at higher voltages. In order to further investigated this behavior, several other electrolyte solutions were tested. Acids were tested to supply a source of protons, which was thought to be potentially beneficial for two reasons. First, since xylindein is believed to exhibit protonic conduction, the extra protons may facilitate conductivity and switching behavior. Second, since xylindein had been previously observed to be much less stable upon deprotonation,[159] this may provide a more stable medium. Figure A2 shows output curves for xylindein devices using HCl, Citric acid, and DI water. No discoloration was observed in any of these three solutions. The HCl solution device exhibited curves with a singular reduction and oxidation peaks in the classic “duck shape” of CV curves. Citric acid also showed CV like curves, while DI-water resulted in a working transistor device.

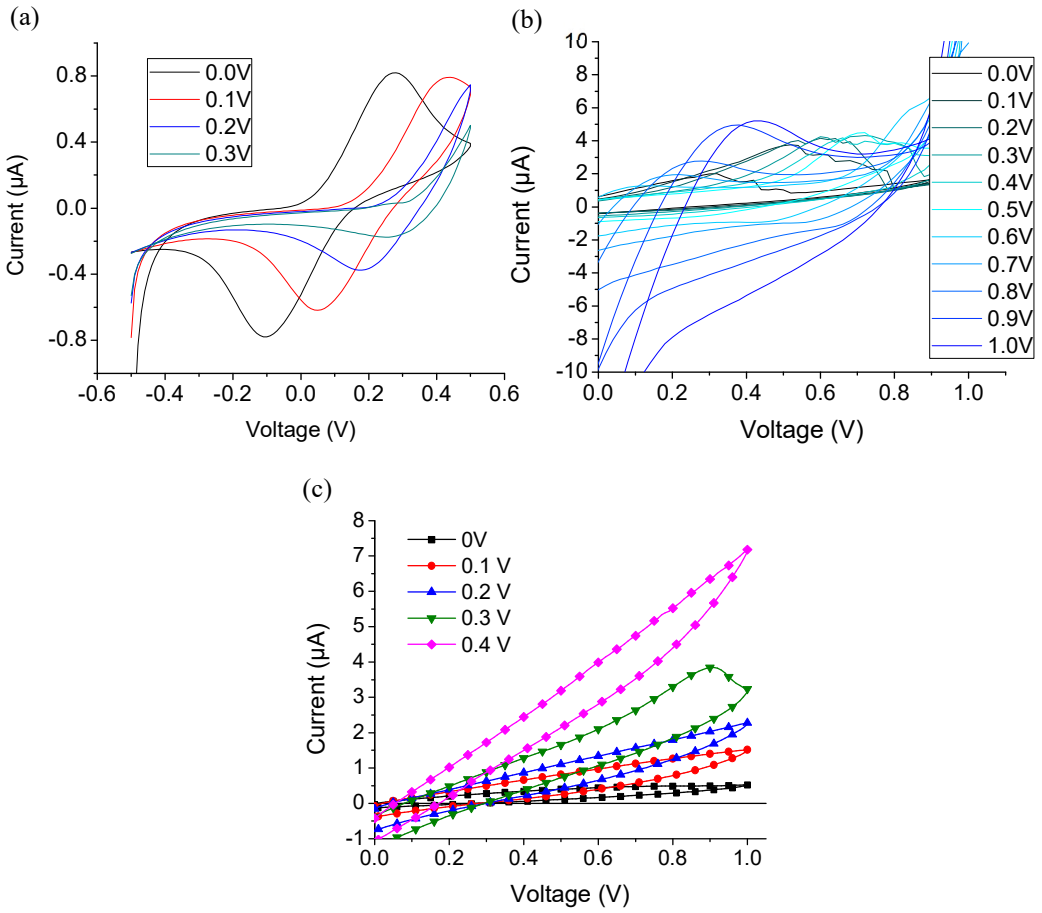

Figure A2. Cyclic current-voltage sweeps for xylindein devices in an electrochemical transistor configuration using 1mM HCl (a), 0.1M citric acid (b), and DI water (c) as the gating medium.

Pristine xylindein water gated transistors often displayed large hysteresis. Some xylindein composites were also tested, and seen to mitigate this effect. Figure A3 shows water gated transistors using xylindein blended with PEIE (a) and xylindein on top of a thin layer of PEDOT:PSS (b) in an electrochemical transistor configuration. Both of these devices show much less hysteresis than the pristine xylindein device, with a similar n-type accumulation mode transistor behavior.

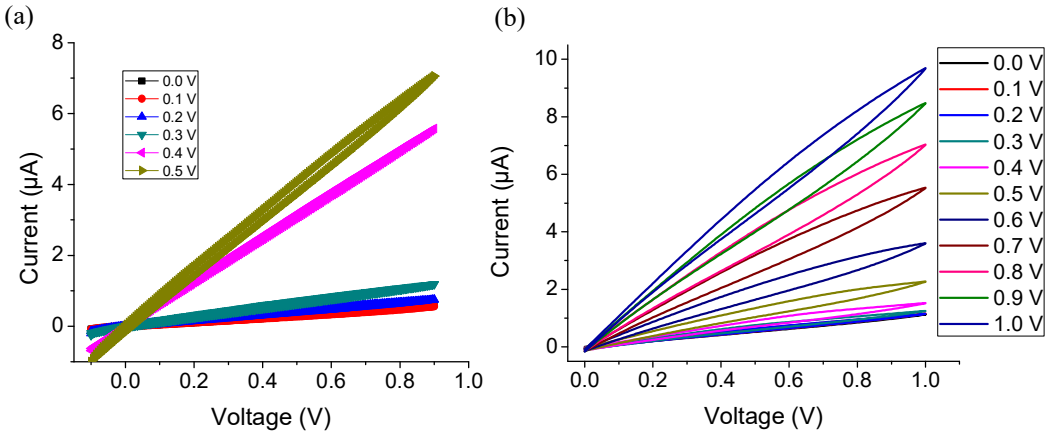

Figure A3. Water gated transistors using xylindein:PEIE (a) and xylindein on a thin layer of PEDOT:PSS (b) as the active layer

Xylindein Energy Storage Investigation

Quinone molecules and their derivatives, including naturally derived pigments, have been studied extensively for use in battery applications.[147,160,161] Xylindein, as a large quinone derivative has been seen to exhibit redox behavior in electrochemical transistor configurations, could be of potential use in this application. As an initial investigation, xylindein was compared to alizarin, a naturally derived hydroxy containing quinone derivative already researched in battery applications. In this initial investigation, pseudocapacitor structures were fabricated consisting of two carbon pencil lead electrodes immersed in a 0.1M H_2SO_4 solution. The electrodes were coated via dropcasting with either xylindein or alizarin. Figure A4 shows cyclic current voltage sweeps for the pseudocapacitors taken with a Keithley 237 source measurement unit. The symmetric alizarin pseudocapacitor appears to show two sets of small reduction and oxidation peaks, not too dissimilar from what has been reported in the literature.[146] Both the xylindein-alizarin and symmetric alizarin xylindein show several peaks that are promising. When the voltage window was increased on the symmetric xylindein device (Fig A4 (b)), sets of redox peaks were seen approximately 2V apart, which is an improvement upon reported alizarin devices,[146] if that voltage window is stable. Further investigation is required using a

proper cyclic voltammetry setup to accurately assess xylindein in energy storage applications.

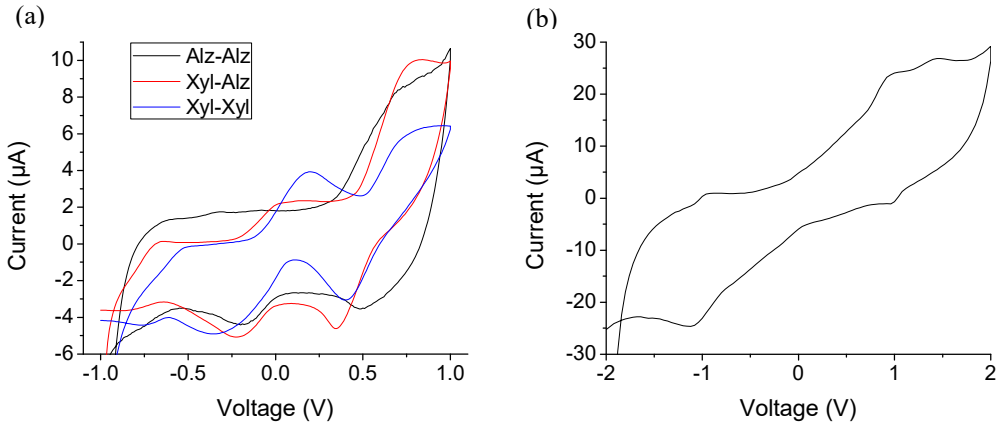

Figure A4. Cyclic current voltage sweeps for pseudocapacitor devices. (a) Sweeps for devices with two alizarin coated electrodes, one alizarin and one xylindein, and two xylindein coated electrodes. (b) Sweep for the all xylindein device with an expanded voltage window.